UNIVERSITY OF OKLAHOMA

GRADUATE COLLEGE

INVESTIGATION OF 3D PRINTED POROUS POLYDIMETHYLSILOXANE (PDMS)/CARBON NANOTUBE (CNT) NANOCOMPOSITES FOR SENSING APPLICATION

A THESIS

SUBMITTED TO THE GRADUATE FACULTY

In partial fulfillment of the requirements for the

Degree of

MASTER OF SCIENCE

By

MUSA NTOKOZO SUKATI

Norman, Oklahoma

2020

INVESTIGATION OF 3D PRINTED POROUS POLYDIMETHYLSILOXANE (PDMS)/CARBON NANOTUBE (CNT) NANOCOMPOSITES FOR SENSING APPLICATION

A THESIS APPROVED FOR THE

SCHOOL OF AEROSPACE AND MECHANICAL ENGINEERING

BY THE COMMITTEE CONSISTING OF

Dr. Mrinal Saha, Chair

Dr. Yingtao Liu, Co-Chair

Dr. M. Cengiz Altan

Acknowledgement

My deepest gratitude goes first to Dr. Mrinal C. Saha for allowing me to work within his research group and for investing large amounts of time and resources aiding and guiding me through my graduate research. My development as a researcher and all research work I have accomplished was made possible by his selfless and expert guidance. I would also like to thank Dr. Yingtao Liu for his expert knowledge and his valuable feedback. His patience and willingness helped to shape me into a more competent researcher. In addition, I would like to extend my gratitude to my committee member, Dr. M. Cengiz Altan, whose encouragement inspired me to fight through adversity in order to complete my thesis research. My research work would not have been possible without the help, guidance and cooperation from my lab mates. I would like to thank Anirban Mondal, Mohammad Abshirini, Mohammad Charara and Parisa Marashizadeh who taught me important aspects of the research work and worked with me to advance the research work. I would also like to thank Wenyuan Luo who encouraged me when I first started research and helped me to secure my place in the lab.

I am deeply grateful for my parents, Themba and Joyce Sukati, who made studying in the USA possible. Their enormous sacrifices to ensure that I leave my impoverished home country to pursue a rare opportunity played a great role in my development and the advancement of my professional and personal life. I want to also thank my siblings, Thandeka Magongo, Mlungisi Sukati and Smangele Matse for their love and encouragement. I also want to extend a special thanks to my girlfriend, Seapehi Molise, for her incredible support during a difficult and often stressful two years. I am forever grateful for her caring nature and for pushing me to achieve greater things in my engineering career.

Dedication

I would like to dedicate this thesis to my parents, Themba and Joyce Sukati, who made countless sacrifices in order to ensure that I received a very good education. I would also like to dedicate this thesis to my girlfriend, Seapehi Molise, who supported and motivated me through difficult times.

Table of Contents

Table of Figures

Table of Tables

Abstract

Sensors manufactured using piezoresistive elastomeric nanocomposites have a wide range of applications in fields such as structural health monitoring, robotics and biomedical industries. These nanocomposites are a mixture of highly deformable polymers and conducting nanofillers that have the special property of experiencing a change in their electrical conductivity when compressed or stretched. The use of Additive Manufacturing processes such as Stereolithography Apparatus (SLA) and Direct Ink Writing (DIW) to construct sensors from these nanocomposites has provided numerous advantages including increased sensitivity of the sensors and the fabrication of complex geometry. However, bulk material sensors, manufactured additively or using conventional methods, display a greater effect of hysteresis, especially at strains higher than 10%, which limits their sensitivity. In order to address this challenge, this thesis focuses on the use of porosity in the form of varying infill densities and patterns made possible by Additive Manufacturing processes to significantly reduce these bulk material effects.

The additive manufacturing of porous structures requires the nanocomposite material to hold its shape well after extrusion, and it should keep its shape when subsequent layers of material are deposited above it. Pristine polymers such as polydimethylsiloxane (PDMS) have no yield point which is a signifier of material that can hold its shape, therefore they cannot be successfully 3D printed while freestanding since they collapse and spread after extrusion. A thixotropic silica filler and carbon nanotubes (CNTs) were used to allow the material to hold shape and have a significantly higher yield stress required for porous structures to successfully print. Peak hold and amplitude sweep tests were conducted on nanomaterial consisting of 1.5% CNT and silica content ranging from 5-20% in order to quantify the rheological properties of the material. While all the silica content percentages had yield points and could hold shape during 3D printing, the material

formulation containing 15% silica was selected as the ideal material due to its high yield point and low brittleness.

Cuboids were 3D printed from this material using three infill patterns, three infill densities and two syringe needle sizes. The fabricated samples are characterized using a scanning electron microscope (SEM) to validate the microstructural features, layer bonding and infill densities. Each sensor's pressure sensing capability is investigated using cyclic compression loading at various maximum strains. Sensing experiments show an increase in both stress and strain sensitivity, as well as a decrease in the mechanical and electrical hysteresis with the introduction of porosity. These results indicate that introducing porosity using 3D printing is a sensible strategy to improve the piezoresistive performance of nanocomposites and to allow for the tunability of sensing capacity in pressure sensors.

The mechanical performance of the sensors was analyzed along with tensile samples of the same infill patterns and densities. The fracture stress was determined and the locations of failure were analyzed. Finite Element Analysis was used to analyze the stress distribution within the material as well as to predict the location of failure. Mechanical results show a significant increase in the fracture stress of the porous compression samples above 40% infill density, therefore highlighting their durability and robustness. Results also show a reduction in the fracture stress for tension samples, highlighting their weakness under tensile loads.

Chapter 1. Introduction

Sensors manufactured from highly elastic piezoresistive materials have attracted great interest in a variety of research fields. These sensors have a wide range of applications in the fields of robotics [1], structural health monitoring [2], wearable electronics [3], and flexible pressure sensors [4]. Highly flexible piezoresistive sensors have been shown to have greater sensing capacity compared to conventional strain gauges which have a typical gauge factor of 2 and a maximum strain of approximately 10% [5]. These sensors consist of the blend of a polymer and conductive nanomaterial, and they are endowed with hyperelastic properties and low stiffness [6]. They are fabricated using a wide variety of polymers such as thermosets, thermoplastics and elastomers, as well as a wide range of nanofillers including carbon nanofibers, carbon nanotubes, carbon black, graphene, and silver nanowires [7]. Besides providing electrical conductivity, the nanofillers also act as the reinforcement within the material, with the polymer acting as the matrix of the nanocomposite. These nanofillers, which are essentially multiphase solid materials whereby one of the phases has one, two or three dimensions of less than 100 nanometers, demonstrate good physical, chemical and biological properties that differ significantly from the properties of bulk materials. The nanofillers can be one dimensional such as carbon nanotubes, two-dimensional such as graphene, and three-dimensional such as carbon black. They have been shown to possess exceptionally high surface to volume ratios as well as high aspect ratios. Consequently, they supply the polymer matrix with multifunctional properties such as a high elastic modulus, increased fracture strength, as well as electrical and thermal conductivity [8].

Among the polymers that make up the base of these nanocomposites, elastomers have been widely researched due to their desired hyperelastic properties. In particular, the silicon-based organic polymer polydimethylsiloxane (PDMS) has drawn great attention from researchers due to

its inert, non-toxic, hydrophobic and non-flammable properties, as well as its hyperelasticity, biocompatibility, environmental friendliness and viscoelasticity [9]. PDMS also has mechanical properties that are easily tunable, making it vastly beneficial in the design of piezoresistive sensors. Various formulations of PDMS with varying viscosities and post-cure stiffnesses currently exist in the market. Industry trusted manufacturers of PDMS include Dow Corning and Gelest. The mechanical and rheological properties of PDMS can be altered by changing select factors such as the curing time, curing temperature, catalyst content and filler content. Most PDMS variants in the industry utilize a platinum-based catalyst which allows for shorter curing times and processing at high temperatures. Studies revealed that high temperatures resulted in shorter curing times were shown to have an increase in their mechanical properties [10].

This chapter discusses the various nanofillers used to manufacture PDMS based nanocomposite sensors, and the background of technologies used to manufacture these sensors. The chapter also highlights the various manufacturing techniques for bulk and porous PDMS as well as outline the scope of this work and research objectives.

1.1 Flexible Piezoresistive Nanocomposites

As discussed in the previous section, PDMS based nanocomposite sensors are manufactured by adding conductive nanofiller into a PDMS polymer matrix. Researchers have explored a variety of conductive nanofillers including carbon nanotubes (CNT), carbon nanofiber (CNF), carbon black (CB), graphene and metal nanoparticles. The incorporation of these particles induces a piezoresistive effect, which is defined as the change in electrical resistance that occurs when a force is applied to a semiconducting material. The etymology of the word is derived from the combination of two words, “piezo” which is stems from the Greek word “piezein” meaning

"to press or to compress", and "resistive" which stems from the Latin word "resistere" which means "to stop" [11]. The piezoresistive effect differs from the piezoelectric effect, whereby an electric signal is generated when a force is applied to a material. At the macroscopic level, the change in resistance outlined by the piezoresistive effect is governed by the equation

$$R = \rho \frac{l}{A} \tag{1}$$

whereby ρ is the material resistivity, l is the material length and A is the transverse cross-sectional area. In some materials, the piezoresistive effect is also as a result of the change in the resistivity. In this instance, there are changes in the inter-atomic spacing as a result of the application of strain. This affects the bandgaps, making it easier for electrons to rise into the conduction band, the electronic state of an atom which is closest to Fermi level and determines the electrical conductivity of the material. This phenomenon is governed by the equation

$$\rho_\sigma = \frac{\left(\frac{\partial \rho}{\rho}\right)}{\varepsilon} \tag{2}$$

whereby ρ_σ is the piezoresistive coefficient, $\partial \rho$ is the resistivity change, ρ is the original resistivity and ε is the strain [12]. Within PDMS based nanocomposites, the piezoresistive effect is caused by the tunneling effect, whereby the compression of the nanocomposite material reduces the distance between adjacent conducting nanomaterial such as CNTs, therefore resulting in a larger number of connections being formed between nanotubes [13]. The connection between nanotubes is essentially a critical distance required for electrons to jump from one nanotube to another, overcoming the insulation properties of the PDMS matrix. More connections between CNTs are produced due to the material being compressed further, and as a result the material experiences a decrease in resistance. The principles of the tunneling effect also apply to materials in tension. As

the material is stretched, the nanotubes pull away from their neighbors, resulting in connections being broken. This in turn increases the material's resistance. The other nanomaterials such as CNF, CB, graphene and metal nanoparticles also take advantage of the piezoresistive effect to various results.

1.1.1 Carbon Nanofibers

CNFs are cylindrical nanostructures with graphene layers stacked as either plates, cones or cups. They are a variant of CNTs, which are manufactured by wrapping graphene sheets into perfect cylinders. They are synthesized using the process of catalytic chemical vapor deposition which involves gaseous molecules being decomposed at high temperatures and carbon being deposited onto a substrate and allowed to grow with the help of a transition metal catalyst enclosing the growth. When CNFs are added into an elastomer matrix, the piezoresistive effect has been observed. Various researchers have fabricated such nanocomposites and their piezoresistive properties. Tallman et al. [14] fabricated highly flexible CNF/polyurethane nanocomposites for use in distributed strain sensing. The CNF and polymer were shear mixed at 7.5, 10.5, 12.5 and 15% filler volume fractions, and the resulting nanocomposite was cast into tensile bars. After being subjected to a sustained tension load, the samples displayed relative resistance changes of 27.9%, 11.7%, 5% and 6.6% for the CNF filler volume fractions of 7.5, 10.5, 12.5 and 15% respectively, thus showing good sensing response. A distributed strain sensing sensor fabricated using the samples was used to perform electrical impedance tomography was created in order to detect three different points of contact. The sensor clearly captures these three distinct points of contact at all fiber volume fractions, with lower volume fractions showing larger decreases in resistance. Other studies support these results [15, 16]. However, the sensing functions of the CNF/polyurethane nanocomposite contain hysteresis, as shown on Fig.1. Hysteresis is the phenomenon whereby the

value of a physical property lags behind changes in the effect causing it. In the field of highly elastic nanocomposites, hysteresis occurs when energy is dissipated during compression or tension loading and unloading as a result of material friction. This phenomenon affects the sensing function of a nanocomposite and generally results in sensitivity that is lower than full potential [17, 18]. Therefore, the CNF/polyurethane nanocomposite sensors do not work at full capacity as a result of hysteresis. Mapkar et al. [19] obtained flexible piezoresistive sensors by manufacturing functional nanofiber network composites (FNNCs) constituting a flexible silanol terminated PDMS matrix with CNF nanofillers. The CNFs were functionalized with PDMS groups in order to enhance the bonding between the matrix and filler and improve surface wetting. The PDMS functionalized CNFs (CNF-PDMS) was hand mixed with the silanol terminated PDMS (PDMS-OH), with poly(diethoxysiloxane) added as a cross linker. A tin based catalyst was used to initiate curing, and the sensors were molded by pressing the material between two sheets of wax paper and allowed to cure for 12 hours. Results showed very good dispersion of the CNF-PDMS compared to regular CNFs, with individual fibers observed under a Scanning Micron Microscope (SEM). This was a result of the improved surface chemistry between the CNF-PDMS and the PDMS-OH matrix. The samples shows drastic increases in stiffness, tensile strength and toughness compared to samples with regular CNFs. They showed decreases in the electrical conductivity compared to pristine samples, although the samples could still be used for sensing applications. From the mentioned studies involving flexible CNF nanocomposites, it can be concluded that the addition of CNFs to a polymer matrix proves the piezoresistive effect and results in functional sensors. However, their sensing capacity leaves room for improvement, especially compared to nanofillers such as graphene [20, 21]. Bulk samples have been shown to have the prevalence of hysteresis [22].

1.1.2 Carbon Black

Carbon black is a nanomaterial that has drawn great interest in the field of piezoresistive nanocomposite sensors. CB is fabricated through the incomplete combustion of heavy petroleum materials, and it has a paracrystalline structure with a high surface area to volume ratio. Researchers have shown that elastomeric nanocomposites with carbon black nanofiller have excellent piezoresistive properties. Shang et al. [23] fabricated and tested flexible piezoresistive nanocomposites by filling a silicone rubber matrix with a CB nanofiller. The ratio of CB:silicone used ranged from 0.01 to 0.2. CB, along with a silane coupling agent, was mechanically mixed with a water-ethanol binary solvent for 30 minutes. The resulting mixture was then added to the silicone rubber and stirred at 70°C in order to evaporate the solvent. The resulting powder was then mixed with the silicon matrix by mass ratio and subsequently dissolved in toluene. Mechanical mixing was combined with ultrasonic vibration in order to achieve good dispersion. A curing agent was included in the mixture, and the stirring occurred until the solvent evaporated fully. Samples were molded and cured at 55°C for 24 hours. The researchers found that the conductivity of the samples increases as the CB content increases, with a steep increase around 3 wt. % indicating a low percolation threshold. Essentially, a percolation behavior in piezoresistive nanocomposites is the phenomenon whereby the conductivity within the material increases with the increase in conducting nanofiller [24, 25, 26]. The percolation threshold is whereby the conductivity of the materials increases drastically until the saturation of the electrical networks is reached and the addition of conducting nanofiller no longer increases the conductivity of the material. The percolation threshold is dependent on the aspect ratio of the nanofiller, therefore materials mixed with nanomaterials that possess high aspect ratios reach the percolation threshold at lower nanofiller to matrix weight ratios. SEM results showed good dispersion of the CB particles

into the silicone matrix. The samples with a CB weight percentage 5% and higher showed a rapid increase in the conductivity at low compression pressure. The sensors display the piezoresistive mechanism well at CB weigh percentages higher than the critical weight percentage of 5%. The samples at different CB weight percentages showed very similar gauge factor values at all strains measured, almost all of the points lying on a reciprocal function. While proving repeatability of piezoresistivity for the homogeneous particle dispersion obtained by the fabrication method, these samples do not show the tunability of the samples' sensitivity, even with the variation of nanofiller content. Furthermore, the nanocomposite's sensing capacity was low compared to sensors with other conducting nanofillers. Other studies confirm this issue [27,28]. Wang et al. [29] fabricated their CB/silicone rubber nanocomposites for use in thin flexible pressure sensor arrays. The piezoresistive sensing element used in the sensor array was manufactured by mixing CB and the silicone rubber at a mass ratio of 0.08:1. Hexane was used as a solvent to mix the CB with the rubber. Mechanical mixing along with ultrasonic vibration was used to enhance particle dispersion, and the solvent was evaporated naturally during the mixing process. The resulting mixture was turned into a thin film via spin coating, and it was then vulcanized at 30°C for 40 hours. SEM characterization showed good dispersion of CB particles within the silicone rubber matrix. Overall, the samples showed a good piezoresistivity mechanism, with a pressure measurement range of 0-1 MPa and a maximum measurement deviation of 30 kPa. This measurement range satisfies engineering applications, however the sensor does not capture measurements at low stresses very well. Research teams such as Shimojo et al. [30] have successfully fabricated more sensitive sensors. Furthermore, the sensor had a significant hysteresis error of 1.3% which came about as a result of the sample's bulk nature. From looking at published studies detailing the fabrication of highly flexible piezoresistive CB nanocomposites, it can be concluded that tuning the sensitivity

of the sensors is difficult and is not easily achieved by varying the CB content. Also, there is a presence of hysteresis error that limits the sensitivity of the sensors.

1.1.3 Graphene

Graphene is an allotrope of carbon that takes the form of a single layer of atoms in a two-dimensional structure, with one atom forming each vertex. Graphene exhibits excellent mechanical, electrical and thermal properties, possessing low density and great versatility [31]. It can be used to manufacture other carbon-based nanofillers such as graphite, CNTs, CNFs and fullerenes. It has excellent tensile and compressive strength, with values that are over 100 times greater than steel [32]. Nanomaterials manufactured with graphene nanofillers are able to reach the percolation threshold at a lower filler content compared to other conductive nanofillers, due to graphene's high surface area. Due to its favorable properties, researchers have widely studied the piezoresistive effect of flexible polymer matrices reinforced with graphene. Hou et al. [33] fabricated a nanocomposite sensor using PDMS with a conductive alkyl-functionalized graphene (G-ODA) nanofiller. The researchers highlight the widely observed poor dispersion of graphene in non-polar polymers. The nanomaterial in its pristine form fails to bond effectively to the polymer matrix, even when proven effective techniques to disperse nanomaterials such as solvents and ultrasonication is utilized. The research team solved this issue by performing one-pot synthesis of G-ODA using graphene oxide (GO) and octadecylamine. The flexible G-ODA/PDMS nanocomposite was fabricated using a wet mixing approach, utilizing xylene as a solvent. The percolation threshold was reached at the low nanofiller volume percentage of 0.63%, and the sensors displayed the piezoresistive effect well under compression. The sensors displayed tunability of conductivity, with the variable increasing with an increase in nanofiller content. The sensors also showed a significant decrease in the material hysteresis compared to CNT/PDMS

sensors. Fig.1 shows the sensing functions of the sensors fabricated using CNTs and G-ODA nanofillers. The differences in the sensing functions of the two material highlights the effect of hysteresis on the piezoresistive sensing function, with Fig.1(b) showing sensors (CNT/PDMS) with a relatively high amount of hysteresis. The sensors display a greater level of material relaxation whereby the resistance change within the material decreases in cyclic loading of the same strain and strain rate. The relative resistance change does not exactly align with the pressure applied in magnitude, implying poor repeatability as a consequence. The material with greater hysteresis also has two "troughs" whereby as the relative resistance (R/R_0) change nears the maximum value, it suddenly increases into a mini "peak" then continues to decrease to the maximum value. The sudden decrease in the R/R_0 occurs during the loading cycle, a phenomenon that is not supposed to occur in ideal circumstances. The mini "peak" prevents the R/R_0 from continuing to increase, therefore limiting the overall piezoresistive sensitivity of the material. Therefore, the G-ODA/PDMS sensors saw an improvement in the sensing potential compared to the CNT/PDMS sensors. However, the G-ODA sensors saw a decrease in the piezoresistive sensitivity with an increase in filler content, while the CNT sensors had their sensitivity increase with the increase in nanofiller. This means that, at 1.19% filler volume, the G-ODA/PDMS material showed less piezoresistive sensitivity compared to the CNT/PDMS material. This was due to the fact that the most possible connection forms of the CNT network are either point-point or point-line contact due to the one dimensional property of CNTs, and the addition of more CNT into the polymer matrix does not interfere with other conducting networks until the percolation threshold is reached, due to the small lateral surface area. G-ODA forms a conducting network with line-plane and plane-plane contact due to its two dimensional properties, which means that the addition of more G-ODA results in the nanofiller interfering with formed conducting paths,

and thus the material reaches the percolation threshold at lower nanofiller content. However, these two different orientations of the nanofillers have a different effect on the hysteresis. Since CNTs have point-point and point-line contact, when pressure is applied and the material is compressed it is more beneficial to induce destruction of certain networks, resulting in the sudden mini "peak" on the sensing function which is essentially a decrease in the R/R_0. The line-plane and plane-plane contact which occurs with G-ODA is stable and does not break down when pressure is applied and the material is compressed. This phenomenon is instrumental in limiting the effect of hysteresis with G-ODA/PDMS nanocomposite sensors.

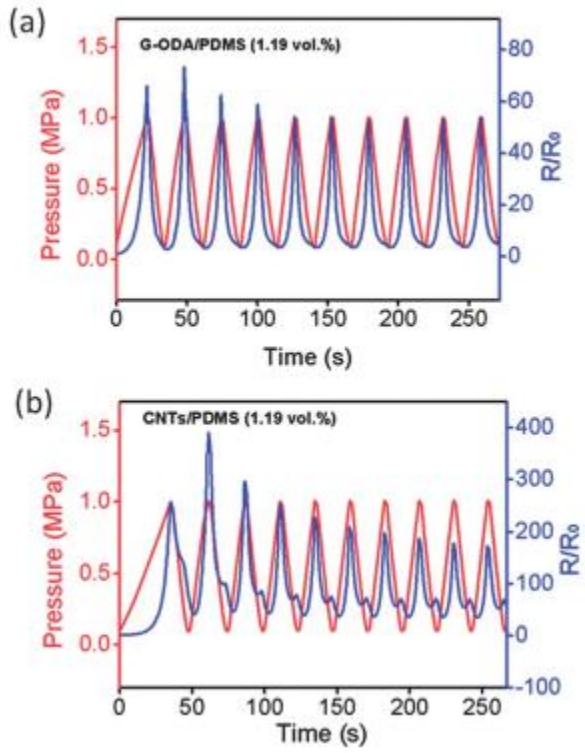

Figure 1: Pressure and R/R_0 vs time of G-ODA/PDMS and CNT/PDMS (Hou et al.)[33]

Tung et al [34] used a different approach to fabricate their flexible graphene/polyurethane nanocomposite sensor. Instead of functionalizing the surface of graphene in order to allow it to

bond more easily to the polymer, the researchers decorated the graphene with magnetite nanoparticles which acted as nanospacers between graphene nanoplatelets and utilized poly(ionic liquid) to stabilize the mixture. SEM characterization showed good dispersion, with full exfoliation of magnetite decorated graphene platelets. Sensing results showed high sensitivity, with a low threshold pressure of 0.5 kPa. The sensors had low hysteresis within the loading and unloading cycle, further highlighting the stability of 2D graphene nanoplatelets within a conducting network. The sensing functions of the sensors did not have the mini "peak" associated with high amounts of hysteresis, and they did not contain the drift in the cyclic relative resistance change sensing function as a result of material relaxation commonly associated with hysteresis. From the two studies mentioned, as well as a variety of other studied conducted on the piezoresistivity of graphene polymer nanocomposite sensors, it can be concluded that such polymer nanocomposites have excellent conductivity and sensitivity, and they are able to detect very low pressures compared to nanocomposites with other nanofillers. Sensors manufactured using these materials also significantly reduce hysteresis within the bulk material, resulting in them fulfilling their tasks at close to full sensing capacity. While graphene is ideal in fabricating flexible nanocomposite sensors, it does have a few disadvantages. It provides poor tunability of the sensitivity since the addition of more graphene into a polymer matrix results in the sensitivity remaining the same or decreasing after the low percolation threshold is reached [35]. Graphene is also a very expensive material compared to other nanofillers such as CNFs, CNTs and CB. The cost of graphene currently lies between $100,000 -$300,000 per kg, making it highly uneconomic and impractical when attempting to design low cost tactile sensors. Furthermore, graphene in its pristine form is difficult to disperse into a polymer matrix [36]. In order to successfully disperse it, researchers alter its surface through functionalization or incorporate other nanoparticles onto the structure of

graphene in order to facilitate bonding with the polymer matrix [37]. These processes are complex and difficult to perform, and the chemicals involved are hazardous and prone to exploding.

1.1.4 Carbon Nanotubes

CNTs are cylindrical nanostructures made from carbon atoms, and they can be differentiated into two distinct types. Single-walled CNTs (SWCNTs) are essentially section of two-dimensional graphene that has been rolled up to form a hollow cylinder, and they lie in the range of one nanometer. Multi-walled CNTs (MWCNTs) consist of SWCNTs that are nested together, with typical diameters lying in the range of 100 nanometers. CNTs possess very good electrical and thermal properties, and they have remarkable tensile strength [38]. They have a high aspect ratio as a result of their long structure and small diameter, meaning that CNT/polymer nanocomposites reach the percolation threshold at a relatively low nanofiller content [39]. They are therefore exceptional candidates to act as conductive nanofiller within flexible polymers in order to produce piezoresistive sensors, and extensive research has been done to fabricate and optimize such sensors. Kang et al. [40] fabricated a nanocomposite sensor consisting of a polyimide matrix with SWCNTs nanofillers. The CNTs were dispersed into the polymer matrix using mechanical mixing and ultrasonication, with 0.05% their weight reaching the percolation threshold. SEM characterization showed that good uniform dispersion was achieved. Regarding the piezoresistive results, the piezoresistive sensitivity increased with the increase in nanofiller content, and the highest sensitivity was reported at the percolation threshold. A gauge factor of 4.5 was recorded, however there was the significant effect of hysteresis present in the sensing functions. Cattin et al. [41] studied the piezoresistive effect in polymer nanocomposites with nanofillers that have a high aspect ratio. The researchers fabricated the sensors using Vinyl Methyl Silicone (VMQ) rubber and PDMS as the polymer matrices, and they utilized MWCNTs with

different aspect ratios (ARs) as well as graphene as the conductive nanofiller. The nanofiller was dispersed using a combination of shear mixing and ultrasonication, using toluene as a solvent. Good dispersion was achieved with little agglomeration occurring. As predicted, the electrical results showed that the VMQ nanocomposite with the highest aspect ratio MWCNTs (AR of 500) showed the greatest piezoresisitive sensitivity, while the VMQ/MWCNT nanocomposite with an AR of 50 resulted in the second lowest sensitivity. Generally, nanocomposites endowed with CNTs as conductive nanofiller display the piezoresistive effect excellently. Due to their high AR and one-dimensional properties, they achieve the percolation threshold at low nanofiller content [42]. They also provide a small level of tunability when the polymer matrix, CNT aspect ratio and filler weight percentage are varied. Moreover, CNTs are much cheaper than graphene, making them viable in economic nanocomposite sensor design. As a result, they were chosen to be the conductive nanofiller for this study.

1.2 Fabrication Techniques of PDMS Based Nanocomposite Sensors

There currently exists wide variety of methods for producing PDMS based piezoresistive sensors. For the purpose of this study, these manufacturing processes are divided into two main sections, the fabrication of bulk and porous nanocomposite sensors. This is done to differentiate between these two sensor types and highlight the differences in their mechanical and piezoresistive properties.

1.2.1 Bulk Sensors

Bulk nanocomposite sensors, being substances that have been cured into solid shapes with minimal or no pores present, have drawn significant attention from researchers due to their relative ease of manufacturing. Bulk materials are manufactured using techniques such as cast molding

[43] and additive manufacturing [44]. Cast molding is largely seen as a conventional manufacturing method for nanocomposite sensors due to its frequency of use. Studies discussed in Section 1.1 involve bulk sensors that were manufactured largely using cast molding and other related conventional methods. The cast molding process is quick and easy, and it does not usually require significant post processing [45]. However, the topology of sensors manufactured using cast molding is limited to the shape of the mold, therefore complex geometry is difficult to achieve. This makes it particularly taxing to customize the sensor design. Cast molding incorporates more processes into the fabrication of sensors such as the design and manufacturing of the mold and post processing of the sample, making the entire process costly and time-consuming. Cast molding also results in significant voids and defects that affect the mechanical [46] and electrical properties [47] of nanocomposite sensors. Furthermore, cast molding is not economical for mass production compared to other manufacturing processes. Due to these limitations, additive manufacturing has garnered significant attention from researchers studying highly flexible piezoresistive nanocomposites.

Additive manufacturing, also referred to as 3D printing, is a computer manipulated process that creates objects by depositing materials in layers. Additive manufacturing processes commonly used include Stereolithography Apparatus, Digital Light Processing, Selective Laser Sintering, and Fused Deposition Modeling. Additive manufacturing processes can be divided into five main types; vat photopolymerization which involves the use of liquid photopolymers that can be cured using ultraviolet radiation, powder bed fusion which includes a thermal source malting and fusing powder particles, extrusion-based systems whereby material contained in a reservoir is forced through a nozzle when pressure is applied, material jetting which involves the deposition of material particles or droplets, binder jetting whereby a liquid binder is printed onto a powder bed,

sheet lamination which involves the layer-by-layer lamination of thin sheets of materials that are held together by adhesive bonding or cold welding, directed energy deposition whereby powder material is melted as it is deposited, and direct ink writing which involves the deposition of liquid inks to a surface that solidify due to evaporation and gelation [48]. The 3D printing process begins with the design of the desired object using Computer Aided Design (CAD). The CAD file produced has to be converted to a Stereolithography (STL) file, which is a collection of triangle vertices and surface normal vectors. The STL file is then inserted into a slicing software which produces a layer-by-layer model written in gcode, a coded set of instructions that are submitted to the 3D printer's control system to execute the sliced model. The slicing software takes into consideration the printing parameters set by the user which include layer height and thickness, printing speed, bed temperature, as well as the density and type of infill. With regards to flexible piezoresistive nanocomposites, additive manufacturing holds a significant advantage over conventional methods such as cast molding. Firstly, additive manufacturing enables mass production due to its semi-automation. It allows for the fabrication of complex and organic geometries, and it enables rapid prototyping which is beneficial in the optimization of geometries and processes enabled by Computer Aided Evaluation (CAE) techniques. Additive manufacturing significantly decreases process time and labor, and it results in better component quality. In the field of piezoresistive nanocomposites, 3D printing technologies have been shown to improve the piezoresistive sensitivity of sensors. Charara et al. [49] used DIW to fabricate a MWCNT/PDMS nanocomposite sensor with increased sensitivity. A gauge factor of 16 was recorded, an improvement compared to those of cast MWCNT/PDMS compression sensors found in literature [50]. However, the effect of hysteresis was recorded. As a result, the 3D printing technology used in this study is Direct Ink Writing (DIW), due to its numerous advantages.

While bulk material sensors have numerous uses and advantages, the effect of hysteresis is prevalent within them. This phenomenon reduces their sensing capacity and induces the material relaxation effect. Researchers have been successful in reducing the effect of hysteresis by incorporating graphene nanofillers, however this nanomaterial is costly and allows for little tunability of the sensitivity. While the hysteresis effect is still not well understood, one of the possible causes could be the lateral expansion of the material as it is compressed, resulting in gaps in the conducting networks.

1.2.2 Porous Sensors

Porous piezoresisitive sensors have received a great deal of scrutiny due to their hightened flexibility and sensitivity. Porous sensors have also been shown to possess significantly higher tensile fracture strain compared to bulk samples, and they can be compressed to almost 100% strain without fracturing. Moreover, they possess tremendous stress sensitivity due to their low stiffness, regardless of the conductive nanofiller [51]. Porous piezoresistive sensors are usually manufactured by introducing conductive nanofiller to already manufactured porous polymer foams. These foams are manufactured using a variety of methods including templating, emulsion, gas foaming and 3D printing. Templating involves using a soluble solid material such as sugar and salt grains as a porogen, with the polymer taking up the surrounding space. The porogen is then dissolved, leaving behind pores within the cured polymer. The templating technique is a simple method of achieving a three-dimensional interconnected pore structure. Wu et al. [52] used the templating technique to fabricate porous CNF/PDMS nanocomposite sensors. Brown sugar, used as a porogen, was coated with CNFs using isopropanol as a solvent, and the mixture was compacted into a thin sheet template using a hydraulic press. Infiltration of PDMS was facilitated by a vacuum oven, and the sugar was dissolved using bath sonication. The porosity achieved was

79%, and the samples where loaded in tension in order to test the piezoresistive effect. The sensors were found to be highly sensitive, with the gauge factor increasing from 1.0 to 6.5 when the CNF content is decreased from 2.8 to 0.1 wt %. The sensors also saw relative resistance changes as high as 620% at 40% applied strain. Furthermore, the sensors showed minimal hysteresis and material relaxation, with a recovery time of 3.982s that is significantly faster than the 100s and 50s values recorded by bulk material CB/thermoplastic and SWCNT/PDMS sensors respectively [53, 54]. Templating allows for the tunability of pore size with the use of different sized grains as the porogen. Emulsion involves utilizing the hydrophobic properties of PDMS and other similar polymers and dispersing emulsion droplets that become the porogen. Huang et al [55] manufactured pristine closed pore PDMS foam by using a shear mixer to disperse water into PDMS, creating an emulsion. The researchers found that the increase in porosity resulted in a decrease in the stiffness of the foam. However, this stiffness is significantly greater than those of pristine PDMS foams with 3D interconnected pores due to its closed pore nature. Emulsion also provides a measure of tunability of the pore size through the altering of the shear mixing rate. Gas foaming involves the blending of a chemical that produces gas bubbles within the polymer matrix. Yang et al [56] utilized gas foaming to manufacture CNT/polystyrene foam nanocomposites. Polystyrene and CNTs were blended with the help of a solvent, and 2,2'-azoisobutyronitrile (AIBN) was used as a foaming agent. Gas foaming does not provide the tunability of pore size since it depends on the chemical reaction that releases the gas bubbles, and these are often hard to precisely control. 3D printing of porous structures has been achieved a variety of novel techniques. Alison et al. [57] utilized sacrificial templating to 3D print porous nanocomposites. The researchers prepared nanodroplets and micro-templates that were incorporated into 3D printing ink. Pores were generated by removing the nanodroplets and micro-templates after the 3D printing

process. Mu et al [58] 3D printed a porous polymeric material by utilizing a photocurable resin. The researchers used Digital Light Processing, a vat polymerization 3D printing technique that scans an entire layer at one time. Porosity was achieved by incorporating selectively sieved salt powders in the photopolymer. A method of controlling the porosity using 3D printing involves varying the infill pattern and density. Slicing software offers a variety of infill patterns, such as grid, triangular, rectilinear and honeycomb. This study focuses on using infill patterns and infill density to additively manufacture porous flexible PDMS based nanocomposites.

Researchers fabricating porous PDMS based nanocomposites using 3D printing are faced with numerous challenges. Firstly, pristine PDMS does not hold its shape well after extrusion, and it does not keep its shape when subsequent layers of material are deposited above it. Regarding its rheological properties, PDMS does not have a yield point, meaning that it will collapse upon extrusion. The addition of CNTs improves the rheological properties, endowing the material with a yield point. However, this yield point is still below the requirement for 3D printing sensors with intricate infill patterns. Therefore, a thixotropic filler is incorporated in order to increase the yield point significantly while not compromising the nanocomposite's piezoresistive sensitivity.

1.3 Scope of Work

In summary, PDMS based nanocomposite sensors have a variety of applications in different scientific fields. They display the piezoresistive effect whereby their conductivity changes due to mechanical load. The structures' piezoresistive sensitivity is determined by a wide range of factors such as the type of nanofiller, the different manufacturing techniques and the amount of porosity within the material. Compared to other conductive nanofillers, CNTs are light, low cost, and have excellent mechanical and electrical properties. They have a high aspect ratio,

meaning that they reach the percolation threshold at low filler content. There is a multitude of methods used to manufacture PDMS based nanocomposite sensors, however 3D printing stands out due to the fabrication of complex and organic geometries, the enabling of mass production due to its semi-automation, and the decrease in process time. Current work involving the 3D printing of PDMS based nanocomposite sensors concerns bulk material sensors, which have been shown to contain significant levels of hysteresis that limits their sensing capacity. Porous sensors possess low hysteresis while being highly sensitive. They also possess greater fracture strains compared to bulk samples. Many techniques for fabricating porous polymer structures exist, however the use of 3D printing remains a novel approach. Therefore, this study proposes a formulation of CNT/PDMS nanocomposite material with a thixotropic silica filler. An investigation of the morphology of 3D printed porous CNT/PDMS nanocomposites also be conducted, as well as a characterization of their sensing performance compared to bulk material sensors of the same material, proving that the introduction of porosity via 3D printing significantly reduces the hysteresis and improves sensitivity. Lastly, a characterization of the mechanical properties of the porous sensors will be performed, and a Finite Element Analysis will be conducted to predict the location of failure.

1.4 Research Objective

The research objectives of this study are as follows:

a) Formulate a CNT/PDMS nanocomposite ink with thixotropic silica filler for improved yield point, to allow for functional 3D printing
b) Characterize the porosity, pore size and pore structure of the printed sample
c) Characterize the piezoresistive performance and compare to bulk sample

d) Investigate the mechanical properties and perform a Finite Element Analysis

Chapter 2. Material Formulation and Sensor Fabrication

2.1 Introduction

This chapter highlights the material formulation of the CNT reinforced polymer nanocomposite used to manufacture 3D printed porous sensors, as well as the 3D printing technique used. Porosity is introduced to the sensors through the varying of the infill density and pattern, a technique which requires the nanocomposite ink to possess very good rheological properties. The ink not only must possess a yield point upon extrusion whereby it holds shape and can support subsequent layers on top of it, but it should have a high yield point to support the layer printing of lines required for porosity achieved by varying infill densities. With most infill patterns and densities, single lines of ink support other lines above them without any lateral support. This is different from bulk material sensors which have material from adjacent ink lines providing support. However, the material should still retain flexibility after curing and not be brittle. Certain thixotropic agents used to increase the yield point and enable such 3D printing reduce the flexibility of the material, an unwanted phenomenon in the fabrication of flexible porous CNT reinforced nanocomposite sensors since it reduces the sensing range and fracture strength of the material. Therefore, the ink must contain a thixotropic filler that does not result in a brittle sensor.

2.2 Material Formulation

2.2.1 Materials

All materials were used as purchased unless specified. PDMS of varying viscosities was purchased from Gelest. The PDMS was purchased in the form of vinyl terminated PDMS with 100 cSt viscosity (D-1), vinyl terminated PDMS with 1000 cSt viscosity (D-2), dimethylsiloxane copolymer (H-1), and a platinum based catalyst to facilitate cross-linking. A thixotropic silica filler

was purchased from PPG Industries, Inc. MWCNTs with a diameter range of 50-90nm and an aspect ratio of 100 were purchased from Sigma Aldrich.

2.2.2 Fabrication of Nanocomposite Ink

A predetermined amount of D-1, D-2, H-1, silica filler and MWCNTs was added to a glass container and shear mixed at 2000 rpm for 45 minutes in order to achieve a good blend and uniform dispersion of the CNT nanofiller. The molar weight ratio of the combination of D-1 and D2 to H-1, known as the HMS: DMS ratio, is maintained at 2.8385 at all mixtures studied according to manufacturer specifications. Table 1 shows the different material formulations at four silica weight percentages, highlighting the weight percentages of each constituent in the PDMS mixture. A MWCNT content of 1.5 wt% was selected for all nanocomposite ink formulations studied since it produced an efficient electrical response [63]. Percolation theory dictates that an increase in the weight percentage of conducting nanofillers in piezoresistive polymer nanocomposites results in an increase in the material's electrical conductivity until saturation is reached. Therefore, 1.5 wt% of CNTs was chosen since it is a relatively low weight percentage that has reached the percolation threshold, thus reducing costs. This weight percentage is also easier to disperse, while providing a good sensing response to mechanical loads. The container with the mixed material was then placed in a vacuum chamber desiccator at a pressure of 28.5-29 in Hg for 30 hours in order to remove air molecules that were trapped during the shear mixing process. Once the desiccation was completed, 0.02 wt% of the platinum based catalyst was added before the 3D printing process began in order to facilitate cross linking. The material formulation process is shown on Figure 2.

Table 1: Composition of Each PDMS Formulation

D-1 (wt %)	D-2 (wt %)	H-1 (wt %)	Silica (wt %)	CNT (wt %)
29.6926	29.6926	34.1149	5	1.5
28.1047	28.1047	32.2905	10	1.5
26.5169	26.5169	30.4662	15	1.5
24.9291	24.9291	28.6419	20	1.5

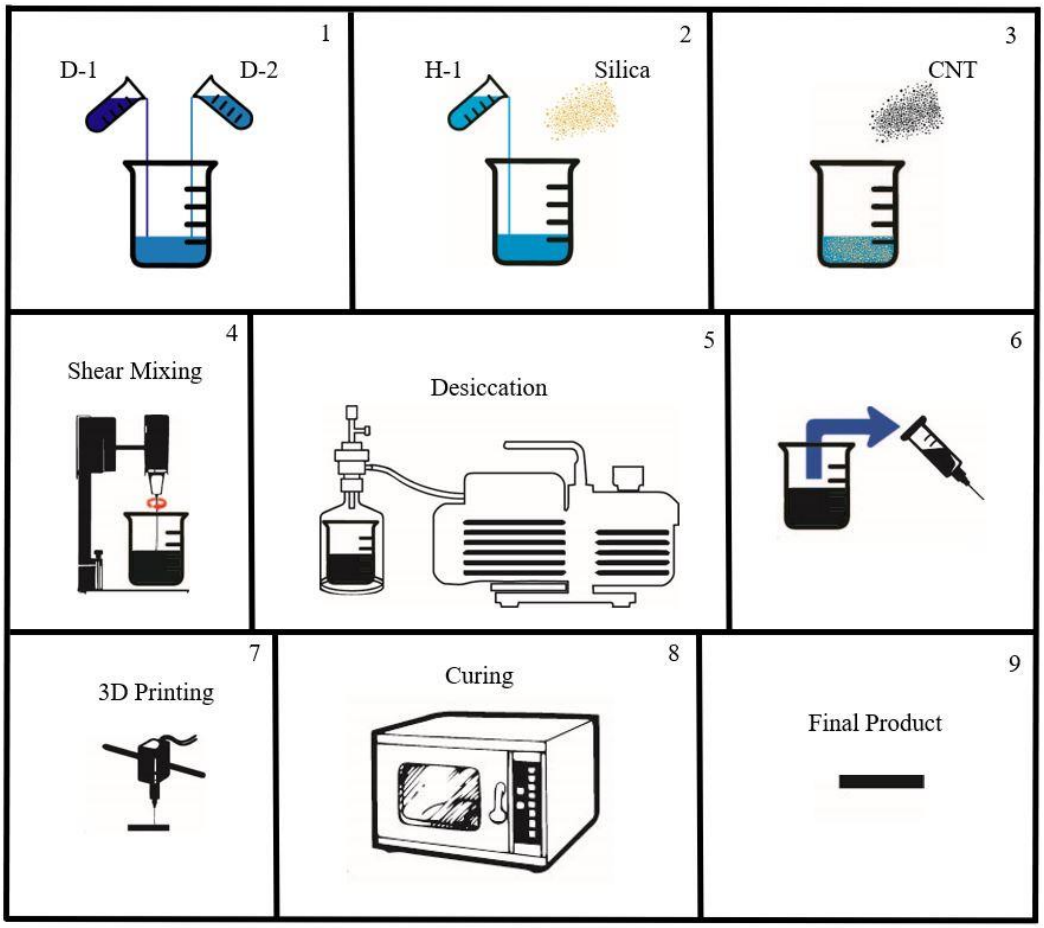

Figure 2: Flowchart of material formulation of CNT/PDMS nanocomposite ink, and sensor fabrication process

2.3 Rheology

2.3.1 Testing Procedure

The analysis of the rheological properties of the nanocomposite ink, essentially the manner in which the material flows when a force is applied, is important in realizing 3D printed porous sensors. In order to understand these properties, rheological tests were conducted using a TA Instruments Discovery HR2 rheometer. Firstly, peak hold tests were conducted on the nanocomposite ink at different silica concentrations in order to analyze the material's shear thinning behavior. The material was placed on a test plate, and a 40 mm diameter cone fixture with a 2° angle was used to apply constant oscillatory shear for 60 seconds at shear rates between 100 s^{-1} and 2500 s^{-1}. These tests were followed by amplitude sweep tests, whereby a different material was placed on the test plate and a sweep was performed at varying oscillatory shear values with a step rate of 5 Pa starting at 1 Pa in order to determine the yield stress. Both tests were performed on nanocomposite ink without the platinum catalyst since the test length exceeded the curing time, therefore the results would be affected by the gelation of the material.

2.3.2 Rheology Results

Tests were conducted to determine the nanocomposite ink's shear thinning behavior [64]. Shear thinning behavior is the tendency of certain liquids and solids to experience a decrease in viscosity when a force is applied. Essentially, materials exhibiting shear thinning behavior flow more when a pressure is applied, and their viscosity returns to its initial state once the pressure is removed. Figure 3 shows the shear thinning behavior of four different CNT/PDMS nanocomposite formulations, each with a different silica concentration. From the graph, it is evident that all the material formulations display shear thinning behavior. Each material's viscosity decreases as the

shear rate increases until a minimum value is reached. All four material formulations show higher shear thinning at low shear rates, and the behavior lessens as the shear rate increases until the minimum value is reached. The material formulation with a 20 wt% of silica had the highest viscosity, while the 20 wt% silica formulation had the lowest viscosity at the shear rates tested, as expected. These results mean that all the material formulations can be extruded out of syringe needle when pressure is applied.

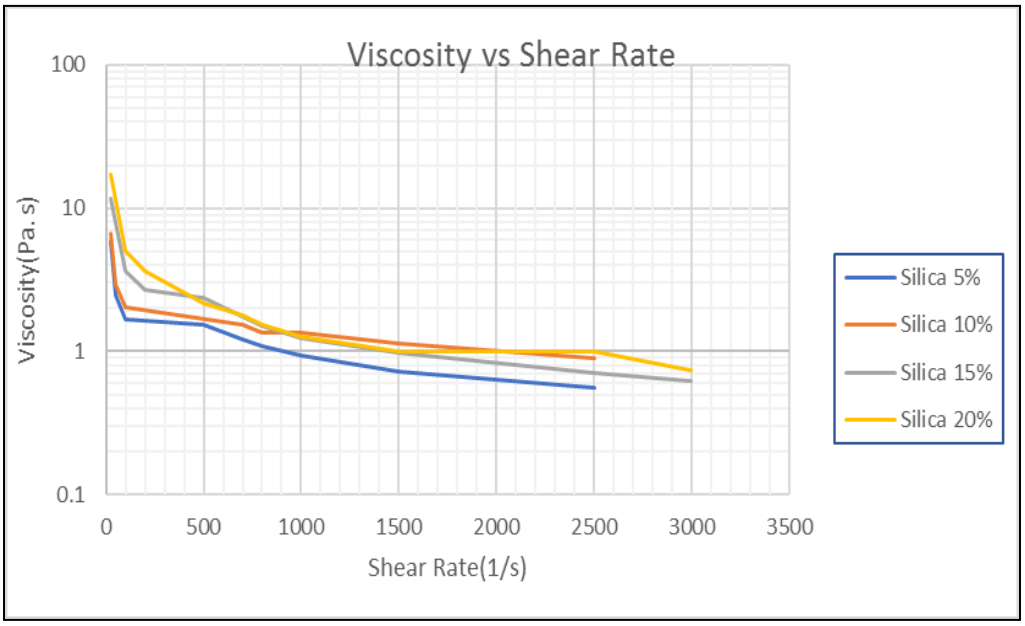

Figure 3: Shear thinning behavior of CNT/PDMS nanocomposite with various silica filler concentrations

Amplitude sweep tests were conducted in order to determine the yield stress of the CNT/PDMS nanocomposite formulations. The yield point in rheology is defined as the lowest shear stress at which the material changes from behaving like a liquid to behaving like a soft solid. The oscillation stress at which this occurs is important since it determines how well the soft solid holds its shape upon extrusion. Figure 4 shows the storage modulus (G`), essentially the elastic

behavior of the material when deformed, and the loss modulus (G``) which is the viscous property that reflects the flow of a material during deformation. These two variables are shown as a function of the oscillation stress for the four silica weight concentrations. The yield point of the material is defined as the point where the storage and loss modulus curves intersect and cross over, with the oscillation stress value at which the cross over occurs identified as the yield point stress. From Figure 4, it is evident that the yield point stress increases with an increase in the silica filler weight percentage, with 5 wt% silica ink having the lowest yield stress and the 20 wt% silica ink showing the highest value. This increase is highlighted in Figure 5, which shows the yield stress as a function of the silica concentration.

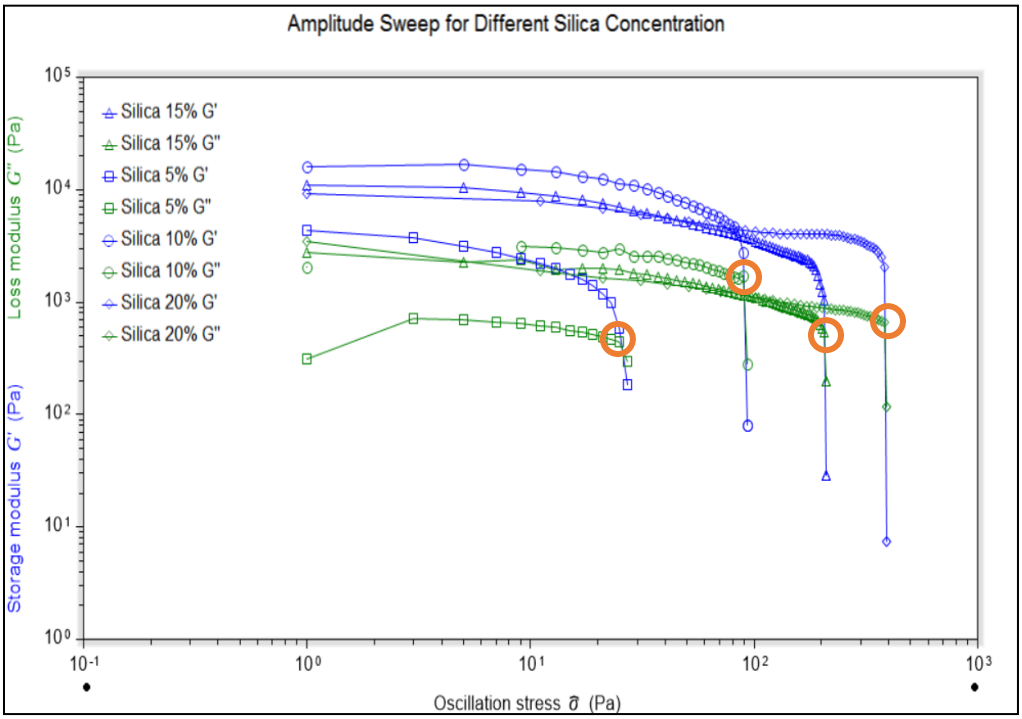

Figure 4: Amplitude Sweep of various silica filler concentrations

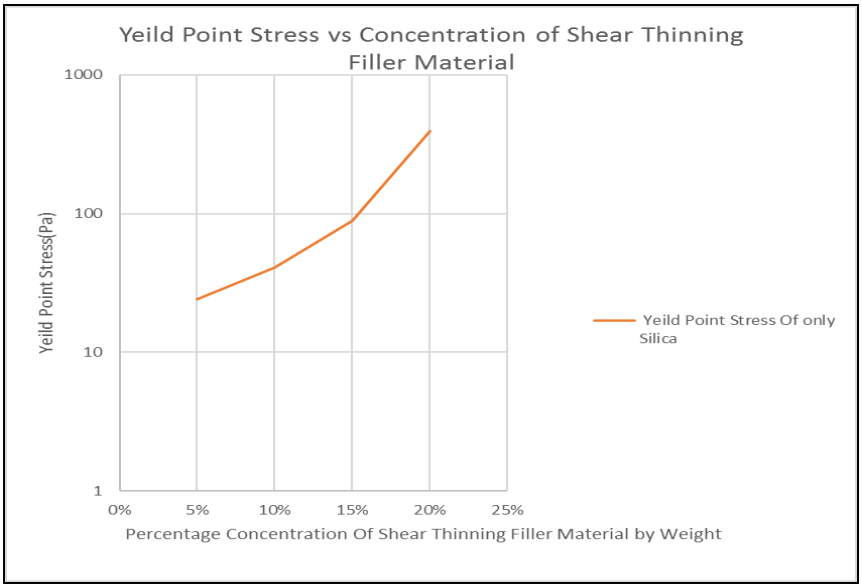

Figure 5: Yield Point Stress of different silica filler concentrations

Regarding the 3D printability of these material formulations, the 5 wt% silica formulation showed significant spreading after printing. There was a level of collapse which lead to the layers blending with each other to a small degree. While a bulk material samples could be 3D printed at this concentration, the material does not adhere to the geometric accuracy required for sensors with varying infill. The 10 and 15 wt% silica formations achieved good geometric accuracy with sensor height and layer thicknesses that varied very slightly from the model values, with the 15wt% formulation showing greater consistency. While the 20wt% silica formulation held the best shape upon extrusion and showed the best geometric accuracy, the sensors produced using this material showed substantial brittleness and low fracture strength. Therefore, the 15wt% silica nanocomposite ink formulation was chosen for this study due to its high yield point and geometric accuracy upon 3D printing while retaining its hyperelasticity and high fracture strength.

2.4 3D Printing

2.4.1 Fabrication Process

The 3D printing process was completed using an in-house modified 3D printer with an extrusion system driven by a pneumatic pump. The geometries chosen were a cuboid with the dimensions of 13 mm x 13 mm x 2.05 mm to be used as compression sensor, and thin, one layer rectangular sheets with the dimensions of 13 mm x 50 mm x 0.41 mm and 13 mm x 50 mm x 0.26 mm to be mechanically tested in tension. Firstly, solid models of the three geometries mentioned were created using the Computer Aided Design (CAD) software Solidworks. The Solidworks part file (SLDPRT) was converted to an STL file and transferred to the 3D printing application Repetier-Host which sliced the model and produced gcode using print settings imported from Slic3r. The printing parameters incorporated into the fabrication of these geometries include a 5 mm/s printing speed, as well as layer heights and thicknesses of 410 µm and 260 µm. The layer height and thickness values correspond to the two nozzle diameters used in this study. In order to introduce controlled porosity into the sensors, the three infill patterns grid, triangle and honeycomb were introduced, as well as the infill densities of 20%, 40%, 60% and 100%. Once the gcode was generated and uploaded onto the 3D printer's control system, the platinum-based catalyst was mixed into the MWCNT/PDMS nanocomposite ink with 1.5 wt% CNT and 15 wt% silica. The mixture was loaded into a 3 mL pneumatic pump syringe and capped with the syringe nozzle. The syringe was secured onto its housing which is part of the extrusion system on the 3D printer. The gcode was run and the geometries chosen were printed on an aluminum plate for easy transportation. The nanocomposite ink was pushed by pneumatic pressure of 20 psi out of the 410 µm nozzle, and a pressure of 40 psi out of the 260 µm nozzle. Once the 3D printing process was completed, the samples were placed in a forced convection oven at 80°C for 3 hours to cure.

Figures 6-9 shows the sliced models with the incorporated infill patterns and densities, as well as the different nozzle diameters. The compression sensor models at the nozzle sizes of 410 and 260 µm are highlighted in Figures 6 and 7. Thus the variation of the infill pattern and density could be analyzed to determine how it affects the porosity, as well as the electrical and mechanical behavior of the sensors. The infill patterns are essentially single lines of ink being placed on top of each other in grid, triangular and honeycomb patterns, highlighting the importance of 3D printing ink with a high yield stress point that can hold very good shape in one-line thick walls. Five layers of the 410 µm layer height and thickness models was generated, while eight layers of the 260 µm models was created, fulfilling the 2.05 mm height determined for all the compression sensors. Sliced models of the tension samples printed in a grid pattern are shown in Figure 8. The pore sizes of the tension models at each infill pattern and density are equal to those of the compression models. That is, the grid pattern model at 20% infill has the same pore size and shape at both the compression and tension models. Figure 9 shows the models used to print the equivalent bulk material samples. The rectilinear print pattern was chosen since the slicing software was unable to generate 100% infill density at grid, triangle and honeycomb infill patterns. There are two bulk tension models produced, with the rectilinear pattern arranged in a longitudinal and lateral orientation. This was done in order to study the mechanical strength of these two orientations.

(a)

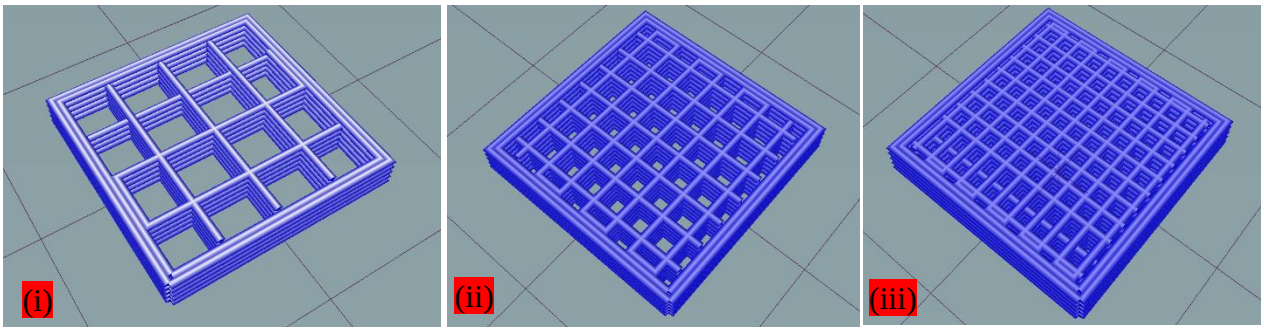

(b)

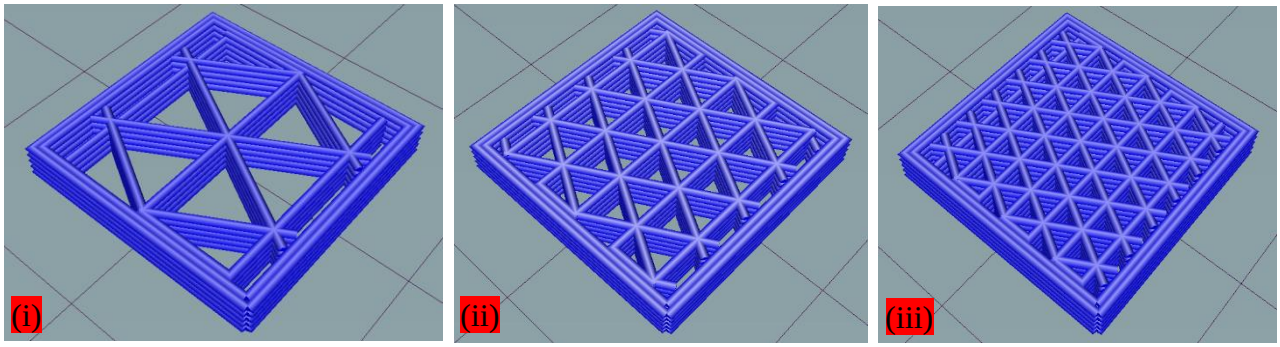

(c)

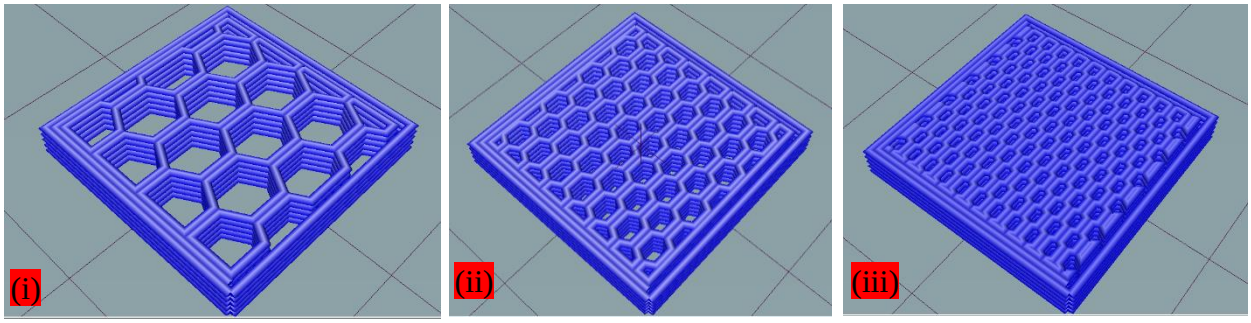

Figure 6: Sliced 3D models of compression sensors with (a) grid, (b) triangle and (c) honeycomb infill patterns at (i) 20%, (ii) 40% and (iii) 60% infill density with 410µm layer height and thickness

(a)

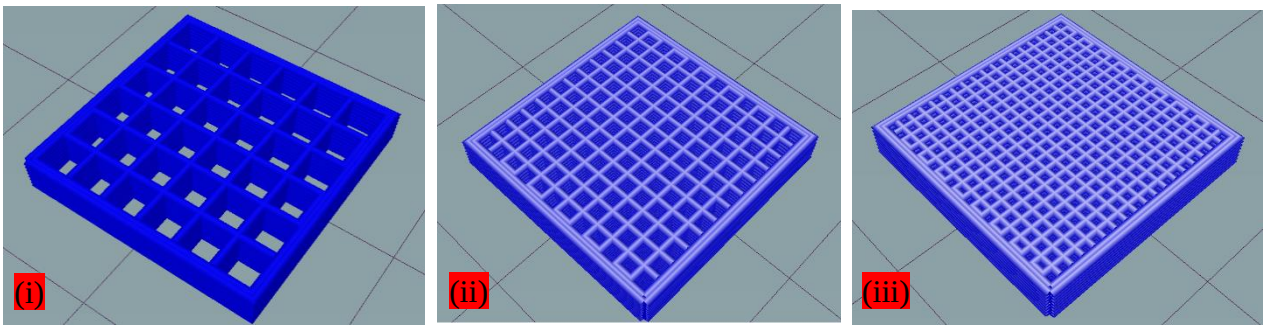

(b)

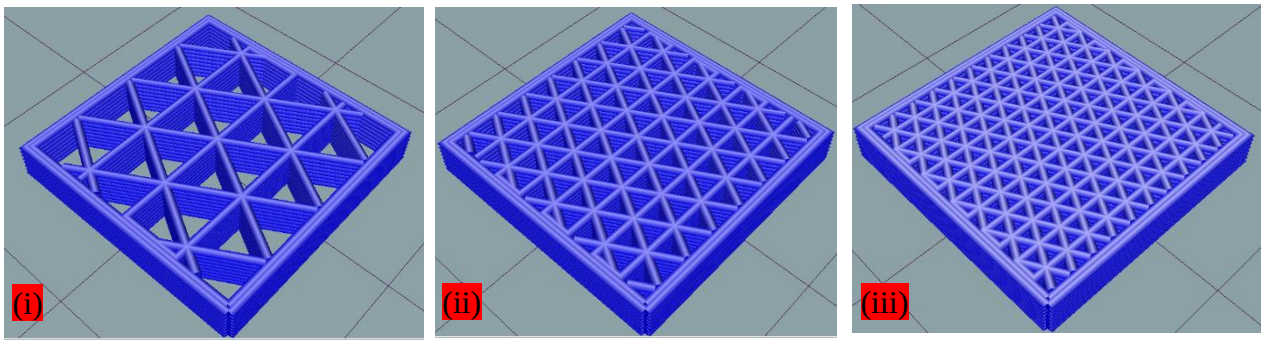

(c)

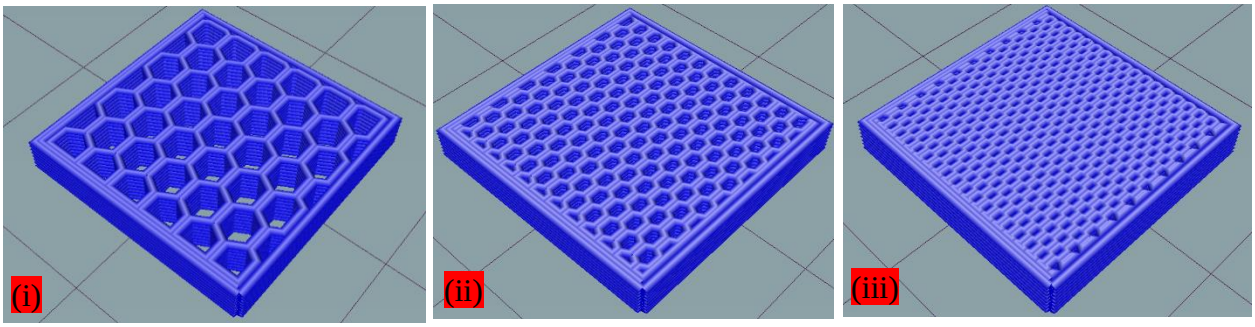

Figure 7: Sliced 3D models of compression sensors with (a) grid, (b) triangle and (c) honeycomb infill patterns at (i) 20%, (ii) 40% and (iii) 60% infill density with 260µm layer height and thickness

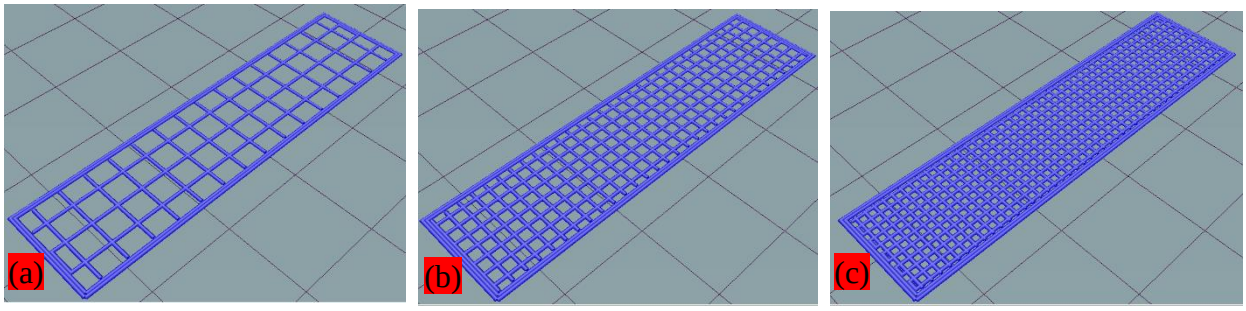

Figure 8: Sliced 3D models of tension samples with a grid infill pattern at (a) 20%, (b) 40% and (c) 60% infill density with 410µm layer height and thickness

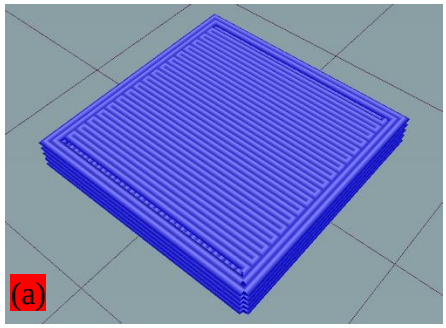

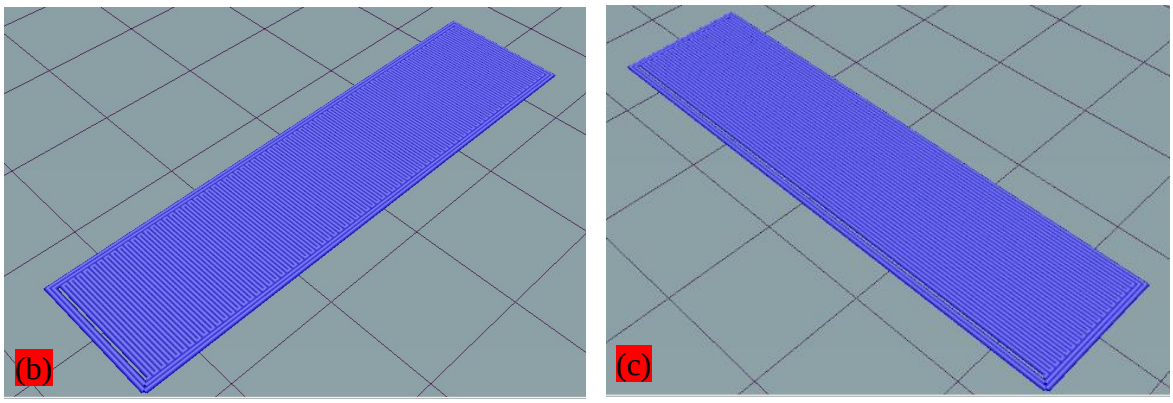

Figure 9: Sliced 3D models of tension sensors at 100% infill density with 410µm layer height and thickness

2.4.2 3D Printed Samples

The porous 3D printed samples, along with the bulk geometries, can be seen on Figures 10-13. The samples show excellent geometric accuracy as a result of the good rheological properties. The samples have very similar dimensions to the models generated using the slicing software. There are no overlaps seen since each layer stacks above the other in good alignment. Good adhesion between layers was also observed, with no gaps observed between layers. There was also no collapse of one layer into another that was observed. Each line printed can also be distinctly viewed. However, in some samples there are diagonal lines that are observed that cut through the infill patterns. These occur in between the printing of lines as a result of the nozzle moving to another location to begin printing. Due to the rheology of the ink, the nozzle drags material to its next location while the gcode is not executing a material extrusion at that particular time. Solving this issue is a difficult task that involves optimizing the print path. Such optimization results in the nozzle passing twice over certain sections of the infill, resulting in the occurrence of double extrusion and some lines in the infill being thicker than others. Few unwanted voids are formed within the porous samples as a result of the 3D printing process. During the 3D printing of

bulk samples, voids are usually a result of gaps between filamentary depositions. Extrusion and material deposition of polymer nanocomposite inks depends of a dragging phenomenon whereby as the print head moves along the print bed, material is extruded onto the print bed and adheres to it. This results in a continuous material flow from the syringe to the print bed that is dragged onto the surface because of the ink's rheological properties. Voids form when sudden turns of the print head result in small gaps being formed between subsequent lines. With the porous samples in this study, the sudden turns of the print head are minimized due to the relatively large size of the pores being created. Lines are extruded and generally stand on their own in each layer, and the reduced contact with other lines reduces the probability of voids being formed significantly. Voids are also present within the material while it is in the syringe. These are produced during material fabrication and loading into the syringe. These manifest on the 3D printed sample as a slight gap of air along a line caused by a split second of air being extruded while the print head continues to move. These are unlikely to be present in the porous samples since every time such a gap is created, then subsequent layers will fail to print since such a gap interrupts the dragging phenomenon. While this phenomenon is less noticeable in bulk material structures, it results in deformed porous structures with entire walls missing. All prints that exhibit this form of voids were aborted and restarted. Lastly, voids present in the syringe that are encased on all sides by material are still present when a line is extruded. However, these voids are microscopic in size and their effect on the mechanical properties of the material is very little. The analysis of the geometric accuracy relating to line thickness, layer height and pore size was performed, and the results are shown in detail in the next section.

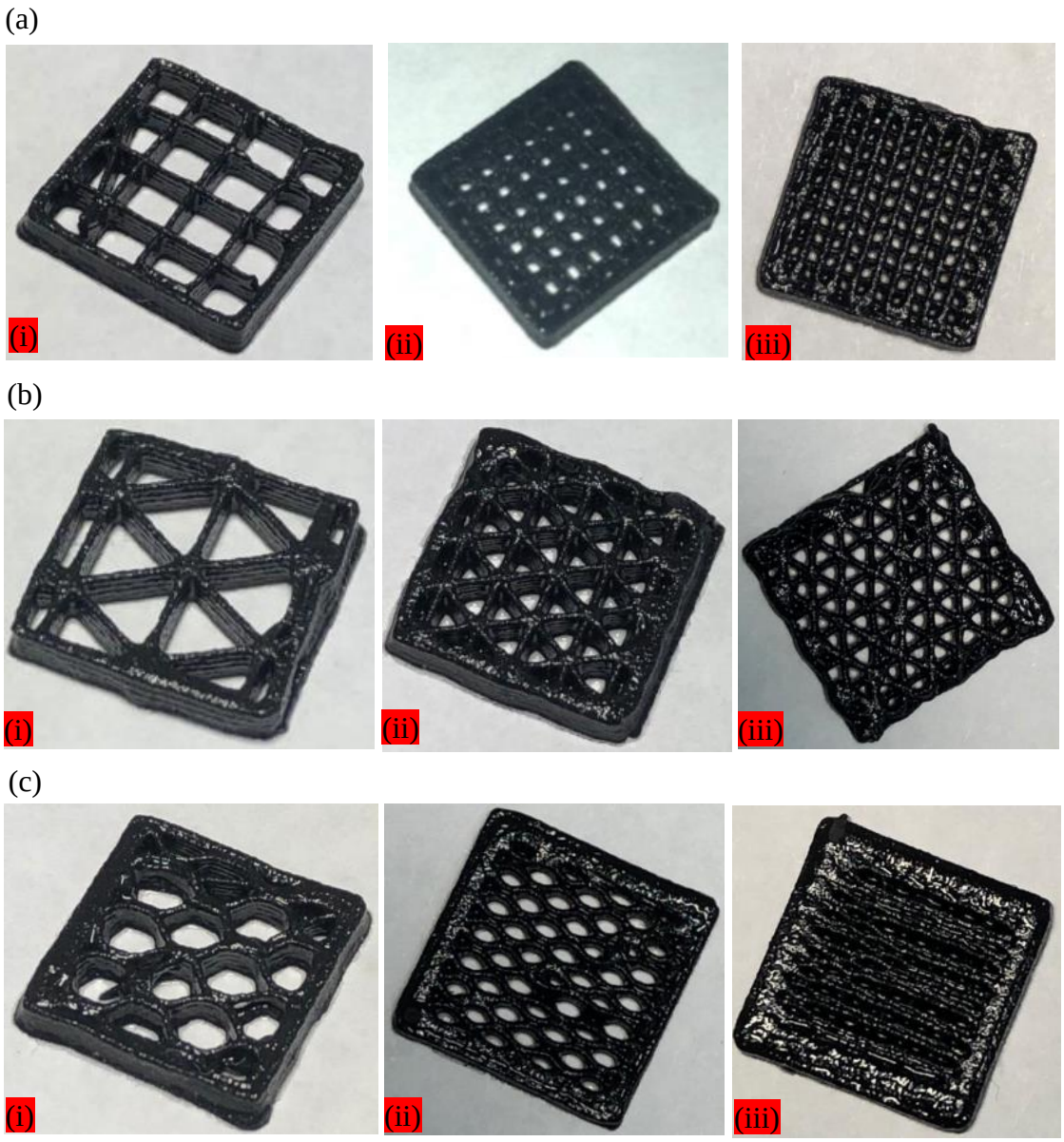

Figure 10: 3D printed compression sensors with (a) grid, (b) triangle and (c) honeycomb infill patterns at (i) 20%, (ii) 40% and (iii) 60% infill density with 410µm layer height and thickness

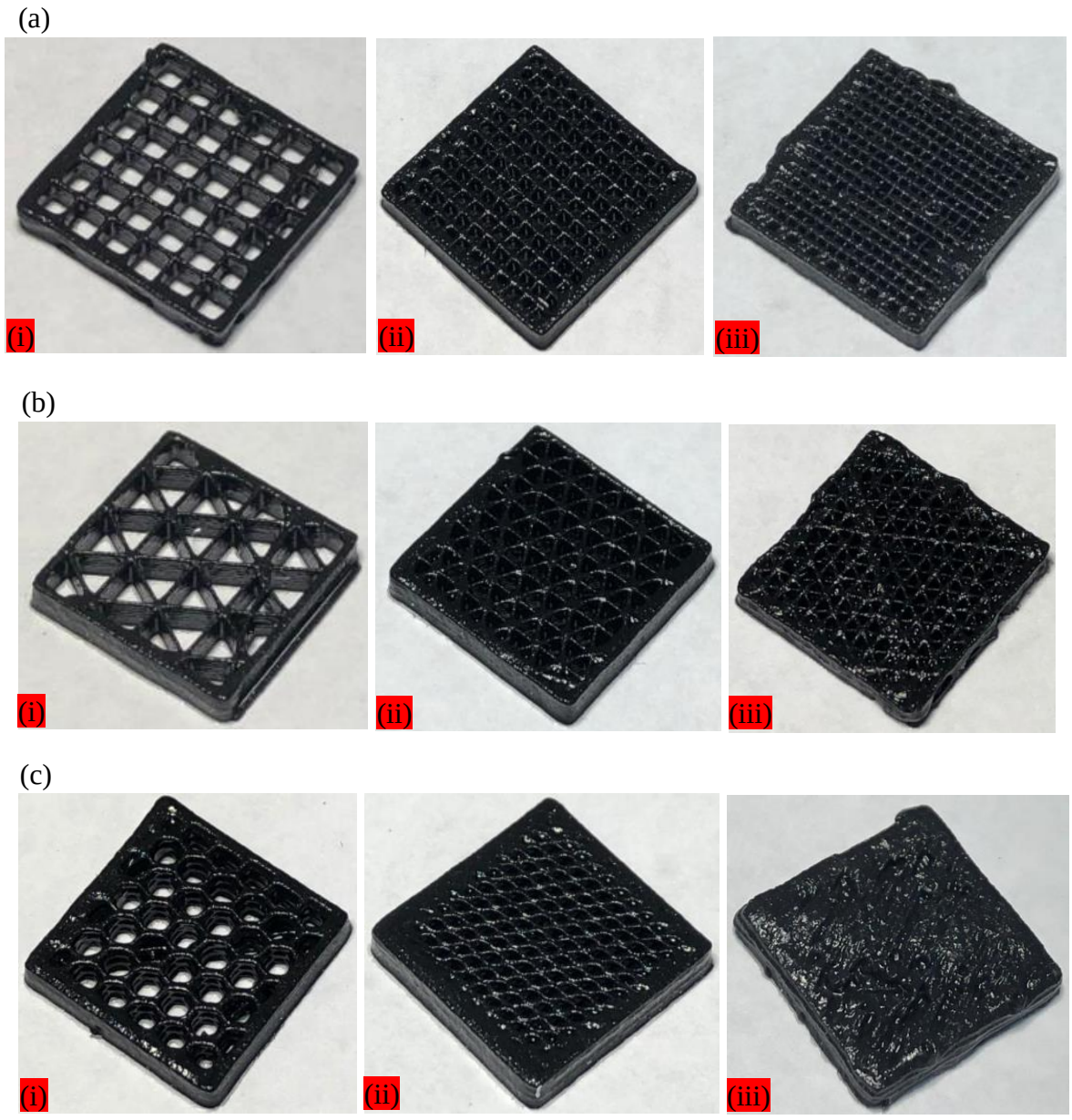

Figure 11: 3D printed compression sensors with (a) grid, (b) triangle and (c) honeycomb infill patterns at (i) 20%, (ii) 40% and (iii) 60% infill density with 260µm layer height and thickness

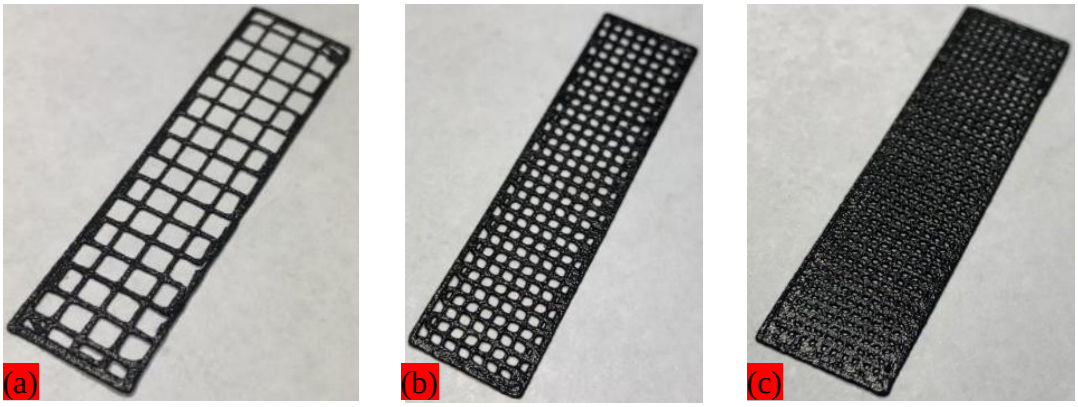

Figure 12: 3D printed tension samples with a grid infill pattern at (a) 20%, (b) 40% and (c) 60% infill density with 410µm layer height and thickness

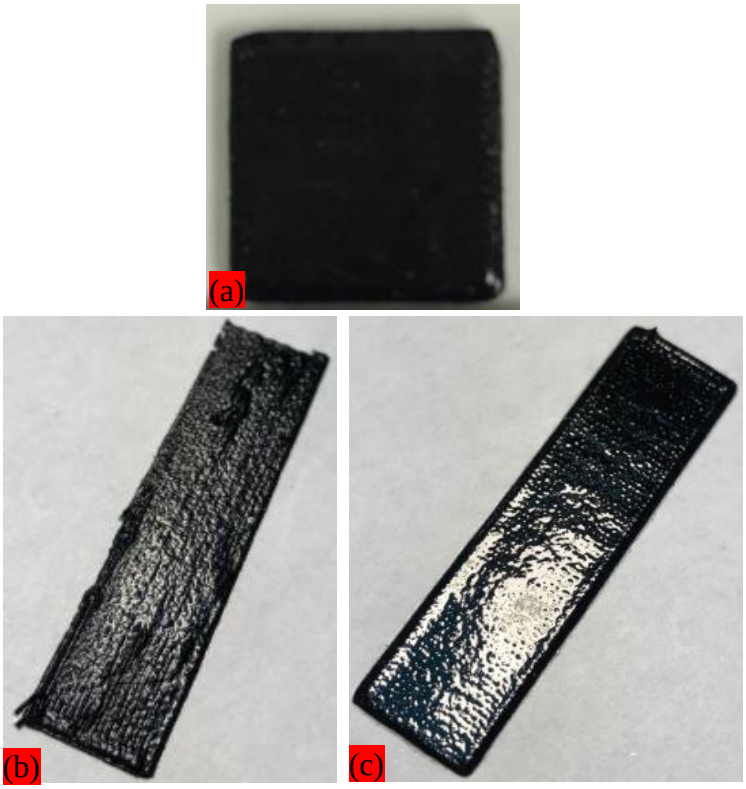

Figure 13: Sliced 3D models of tension samples at 100% infill density with 410µm layer height and thickness

2.5 SEM Characterization

2.5.1 Morphology, microstructure and CNT distribution

The morphology, microstructure and MWCNT distribution on the nanocomposite samples was characterized using a Field-Emission SEM (FE-SEM) at 5 kV. Four samples representing the compression and tension samples at 410 and 260 μm layer height and thickness were freeze-fractured using liquid nitrogen and a cutting blade in order to expose the side profile of the samples. The exposed surfaces were sputter-coated with a thin layer of gold palladium alloy to improve electrical conductivity and improve visibility at high magnification. Figures 14-16 shows the resulting FE-SEM images of the four samples at 200 X, 10 000 X and 23 X magnification (a-c). The images at 200 X magnification (a) highlight that the MWCNTS were well dispersed into the PDMS matrix. Dispersed CNTs are visible as a white haze on the images, a phenomenon which is uniform across each image. The thixotropic silica filler is observable as larger circular shapes that are a slightly lighter shade of gray compared to the dark gray polymer. The silica filler particles, both large and small, were dispersed uniformly, proving the effectiveness of using shear mixing to disperse nanomaterials within a PDMS matrix. The images at higher magnification (2500 X and 10 000 X) show the CNTs in contact with each other, forming conductive networks (b). There are gaps between a few adjacent CNTs observed on the images which could be reduced by the compression of the samples, thus creating more conductive networks and verifying the piezoresistive effect. The FE-SEM images at the lowest magnification achieved (23 X) show macroscale side profiles of the four samples tested. All samples show good layer bonding, and the walls are shown to hold their shape well due to the high yield stress point of the nanocomposite ink. There is some spreading that can be observed with the first layer of the 5 layer 410 μm compression sample which is a result of carrying the load of the other four layers. The cross section

is larger near the base of the sample, narrowing with each subsequent layer. The layer height is also affected, with the first layer having the shortest layer height and the top layer having the largest since it does not support any weight above it. However, the layer heights remain geometrically accurate, with the bottom layer showing the largest deviation from the model height. The 8 layer 260 µm compression sample showed similar behavior to the 410 µm sample. However, its layers showed more adhesion and better surface finish. The one-layer samples highlight the high yield stress point of the material. The cross-section lines are almost circular, showing that they held shape after being extruded out of the nozzle.

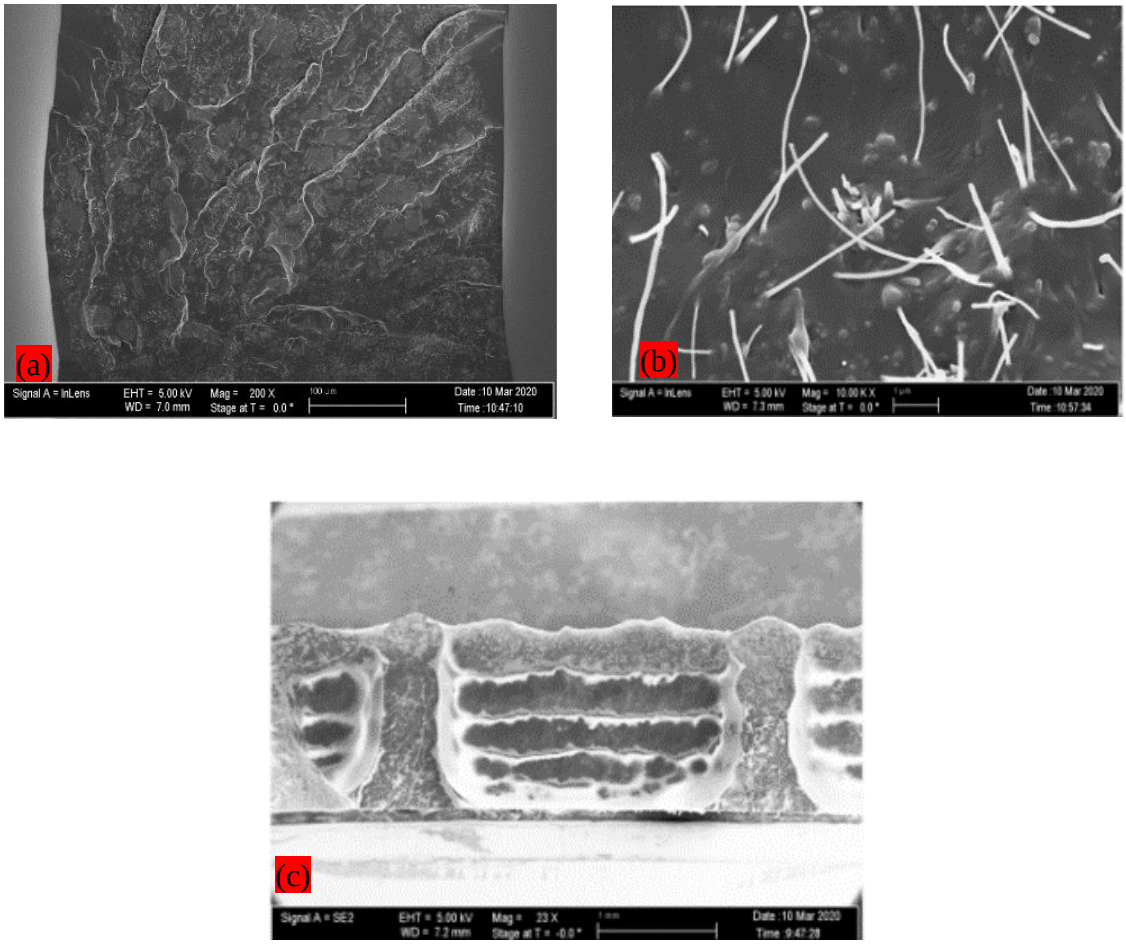

Figure 14: FE-SEM images of the side profile of 410 µm compression porous sample at (a) 200 X, (b) 10 000 X and (c) 23 X magnification

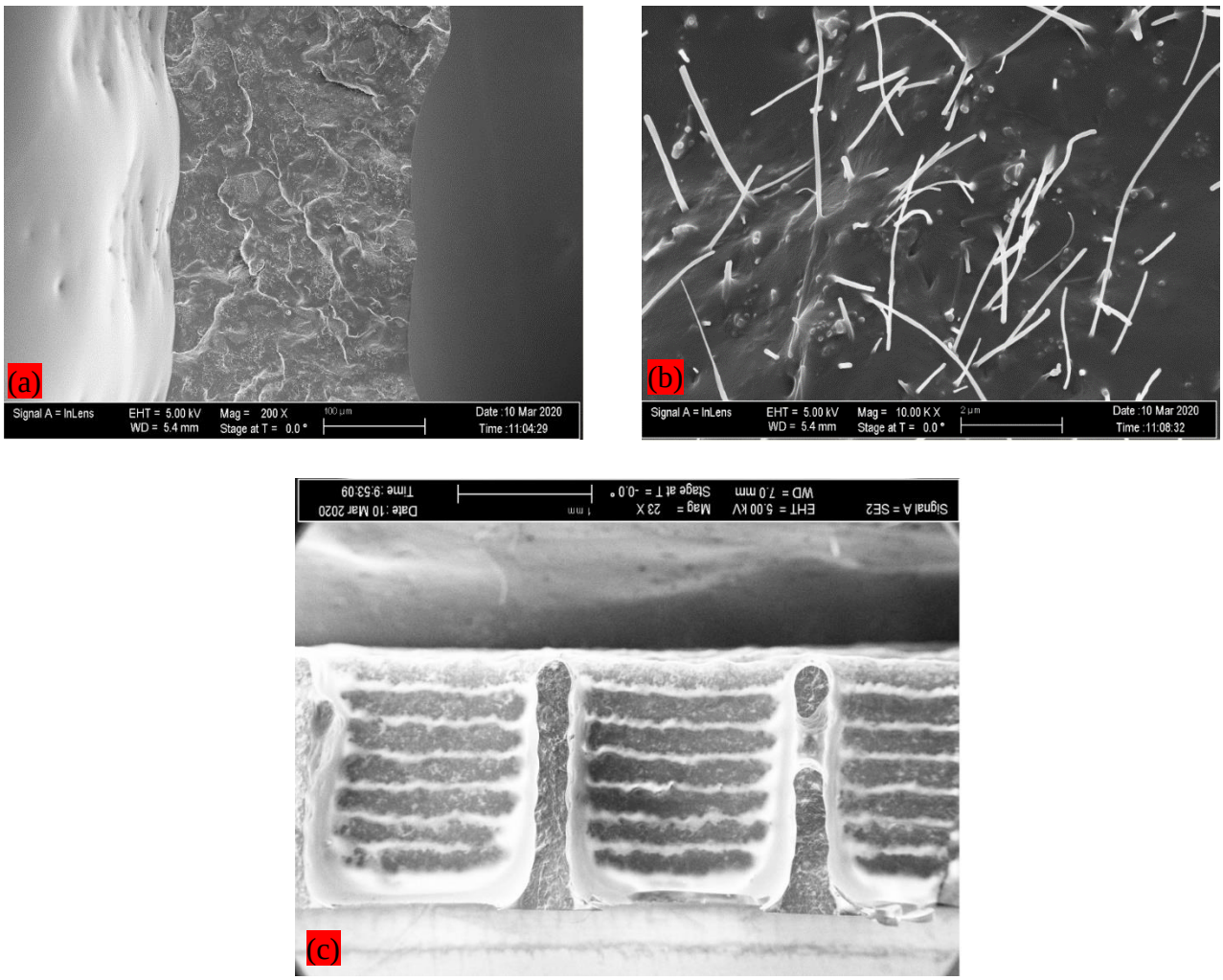

Figure 15: FE-SEM images of the side profile of 260 µm compression porous sample at (a) 200 X, (b) 10 000 X and (c) 23 X magnification

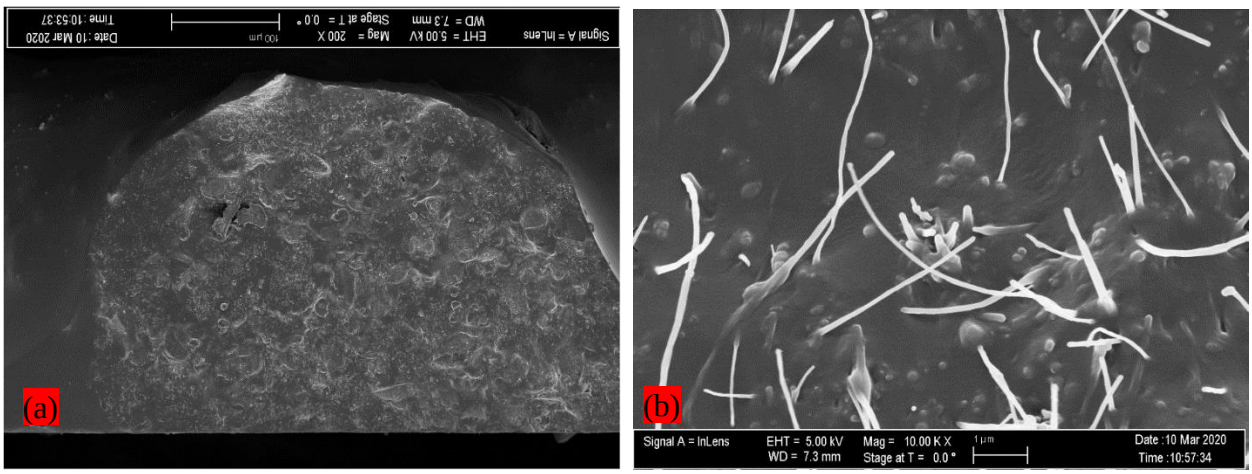

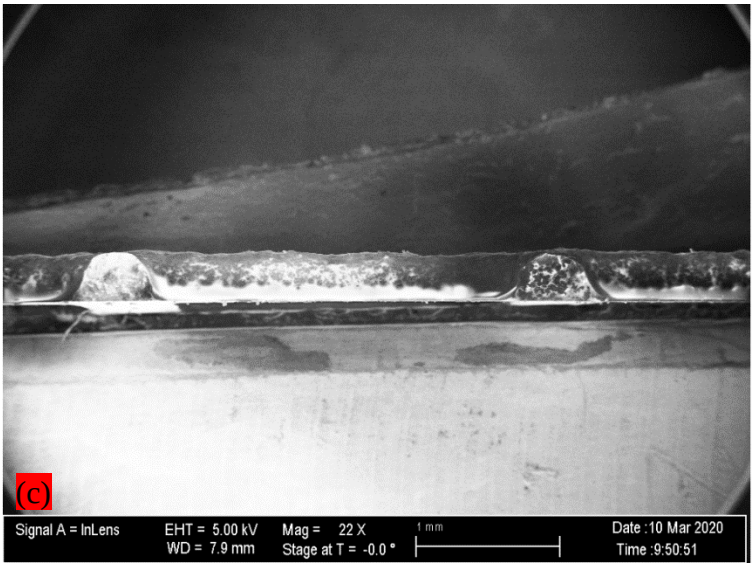

Figure 16: FE-SEM images of the side profile of 410 µm tension porous sample at (a) 200 X, (b) 10 000 X and (c) 23 X magnification

2.5.2 Porosity Characterization

The pores of both the compression sensors and tensile test samples were characterized using the image processing software ImageJ. The controlled porous structure fabricated as a result of infill 3D printing. The infill is essentially a repetitive structure used to occupy space within a 3D printed shell. Since 3D printing offers the distinct advantage of formulating complex geometries, it is often used to reduce material used and the weight of the final product by introducing various infill densities and internal lattice structures. Through the use of infill patterning, the pores created within the samples in this study were enabled to be regular and tunable. Figures 17-19 show the tunability of the pore structure and density using SEM images at similar low magnification. As seen on the images, the pores are well formed and geometrically accurate compared to the sliced 3D models (Figures 6-8). The grid, triangle and honeycomb infill patterns (a-c) are distinct, with little unwanted crossover between lines. The 20% infill density samples (a) show the best geometric accuracy due to the reduced effect of dragging whereby the

nozzle applies a shear force on already deposited lines as it prints a new line, causing the existing lines to be pulled along the nozzle's printing path. This phenomenon is seen within the 40 and 60% samples ((ii) and (iii)). For example, in Figure 17(a)(ii), the pores that are supposed to be square shaped have a slight tilt, the pores taking the resemblance of a parallelogram shape. This is caused by the dragging of the horizontal lines as the nozzle prints vertically. However, this issue is very slight, only clearly visible in the microscale using SEM imaging.

The pores of honeycomb structure with 60% infill density at 410 µm layer thickness appear to be elliptical, however the macroscopic image of the sample depicts a honeycomb structure. This irregularity could be explained by the fact that the SEM image does not provide a more detailed outline of the pores. The path of the deposited lines on the top layer could provide more context of the pore shape. A distinction between the 410 and the 260 µm layer thickness sample can be clearly observed. The pores of the 260 µm samples at each infill pattern and density are smaller than those of the 410 µm structures. The pores appear to be more numerous, with visibly thinner lines compared to the 410 µm structures. The porous tension samples 3D printed with a 410 µm nozzle are shown in Figure 20. These are very similar to the 410 µm grid pattern compression samples in shape and size.

The pores were quantitatively analyzed using the image processing software ImageJ in order to compare the 3D printed samples to the models created by slicing software that is translated to gcode. An analysis was performed to quantify the infill density, thickness of the lines within the infill, and the area of the joints where lines intersect. Figure 21 shows the methodology used to quantify these factors. To begin the analysis, a scale was set using a known length within the image. A scale is provided on the SEM images toward the bottom left corner. In all three SEM images provided, a length of 2 mm was provided as the scale.

(a)

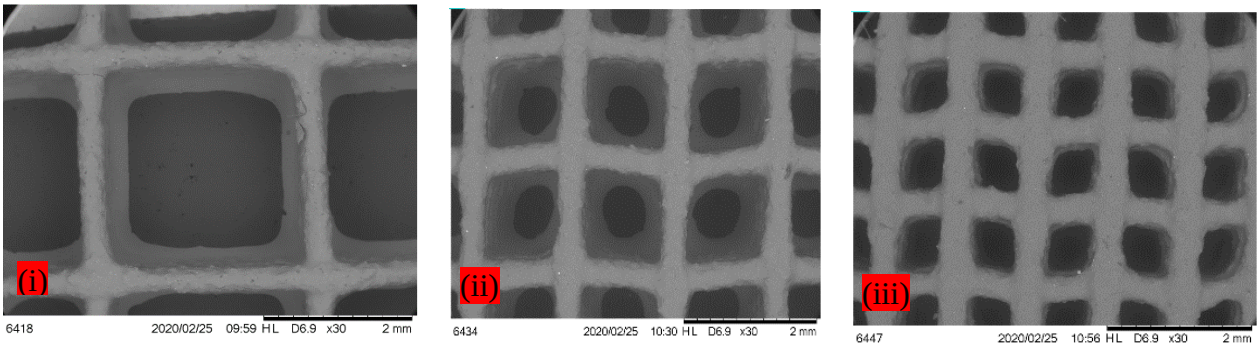

(b)

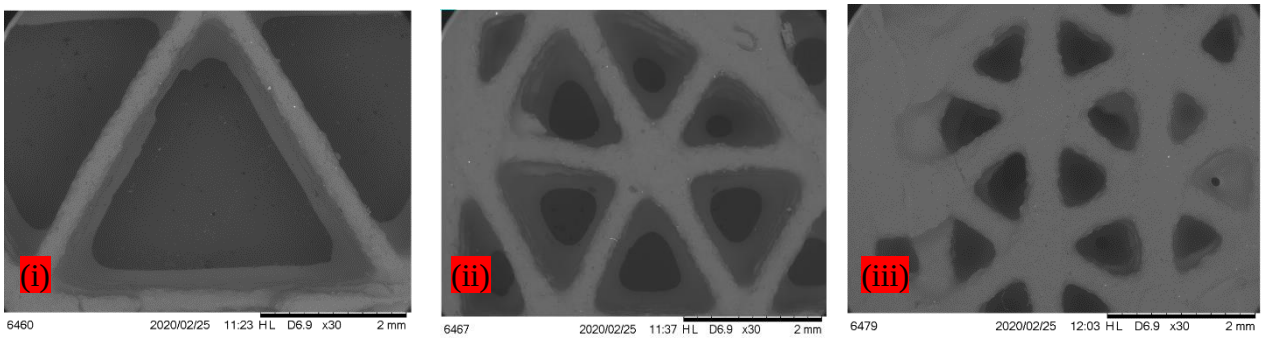

(c)

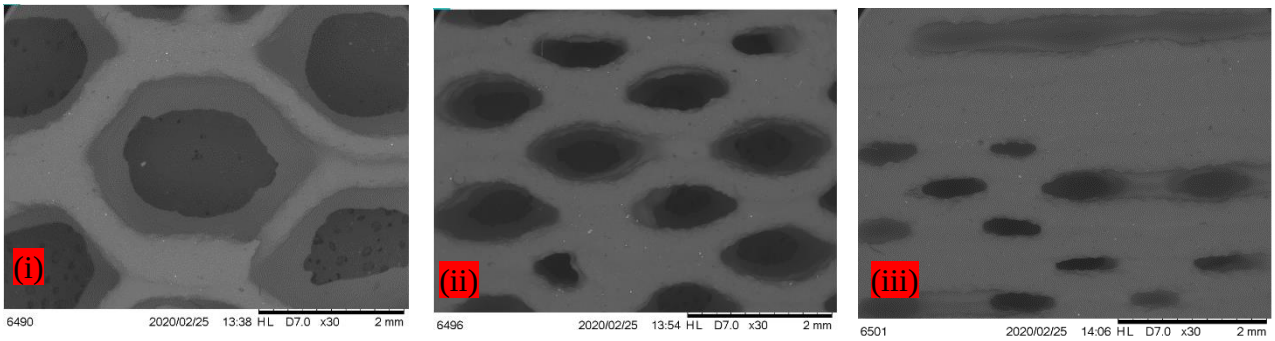

Figure 17: Low magnification SEM images of compression sensors with (a) grid, (b) triangle and (c) honeycomb infill patterns at (i) 20%, (ii) 40% and (iii) 60% infill density with 410µm layer height and thickness

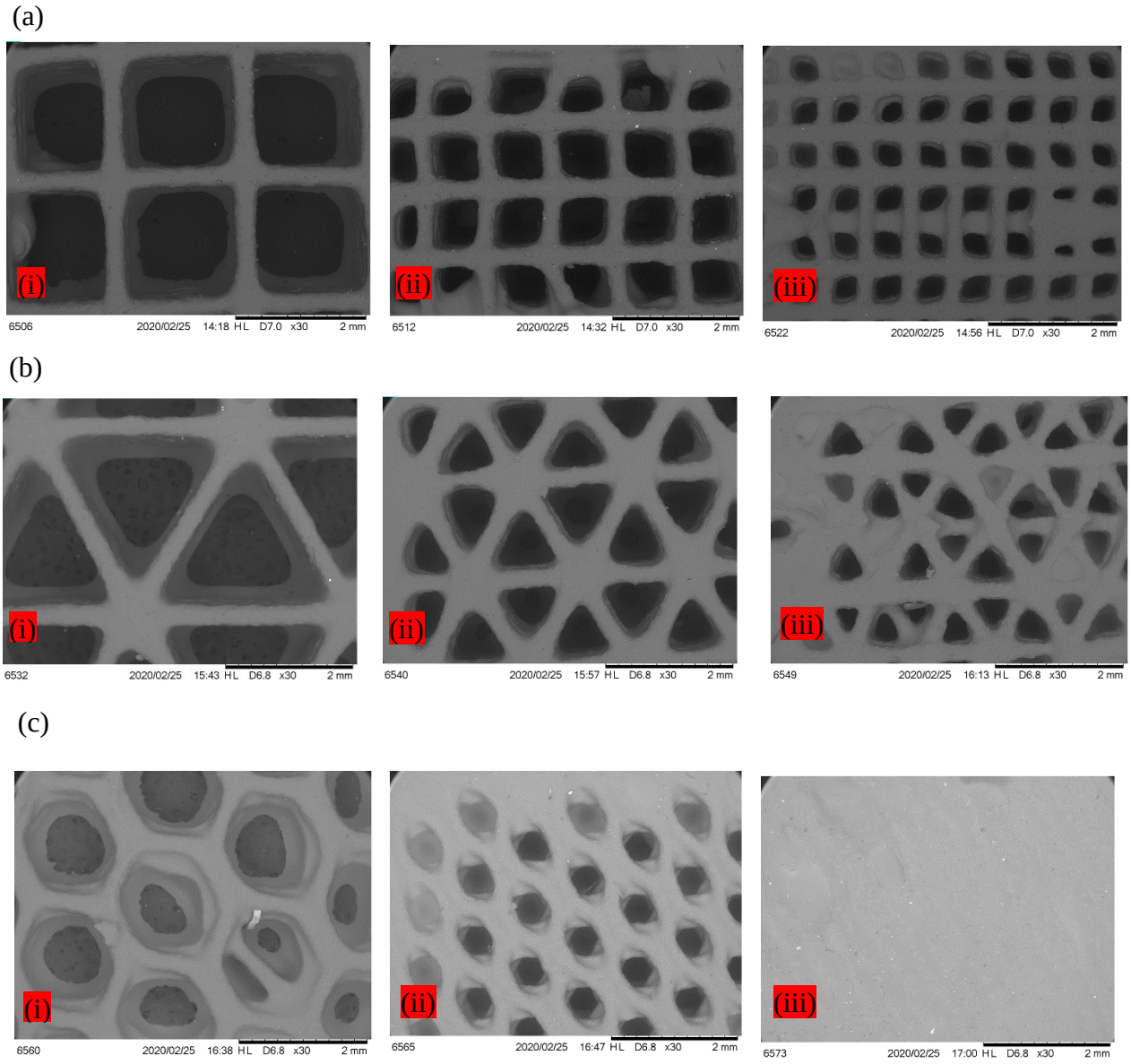

Figure 18: Low magnification SEM images of compression sensors with (a) grid, (b) triangle and (c) honeycomb infill patterns at (i) 20%, (ii) 40% and (iii) 60% infill density with 260µm layer height and thickness

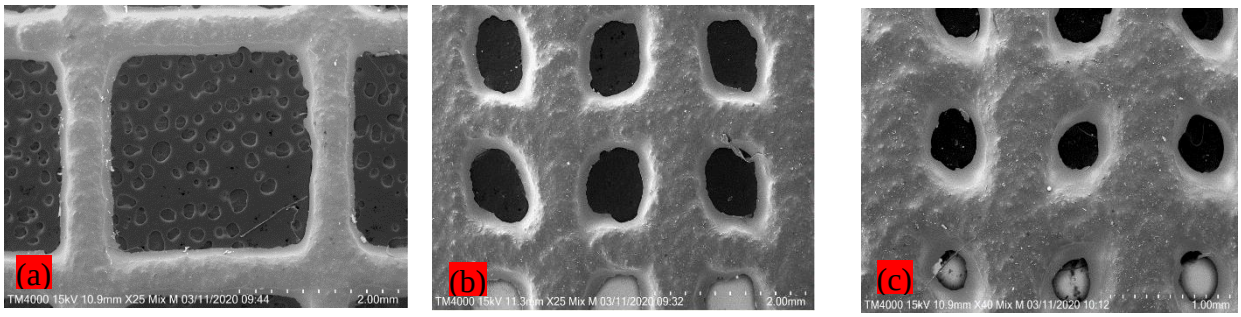

Figure 19: SEM images of tension samples with a grid infill pattern at (a) 20%, (b) 40% and (c) 60% infill density with 410 µm layer height and thickness

On the model images, a known dimension depicting the sample length was used to set the scale. The model images were deemed to be proportional and to scale after analyzing the gcode. Each unit of travel on the print axes represents a millimeter. This information was used to verify a known distance by locating the lines of gcode that depicted the location of the predetermined points and using them to calculate the distance between the points. All checks done verifying known distances were found to be accurate. The infill area was calculated by subtracting the pore area, depicted as the inner area highlighted in a red marker on the images, from the "phantom" solid which would be the area taken up by the material if a pore was not present, in this case shown as the outer area also highlighted in red. Thus the infill fraction can be depicted using the equation

$$Infill\ density = \frac{A_{phantom} - A_{pore}}{A_{phantom}} \quad (3)$$

whereby $A_{phantom}$ is the area of the "phantom" solid and A_{pore} is the pore area. The infill fraction, also known as the infill density, is a value between 0 and 1 which depicts the amount of infill material relative to the bulk version of the same geometry. It also be represented as the infill percentage F. The porosity can be calculated using the equation

$$Porosity = 100 - F \quad (4)$$

whereby the porosity represents the pore area relative to the bulk shape. The line thickness of each line enclosing a pore was measured the ImageJ software. Three measurements were taken of each of the four lines enclosing a grid pore, three lines enclosing a triangle pore and six lines enclosing a honeycomb pore, and an average was calculated. The joint area was measured as shown by the yellow outlines on Figure 20.

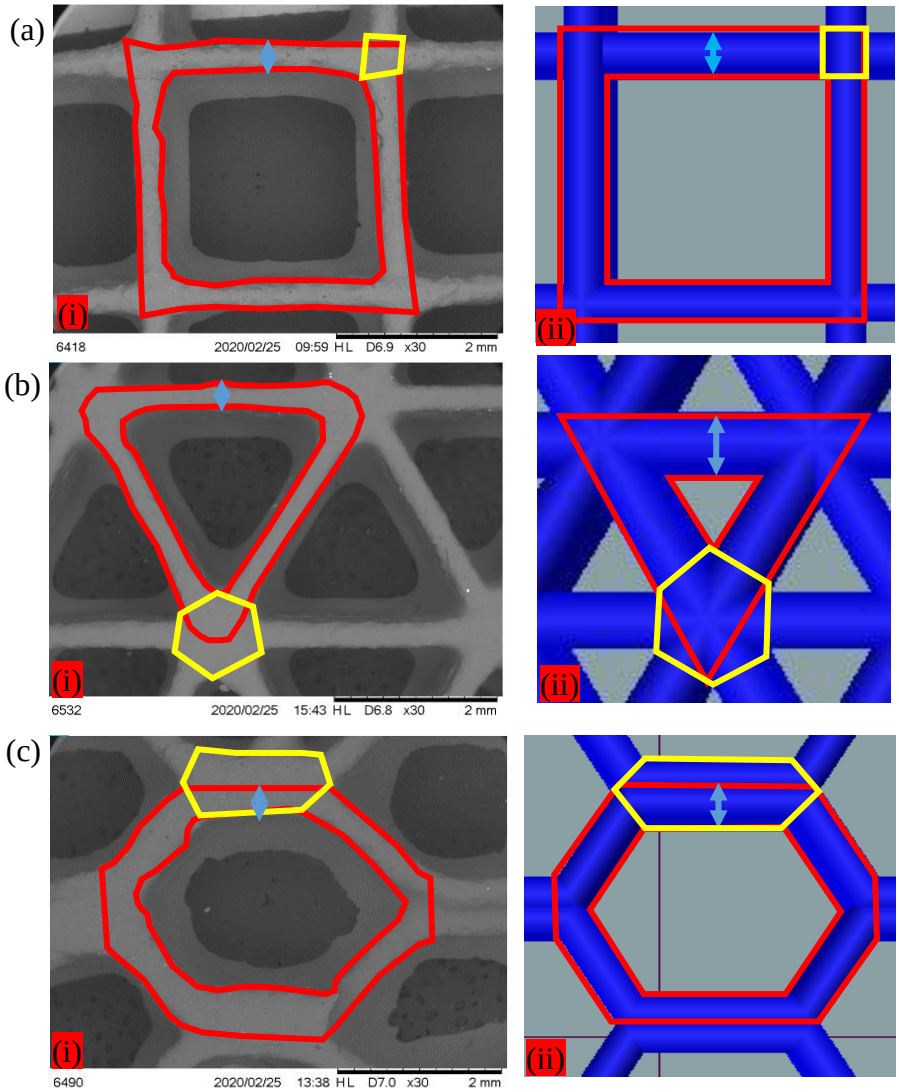

Figure 20: Quantitative pore characterization highlighting infill area (red), line thickness (blue) and joint area (yellow) for (a) grid, (b) triangle and (c) honeycomb infill pattern (i) experimental and (ii) model samples

Figures 21-23 shows the results of the quantitative pore characterization of the pores. An interesting observation can be made concerning the infill fraction values. Looking at the grid infill pattern samples with 410 µm layer thickness, the experimental infill percentages were found to be 37.7%, 65.7% and 80.3% for the 20%, 40% and 60% infill samples respectively. This is a very large deviation from the values stated by the slicing software. When the sliced model pores are analyzed, the infill percentage values are found to be 39.7%, 63.0% and 79.1% for the 20%, 40% and 60% infill samples respectively. The model infill percentages are much closer to the experimental values. This behavior can also be seen with the triangle and honeycomb infill pattern samples. It therefore can be said that each infill percentage as annotated by the slicing software differs from the gcode model produced and from the 3D printed product by about 20%. This discrepancy could be as a result of the slicing software used, which seems to prioritize the stability of the infill and the optimization of printing paths above the accuracy of the infill percentage. Using the current software, it is possible to use an iterative method to locate the infill percentage annotated by the slicing software which results in the desired model and experimental value, with the approximate 20% difference being used as a starting point. For simplicity and consistency, the 20%, 40% and 60% infill labels will be used to identify the three different porous samples.

Using the infill percentage values, the porosities were calculated to be 62.3%, 34.3% and 19.7% for the 20%, 40% and 60% infill samples respectively. As seen on Figure 21, the infill percentage values at each infill density were similar at different infill patterns. For example, the 60% infill samples with the grid and triangle patterns were comparable. The 60% infill honeycomb samples had a slightly larger infill percentage, showing the highest amount of infill of all the 410 µm layer samples. The highest porosity was achieved with the 20% infill triangle sample with values of 66.0% and 62.1% for the experimental and theoretical samples respectively. The 260 µm

layer samples behave in a similar manner to the 410 µm samples, however they achieved higher infill percentages at each corresponding infill density. For example, the 20% infill grid sample with 260 µm layer thickness has an infill percentage of 48.0% compared to the 37.7% value of the 410 µm layer sample at the same infill pattern and density. The highest porosity by the 260 µm layer samples was achieved by the 20% infill honeycomb sample with an experimental value of 55.1%. The 260 µm layer samples also showed a larger discrepancy between the experimental and theoretical infill percentages. The 60% infill honeycomb sample showed an infill percentage of 100% and essentially behaved like a bulk material. This is consistent with the sliced model generated, as shown in Figure 24. The sliced model does not have any open pores due to the proximity of the lines to each other.

The 260 µm layer slice program attempts to create more pores that are smaller compared to the 410 µm layer program. It therefore reaches the threshold at which the spacing between adjacent lines is too small to create pores at a lower annotated infill density than the 410 µm layer program. The grid pattern tension samples with a 410 µm layer thickness had infill percentages that are similar to the grid pattern compression samples of the same layer thickness, affirming the fact that these sample types have the same pore design. The line thickness characterization of the porous 3D printed samples is shown in Figure 23. The line thickness as determined in the slicing software is shown as a red line on the bar graphs. The experimental line thicknesses at all infill patterns are consistent with the theoretical results, with a few discrepancies. The joint area characterization results are shown on Figure 24. The joint area is seen to vary according to the infill pattern type. For both the 410 and 260 µm layer thicknesses, the grid pattern has the smallest joint area by a significant margin. The triangle and honeycomb patterns, while showing significant individual variations, are largely within the same scale. This is because the grid pattern consists of

two lines intersecting perpendicular to each other, while the triangle pattern has three lines that intersect to form a star joint and the honeycomb pattern has two lines that are parallel to each other and come into contact at the edge of the hexagonal shape. The 260 µm layer thickness samples on average have smaller joint areas compared to 410 µm layer samples of the same infill pattern and density. The tension grid pattern samples have values that are very similar to the compression grid samples, further highlighting the similarity in the pore structure.

(a)

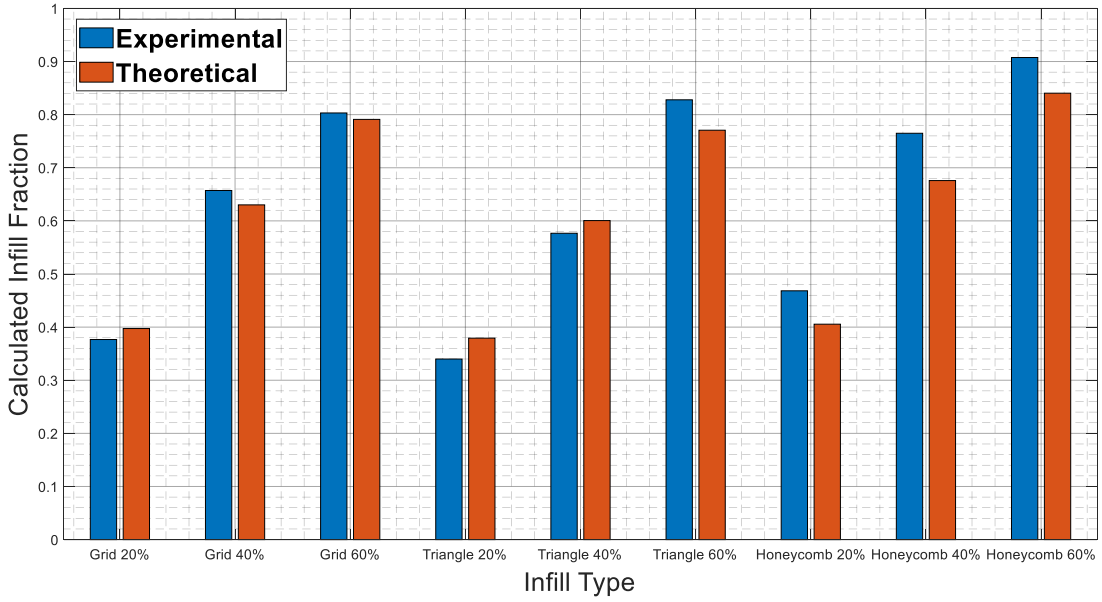

(b)

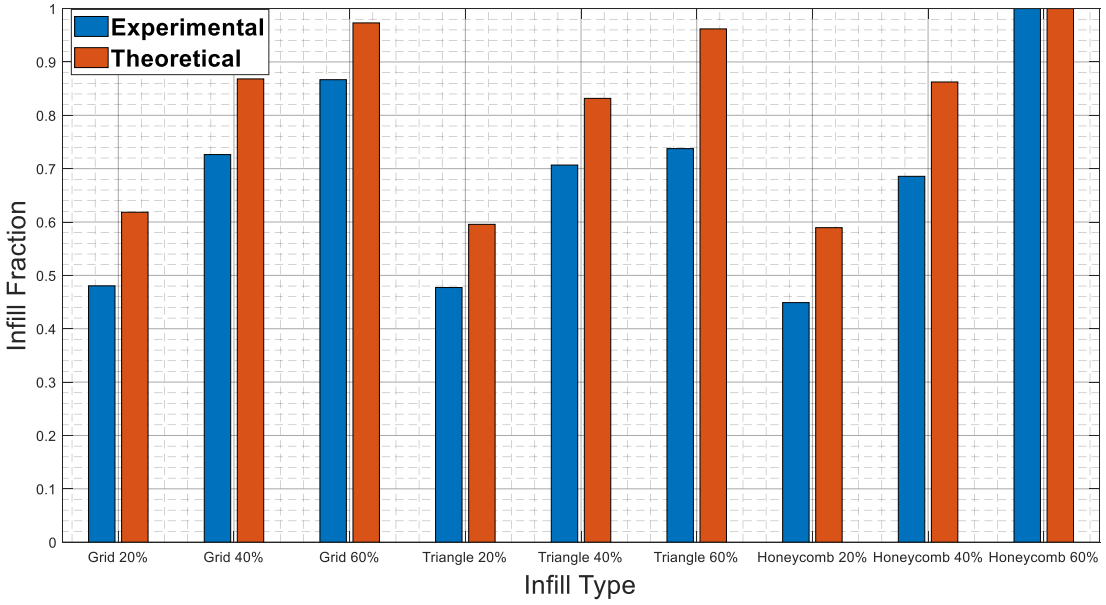

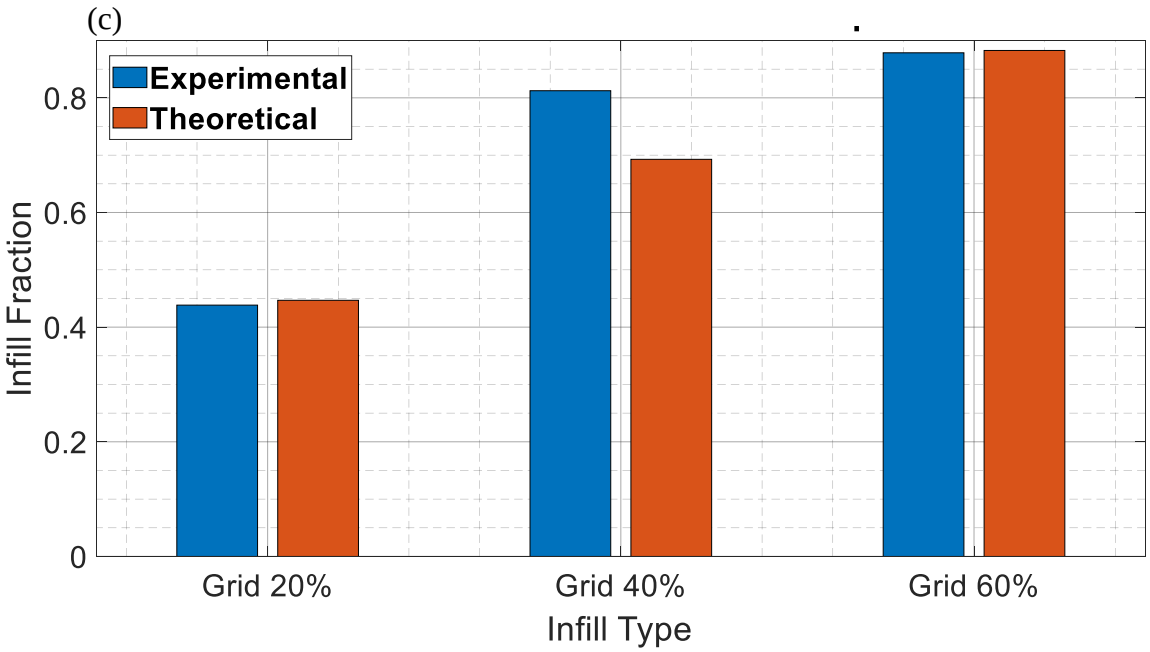

Figure 21: Infill fractions of (a) 410 µm and (b) 260 µm compression sensors, as well as (c) 410 µm tension samples with grid infill pattern

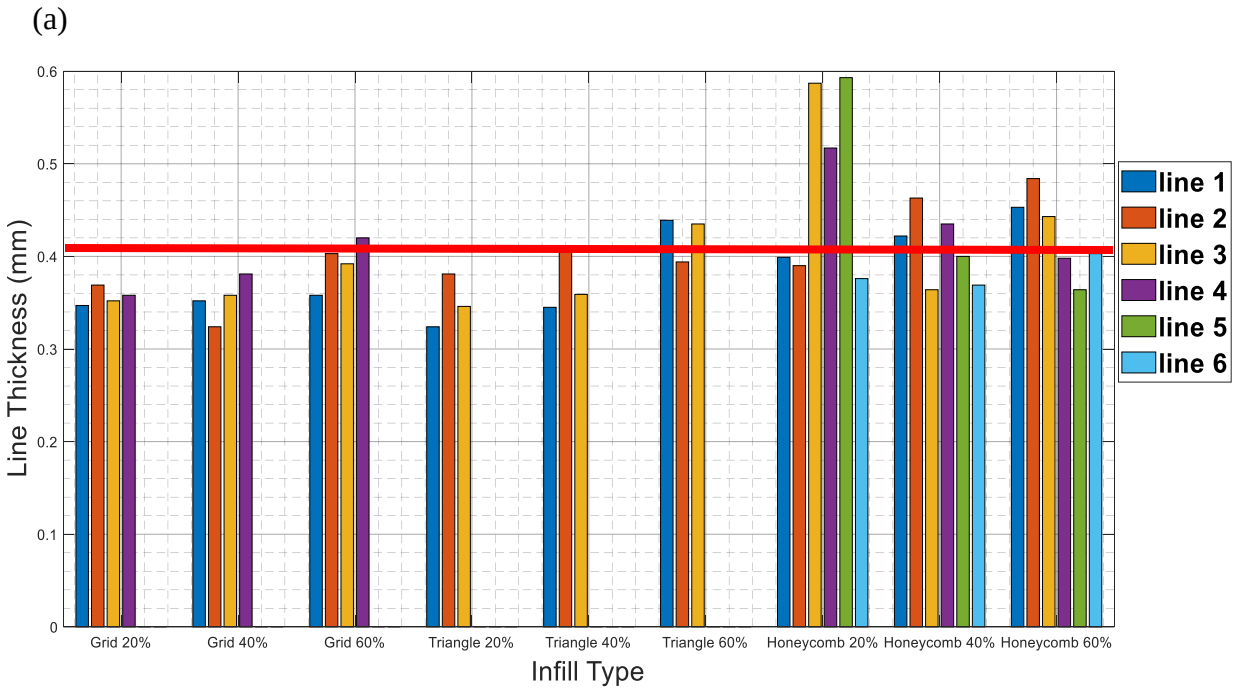

(b)

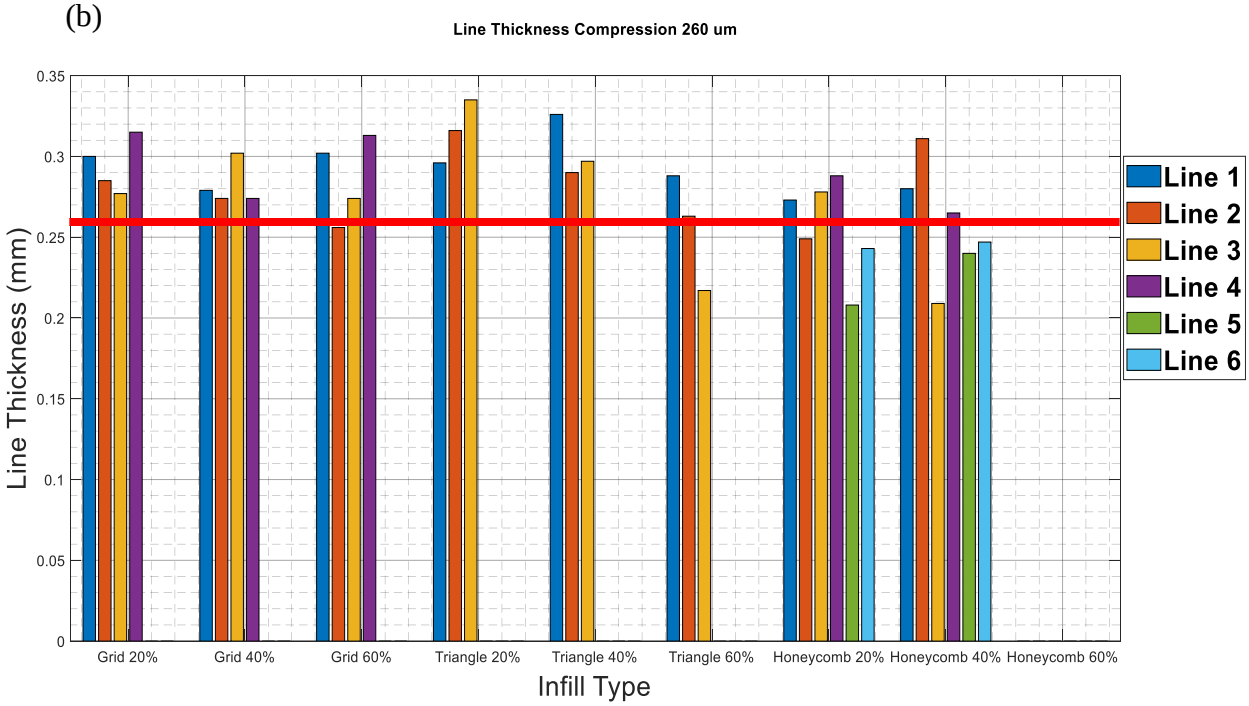

(c)

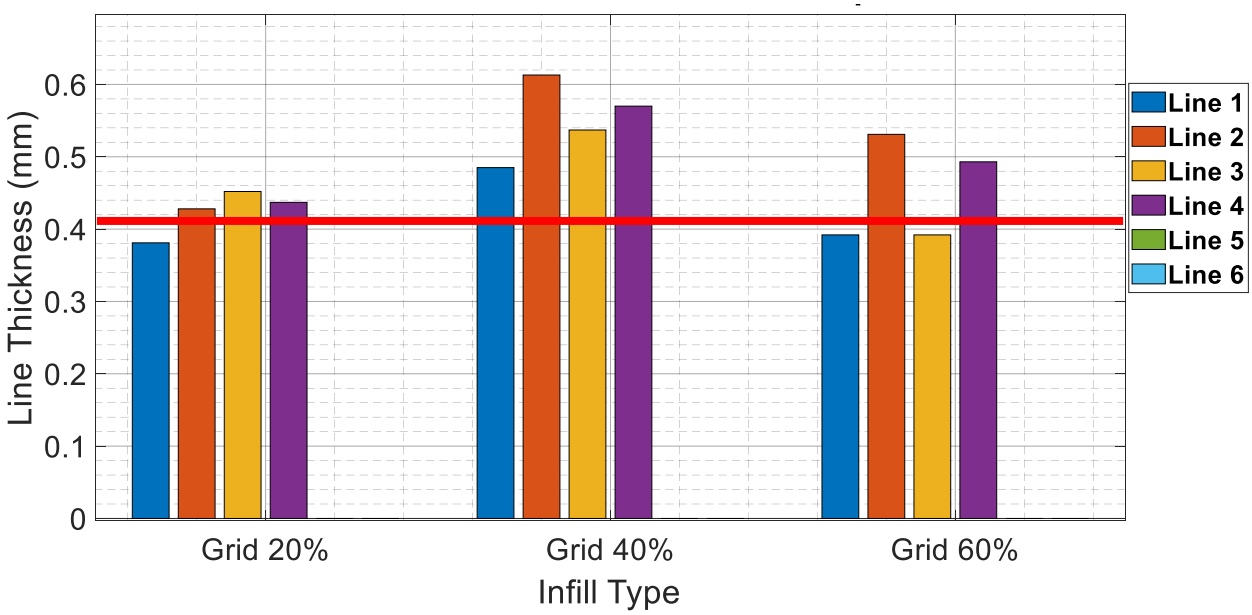

Figure 22: Line thicknesses of (a) 410 µm and (b) 260 µm compression sensors, as well as (c) 410 µm tension samples with grid infill pattern

(a)

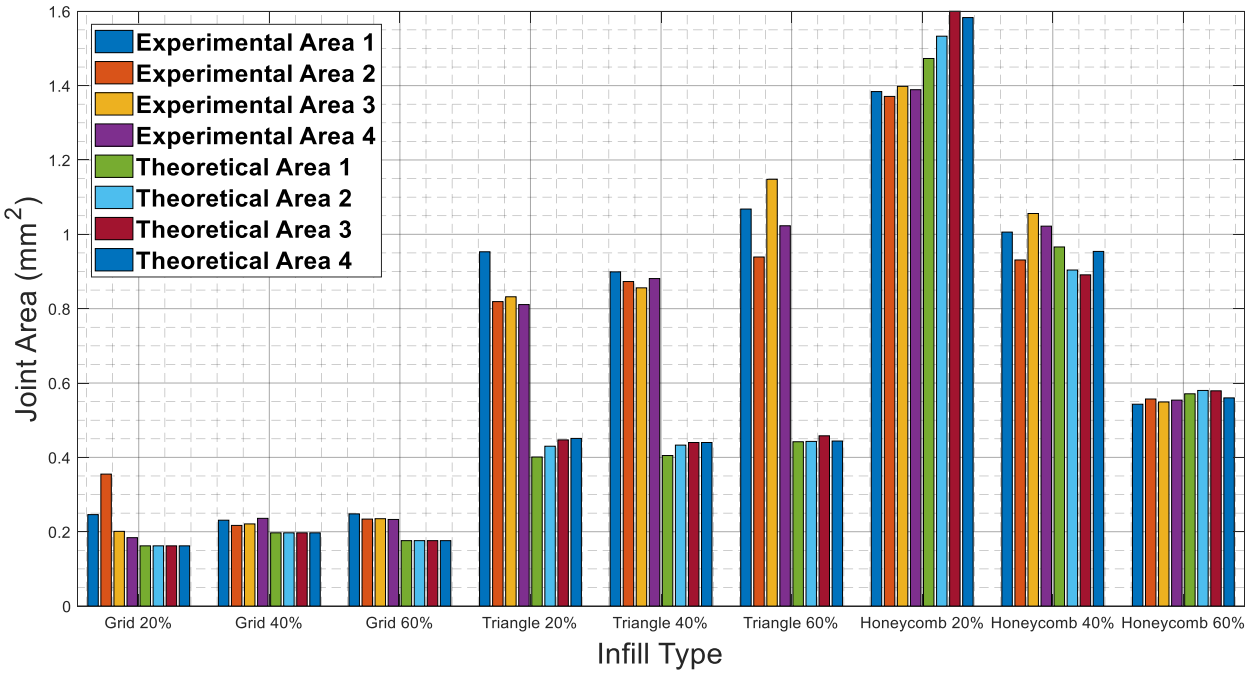
Experimental Area 1
Experimental Area 2
Experimental Area 3
Experimental Area 4
Theoretical Area 1
Theoretical Area 2
Theoretical Area 3
Theoretical Area 4
Joint Area (mm^2)
0
0.2
0.4
0.6
0.8
1
1.2
1.4
1.6
Grid 20%
Grid 40%
Grid 60%
Triangle 20%
Triangle 40%
Triangle 60%
Honeycomb 20%
Honeycomb 40%
Honeycomb 60%
Infill Type

(b)

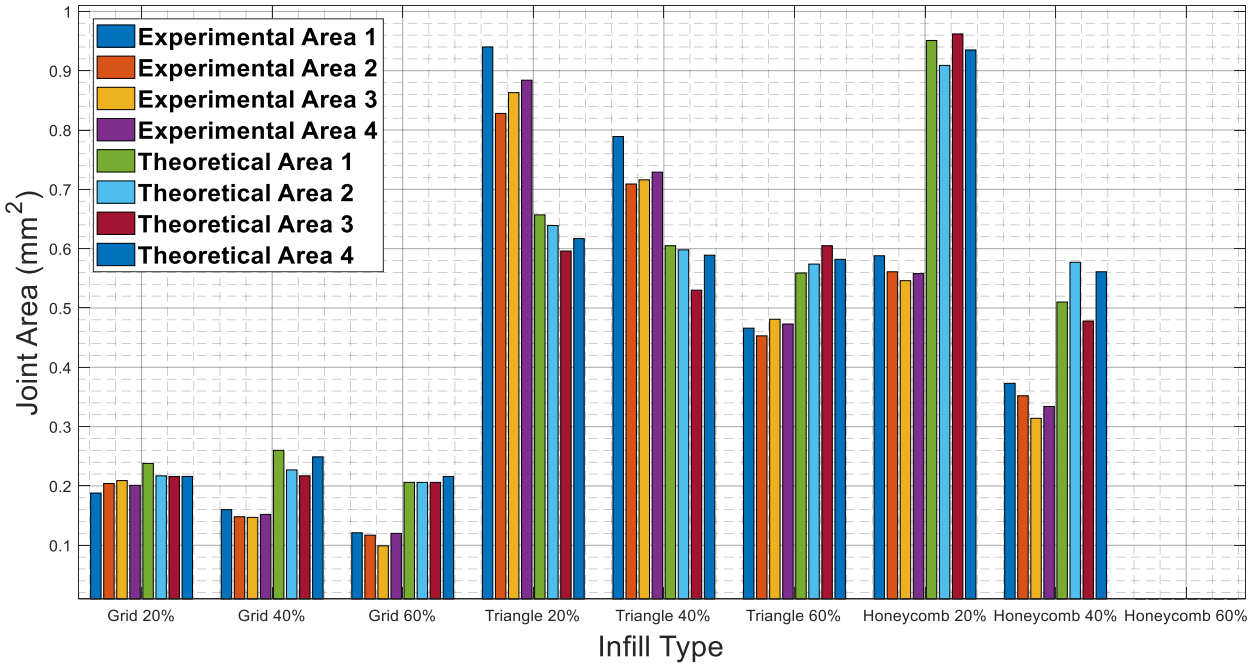
Experimental Area 1
Experimental Area 2
Experimental Area 3
Experimental Area 4
Theoretical Area 1
Theoretical Area 2
Theoretical Area 3
Theoretical Area 4
Joint Area (mm^2)
0.1
0.2
0.3
0.4
0.5
0.6
0.7
0.8
0.9
1
Grid 20%
Grid 40%
Grid 60%
Triangle 20%
Triangle 40%
Triangle 60%
Honeycomb 20%
Honeycomb 40%
Honeycomb 60%
Infill Type

(c)

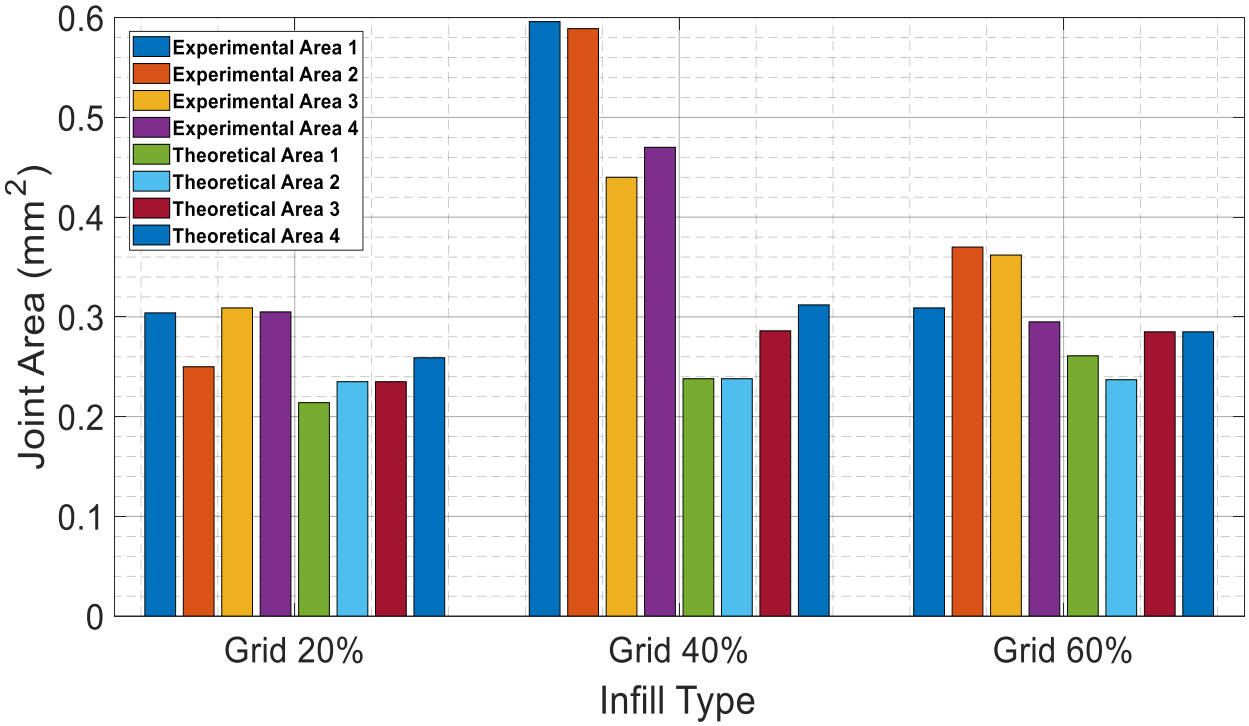

Figure 23: Joint areas of (a) 410 µm and (b) 260 µm compression sensors, as well as (c) 410 µm tension samples with grid infill pattern

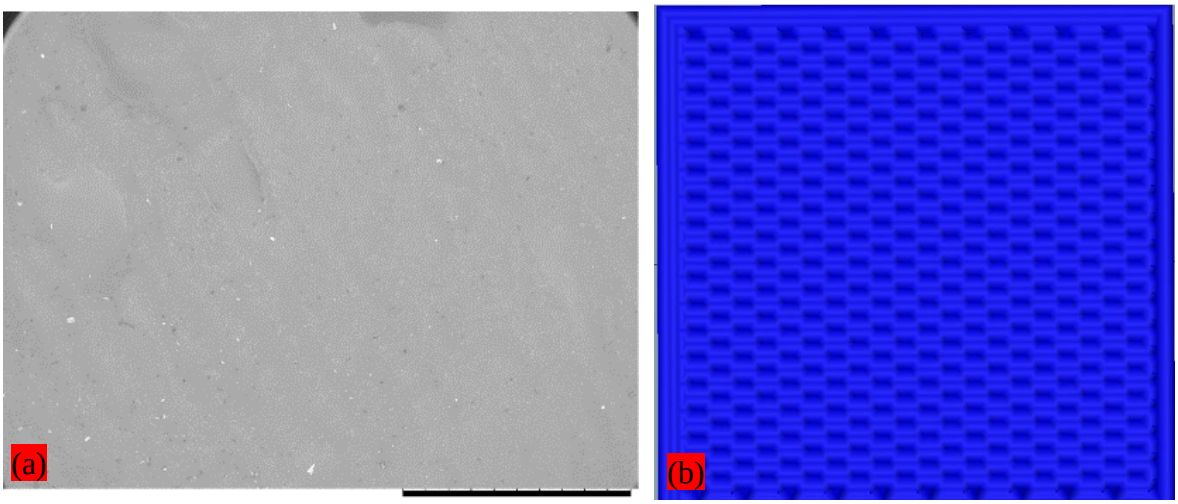

Figure 24: Infill fraction characterization of (a) experimental and (b) model samples with honeycomb infill pattern at 60% infill density and 260 µm layer thickness

2.6 Conclusion

This chapter focused on the formulation of a PDMS/CNT nanocomposite ink, as well as the 3D printing process and characterization of the porous compression sensors and tension samples. Ink formulations with varying rheological properties were considered, and an optimum ink with 15 wt% thixotropic silica filler was selected as the material of choice. Porous samples were 3D printed with grid, triangle and honeycomb infill patterns, with infill densities of 20%, 40%, 60% and 100%. Two nozzle sizes, 410 and 260 μm, were used to fabricate the samples. The 3D printing process was discussed in detail, with a comparison made between the model produced using slicing software and the 3D printed product. The 3D printed samples were found to be geometrically accurate with slight discrepancies attributed to gravity and the dragging phenomenon. The printed geometries were characterized using SEM in order to characterize the morphology, microstructure and CNT distribution. SEM imaging showed that uniform dispersion was achieved with both the CNTs and the silica filler. Finally, the samples' porosity was characterized using a combination of SEM and the image processing software ImageJ. The infill percentage, line thickness and joint area of the samples was discussed in great detail. The annotation of the infill density was found to be offset by approximately 20% for all values considered.

Chapter 3. Characterization of Piezoresistive Sensing

3.1 Introduction

This chapter highlights the characterization of the electrical properties of the CNT/PDMS nanocomposite sensors. Specifically, an investigation of the effect of the 3D printed porous structure on the piezoresistive sensing response is performed. Therefore, this section looks to prove the effectiveness of introducing porosity to these sensors by showing that 3D printed porous sensors achieve greater piezoresistive sensitivity and the decreased effect of hysteresis. An analysis of the sensors with different infill patterns and densities is done to determine which infill type produces the best results. The pressure sensing capability of the sensors is also characterized and compared to bulk material sensors. Another parameter analyzed is the effect of nozzle size on the piezoresistive behavior, with the 410 and 260 µm nozzles considered for this investigation. Finally, a recommendation is produced on how to tune the sensors' piezoresistive sensitivity by altering the named parameters.

3.2 Sensing Response

3.2.1 Cyclic Compressive Testing

The piezoresistive sensing performance of the 3D printed porous nanocomposite sensors was characterized by looking at the sensor's change in resistance when a compression load is applied. Cyclic compression tests were conducted using an Instron 5969 Column Universal Testing Machine with a load cell of 5 kN. The sensors were placed between two circular compression plates with two rectangular copper plates affixed to them. The copper plates were had wires soldered in place which connected to an Agilent 34401A multimeter that recorded the resistance of the samples. Since the samples are electrically conductive, the resistances were finite values.

Compression loads were applied using the top compression plate at cyclic compressive strains of 1%, 5%, 10%, and 20%. A constant crosshead speed of 1 mm/min was used throughout this experiment. Resistance data was collected via the copper plates as the cycling compression testing occurred.

3.2.2 Characterization of Sensing Response

The sensing response can be characterized by looking at the relative resistance change within the sensor during cyclic loading. Relative resistance change can be calculated using the equation

$$\frac{\Delta R}{R} = \frac{R - R_0}{R_0} \tag{5}$$

whereby ΔR/R represents the relative resistance change, R is the electrical resistance measured at a particular time, and R_0 is the initial electrical resistance. The relative resistance change of a sensor can be plotted as a function of the loading and unloading cycles known as the piezoresistive sensing function. Figure 25 shows the sensing function of 410 µm layer height compression sensors with grid, triangle and honeycomb infill patterns at 20%, 40% and 60% annotated infill density. Five cycles of the sensing function are shown at each maximum loading strain, and the sensing functions are compared to a 100% infill bulk sensor of the same geometry. The general behavior observed of the sensors is that the resistance of the sensors decreases with an increase of the compressive load. The samples all showcase the piezoresistive effect whereby more CNT conductive networks are formed when the material is compressed, drastically reducing the electron tunneling distance. This behavior is shown to be repeatable since all the resistance changes are identical in the loading and unloading for all 5 cycles. Figure 25(a) shows the sensing function of

the 100% infill sensor. From the graph, it is apparent that the hysteresis effect is prevalent. At each loading and unloading cycle, there are two troughs whereby the ΔR/R nears a maximum value then suddenly increases into a mini peak, followed by a decrease to the resistance change value. The effect becomes more prevalent at higher strains, and on the graph it begins to take effect at strains greater than 5%. The sensing functions also show a greater level of material relaxation whereby ΔR/R decreases in cyclic loading of the same strain and strain rate. The entire sensing function drifts down as the number of cycles increases until the material has relaxed and warmed up. This phenomenon makes the sensor unreliable during the first few cycles. One of factors that increases the effect of hysteresis is the geometry of the samples. Researchers using optimized shapes such as cylinders and truncated cones have seen a reduction in the hysteresis effect, however this technique is only mildly effective. In the 100% infill sensor, the hysteresis effect is heightened partly due to its unoptimized geometry. All samples are short, wide with sharp edges, which affects the lateral expansion of the material under compression and leads to the undoing of some conductive networks at higher strains. Figure 25(b) shows the sensing functions of the 20%, 40% and 60% infill grid sensors. On these graphs, the hysteresis effect is significantly minimized. The indicators for high amounts of hysteresis such as the mini peak and the sensing function drift are greatly reduced in the porous sensors, even at higher strains. The 20% infill sensor shows the lowest level of hysteresis, with the mini peak being non-existent. The hysteresis level starts to increase and become more noticeable when moving from the 20% infill sensor to the 40% and 60% infill sensors, although it is still significantly lower than the hysteresis of the 100% infill sensor. It is therefore apparent that the introduction of porosity by varying the infill percentage of flexible CNT/PDMS nanocomposite sensors using 3D printing results in a significant reduction of the hysteresis effect. The decrease in the hysteresis effect seems to improve the piezoresistive

sensitivity of the sensors. With the grid pattern sensors at 410 μm layer thickness, the 20% infill sensor shows the highest ΔR/R values at all maximum strains. For example, at the maximum strain of 10%, the 20% infill sensor has a relative resistance change of about -0.737, while values of -0.636, -0.614 and -0.431 are reported for 40%, 60% and 100% infill sensors respectively. The 100% infill sensor shows the lowest average resistance change values at all maximum strain values, affirming that piezoresistive sensors with high amounts of hysteresis also have a reduced sensing capacity. One of the factors that cause hysteresis particularly in elastomeric sensors is the lateral expansion of the materials due to their high Poisson's ratios. This lateral expansion creates a distance between adjacent CNTs that were part of a conductive network, effectively severing and breaking down these networks. With porous sensors created by using 3D printing to vary the infill pattern and density, the effect of lateral expansion is less present. This is because the infill is made out of single line thick walls that undergo buckling instead of lateral expansion when a compressive load is applied to higher strains. There is no distance created from adjacent CNTs moving away from each other in a lateral direction at the same strains that the bulk material experiences this phenomenon.

The effect of hysteresis is also seen to generally decrease as the porosity increases for grid sensors with a 410 μm layer thickness. Looking at the sensing functions of the sensors at all infill patterns and densities, it is evident that all the sensors tested have lower levels of hysteresis compared to the bulk material. This discovery greatly emphasizes the high value of incorporating porosity to flexible piezoresistive nanocomposite sensors using the variable infill method. The magnitude of the hysteresis reduction varies according to the infill pattern, infill density and the layer thickness. The triangle pattern sensors (Figure 25(c)) show the 20% infill sample as having the highest effect of hysteresis, and the 60% infill sample having the lowest of the porous samples.

The 20% infill sample essentially has average resistance change values that are comparable to the bulk material at all maximum strains. The sensing functions of the sensor show higher levels of hysteresis compared to the 40% and 60% samples. The behavior therefore shows an increase in the hysteresis effect as the porosity increases, a reverse of the behavior of the grid pattern samples. The honeycomb pattern sensors (Figure 25(d)) have sensing functions whose hysteresis signs are almost none-existent, further highlighting the utility of incorporating 3D printed porous structures. The sensing functions of 260 µm layer height compression sensors with grid, triangle and honeycomb infill patterns at 20%, 40% and 60% infill density are shown in Figure 26. The 260 µm layer samples behave in the same manner as the 410 µm layer samples in terms of showing a significant reduction in the effect of hysteresis compared to the bulk sensor at all infill patterns and densities. With the grid pattern sensors, the 20% infill sample is seen to have the highest amount of hysteresis, with the 40% infill sensor achieving the lowest amount of all infill patterns and densities. This behavior differs from the grid pattern sensors with a 410 µm layer thickness. It is also the second instance of the high amounts of hysteresis being seen in samples with the highest porosities. While the full mechanism of hysteresis in flexible piezoresistive nanocomposites is not well understood, a possible explanation of this behavior could be that there is a threshold porosity value at which higher porosities start to see a sharp increase in hysteresis. The 410 µm 20% infill triangle sensor, which showed similar behavior, had the highest porosity value. Therefore, it could have exceeded the threshold porosity value. While the 260 µm 20% infill grid sensor has a lower porosity value than other sensors with very low hysteresis, the thin 260 µm walls of the infill coupled with the pore size could result in a mechanism that degrades the conductive networks at higher strains. This mechanism is likely caused by the buckling and micro damage of the thin infill

walls. While the 260 µm triangle and honeycomb sensors showed significantly low hysteresis, there was no discernible pattern observed.

An effective approach used to characterize the strain sensitivity of a flexible piezoresistive sensor is by using the gauge factor. The gauge factor (GF) is seen as the relative resistance change of the sensor normalized by the applied strain. It can be calculated using the equation

$$GF = \frac{\left(\frac{R - R_0}{R_0}\right)}{\frac{L - L_0}{L_0}} = \frac{\left(\frac{\Delta R}{R}\right)}{\varepsilon} \quad (6)$$

whereby L represents the sensor height at a particular strain, L_0 is the height of the sensor at zero strain, and ε represents the applied strain. Figure 27 shows the GF values of 260 µm layer grid, triangle and honeycomb patterns sensors at different maximum strains. The general pattern of the GF shows a non-linear decrease as the strain increases, displaying asymptotic behavior at high strains. The highest GF values are therefore found at the lowest strain applied, which is 1% for this study. Figure 27(a) shows the GF of grid pattern sensors at 20%, 40%, 60% and 100% infill densities. The 20% infill sensor has the highest GF values at all maximum applied strains, achieving a maximum value of 26.1, while the 100% infill sensor has the lowest piezoresistive sensitivity with a gauge factor of 12.5. A general trend can be observed with the grid pattern sensors whereby the piezoresistive sensitivity as quantified by the gauge factor increases with an increase in porosity at multiple maximum strains. This is consistent with the findings in the sensing function discussion, whereby it was noted that the hysteresis effect generally decreases as the porosity increases for 410 µm layer grid sensors. It should be noted that the differences in the GF values between 40% and 60% infill sensors is small, and therefore a linear relationship between the pororisty and the piezoresistive sensitivity cannot be established. The triangle infill samples

showed an inverse pattern, with the 60% infill sensor having the highest GF curve with a maximum value of 17.2 followed by the 40% and 20% infill sensors (Figure 27(b)). The 20% infill sensor had GF values that are comparable to the 100% infill sensor, due to possibly exceeding the porosity threshold. The honeycomb infill sensors showed a relationship similar to the grid samples, however the differences in the GF curves were very miniscule. Collectively, the honeycomb porous sensors achieved greater piezoresistive sensitivity than the bulk material sensor due to lower hysteresis. Figure 28 shows the gauge factor curves of 260 µm layer sensors. With the grid pattern sensors, the 40% infill samples achieved the highest GF values with a maximum of 25.1. The 20% grid sample has a GF curve that was comparable to the bulk material sensor due to the large amount of hysteresis. The triangle and honeycomb samples did not show any consistent patterns, however they were able to achieve high sensitivity with maximum GF values of 21.2 and 17.5 for the triangle 20% infill and honeycomb 40% infill sensors respectively. Collectively, the GF graphs quantify the effect of hysteresis on the piezoresistive sensitivity of the CNT/PDMS nanocomposite sensors. The sensors behave very consistently, sensors with the lowest amounts of observed hysteresis factors having the highest sensitivity.

(a)

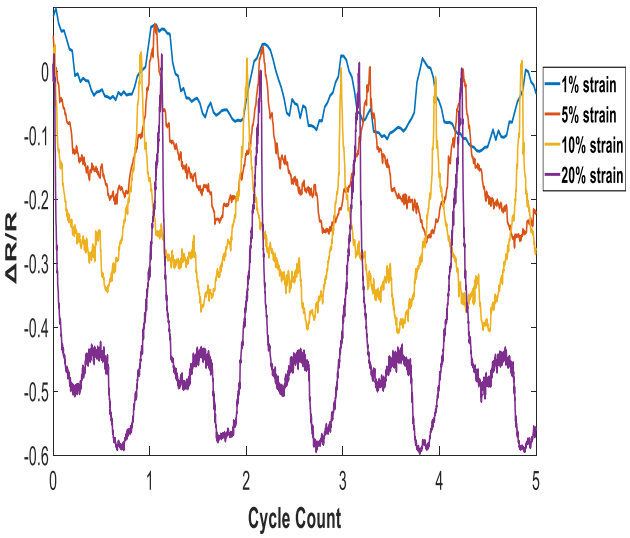

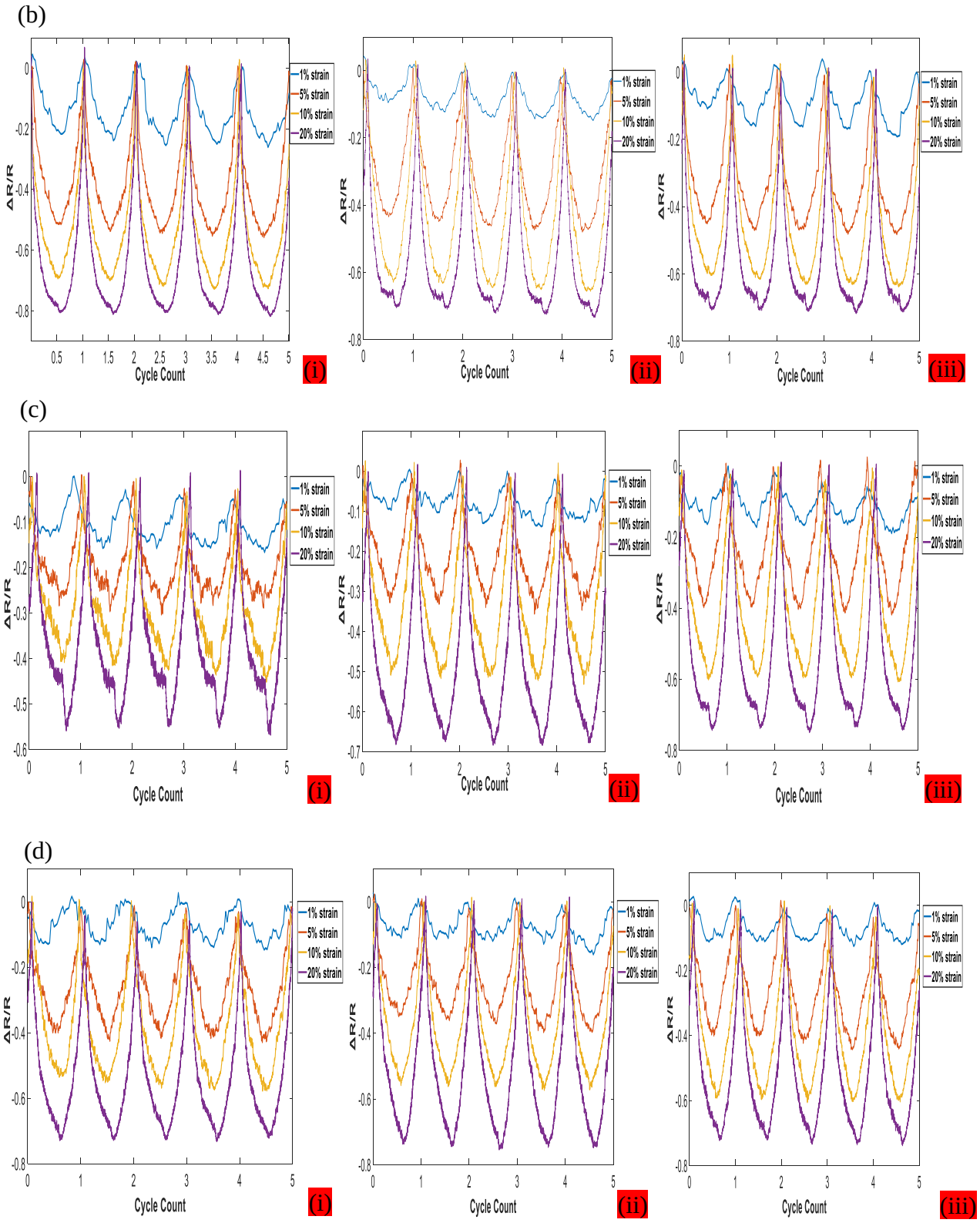

Figure 25: Sensing functions of (a) bulk sensor and compression sensors with (b) grid, (c) triangle and (d) honeycomb infill patterns at (i) 20%, (ii) 40% and (iii) 60% infill density with 410 µm layer height and thickness

(a)

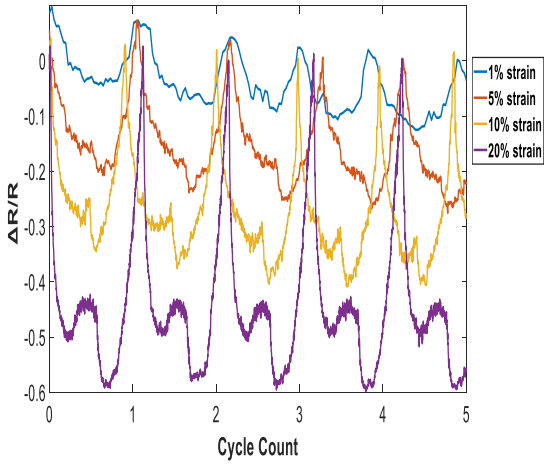
ΔR/R
Cycle Count
1% strain
5% strain
10% strain
20% strain

(b)

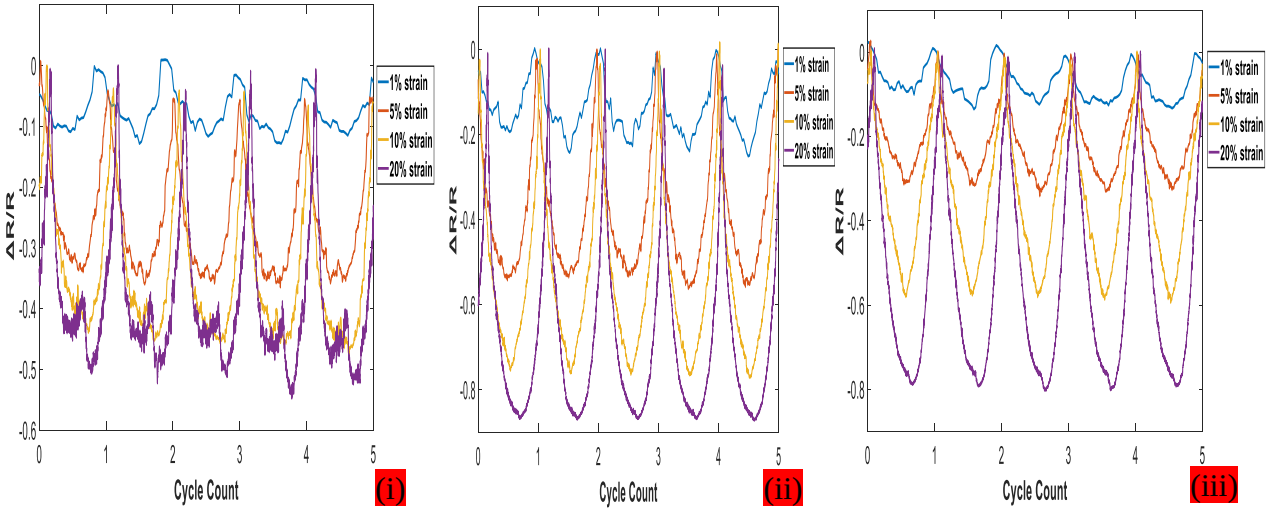
ΔR/R
Cycle Count
1% strain
5% strain
10% strain
20% strain
(i)
(ii)
(iii)

(c)

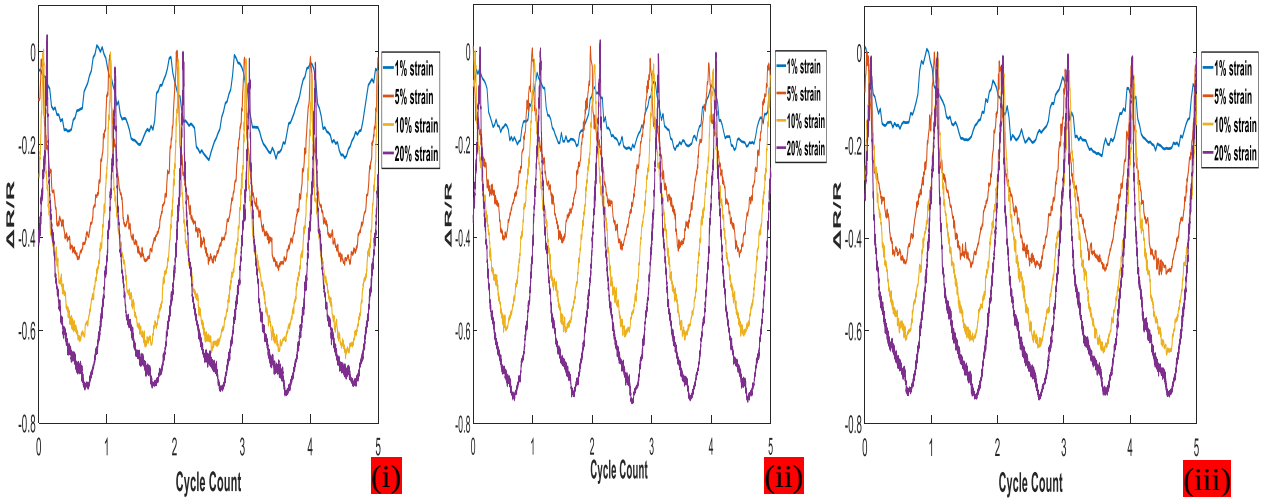
ΔR/R
Cycle Count
1% strain
5% strain
10% strain
20% strain
(i)
(ii)
(iii)

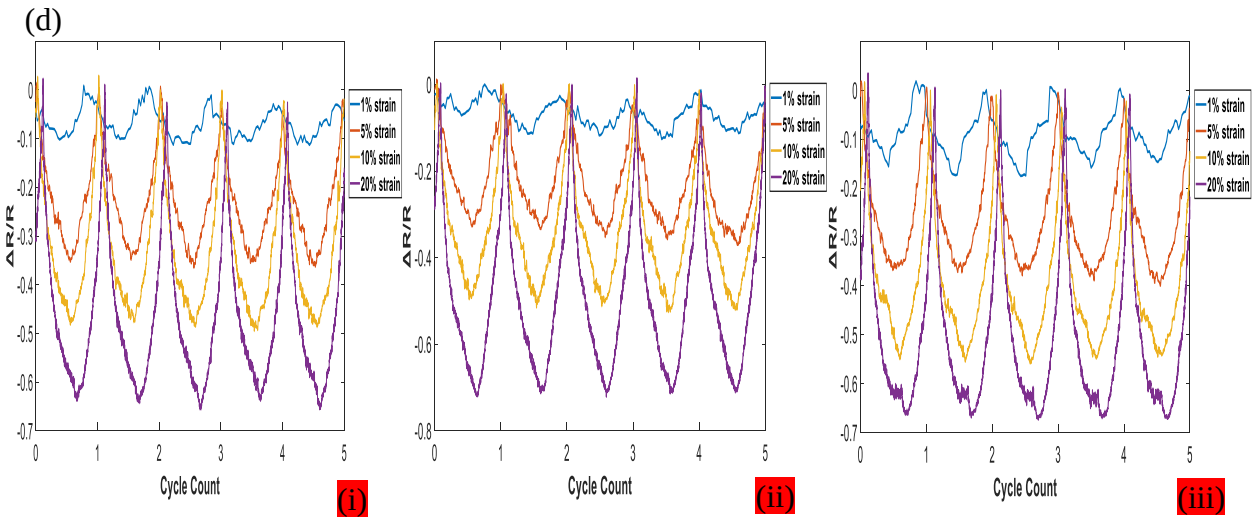

Figure 26: Sensing functions of (a) bulk sensor and compression sensors with (b) grid, (c) triangle and (d) honeycomb infill pattern at (i) 20%, (ii) 40% and (iii) 60% infill density with 260 µm layer height and thickness

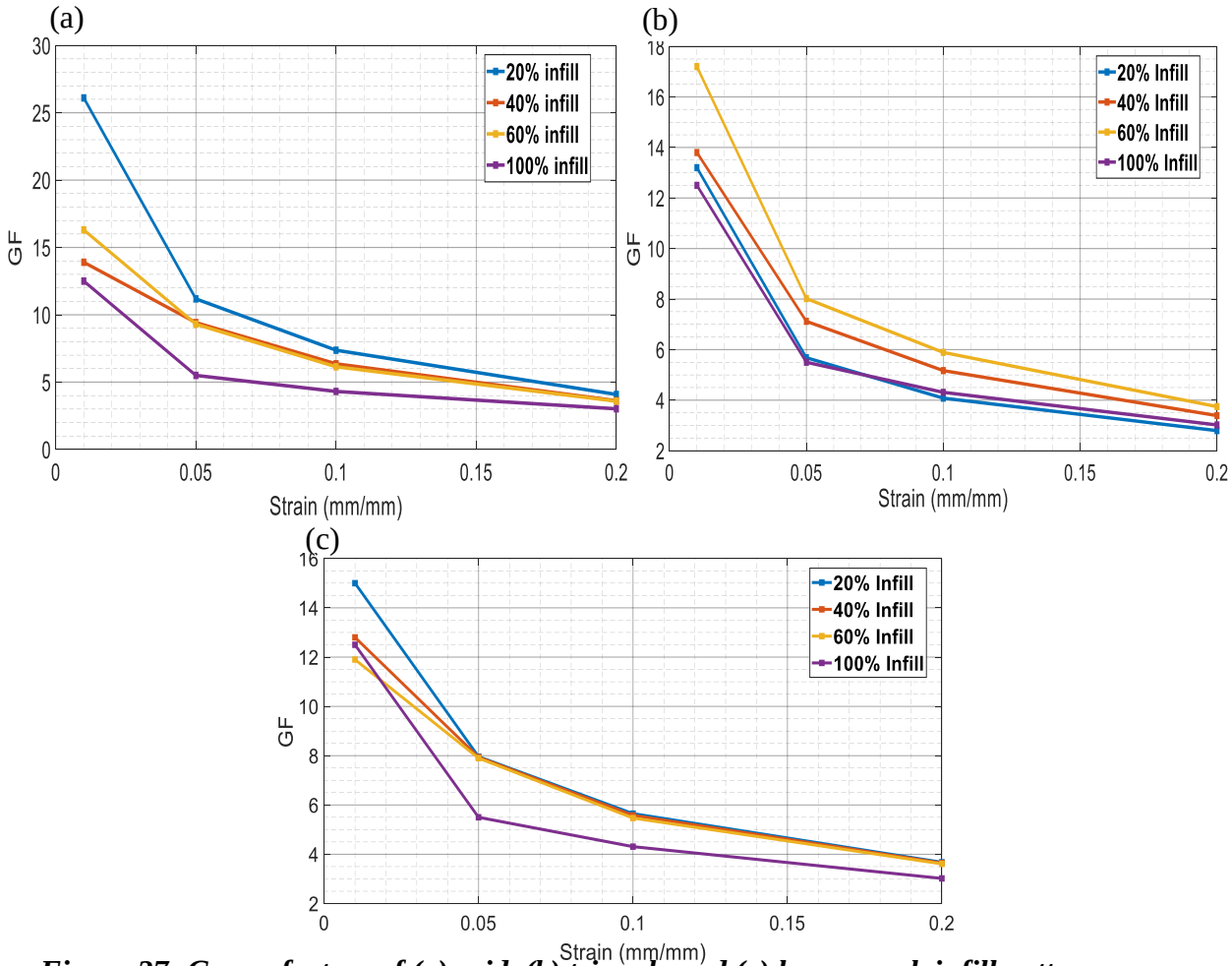

Figure 27: Gauge factors of (a) grid, (b) triangle and (c) honeycomb infill pattern sensors with 410 µm layer thickness

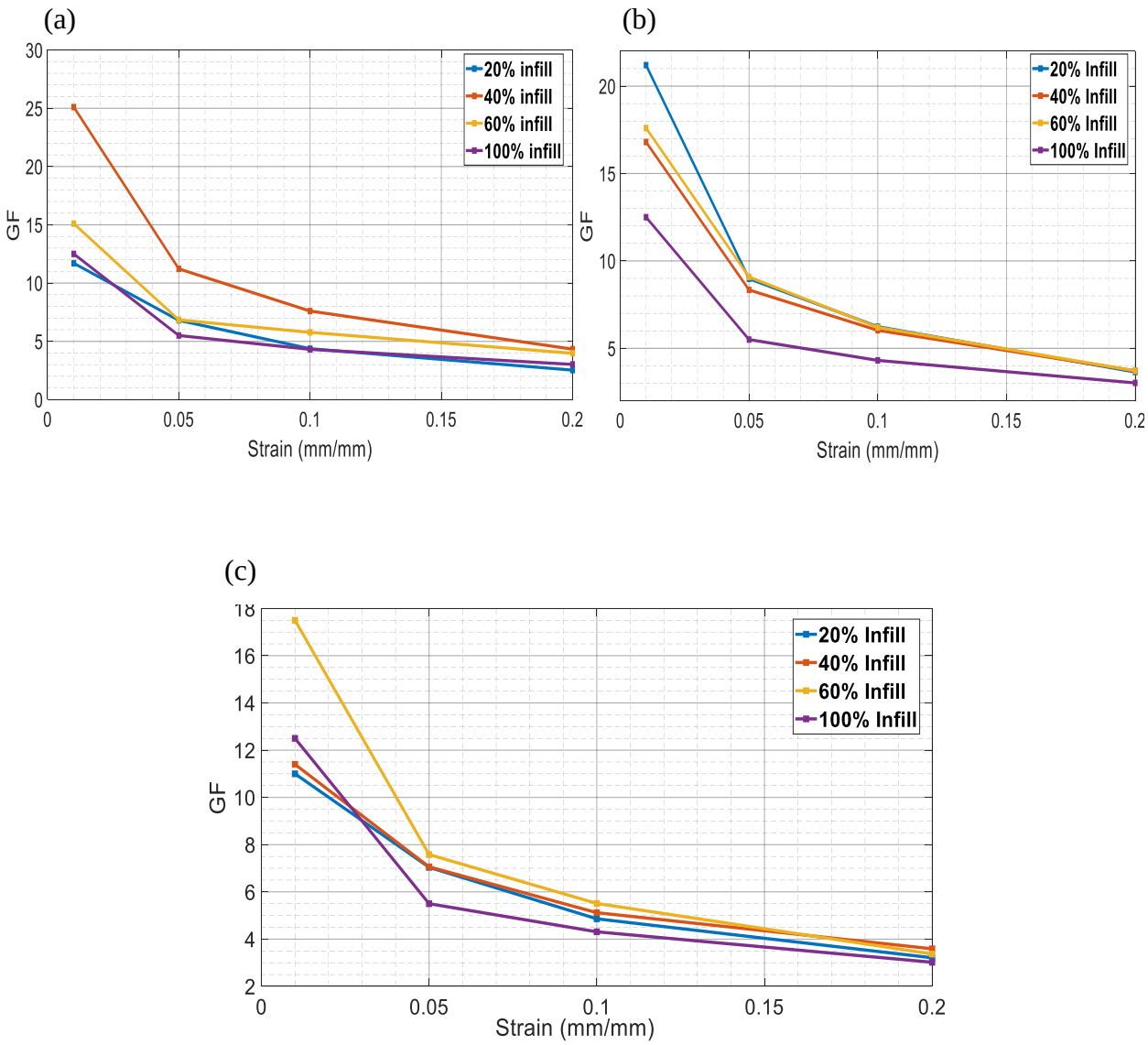

Figure 28: Gauge factors of (a) grid, (b) triangle and (c) honeycomb infill pattern sensors with 260 µm layer thickness

More and more researchers have been interested in describing the sensitivity of a piezoresistive sensor in terms of the pressure applied to cause a relative resistance change. This characterization of the sensing response has been used in the field of tactile haptic sensing. A measure that can be used in the characterization of the pressure sensitivity of flexible piezoresistive nanocomposites is the stress gauge factor, represented by the equation

$$Stress\ GF\ \frac{\left(\frac{\Delta R}{R}\right)}{\sigma} \tag{7}$$

whereby σ is the applied stress. Figures 29 and 30 illustrate the stress GF values at different maximum stresses for 410 and 260 µm layer compression sensors. The stress GF curve behaves in the same manner as the regular gauge factor, showing a decrease in the value as the pressure applied increases. Each sensor has different maximum stress values due to the variation in the stiffnesses at different infill patterns and densities. Regarding the 410 µm grid sensors (Figure 29(a)), it is apparent that the 20% infill sensor shows the highest pressure sensitivity, with a stress GF value of 190.5 MPa^{-1} compared to the values of 58.4 MPa^{-1}, 26.9 MPa^{-1} and 16.9 MPa^{-1} for the 40%, 60% and 100% infill sensors respectively. This result is drastically higher due to the 20% infill sensor's low stiffness which allows for large resistance changes with very little pressure applied. The 20% infill sensor is highly sensitive at low pressures, with the steepest relative resistance change occurring at pressures below 25 kPa. The sensor would therefore be able to perform well as a tactile sensor for various applications. However, flexible porous piezoresistive nanocomposite sensors made from other methods such as the sacrificial templating method achieve higher stress gauge factors due to their extremely low stiffness [59]. The 3D printed porous sensors have higher strain sensitivity compared to other porous sensors of the same nanofiller type and weight percentage [50]. No significant patterns of the stress GF curve differences at varying infill pattern and density could be developed to allow for the easy tuning of the pressure sensitivity. Sensors at other infill patterns and densities achieve high levels of pressure sensitivity. These include the 410 µm layer 20% infill honeycomb, 260 µm layer 40% infill grid and the 260 µm layer 60% infill honeycomb sensors which achieved the maximum stress GF values of 87.7 MPa^{-}

^{1}, 92.6 MPa^{-1} and 58.9 MPa^{-1} respectively. Overall, almost all of the sensors show increased pressure sensitivity compared to the bulk material sensor at all maximum pressures.

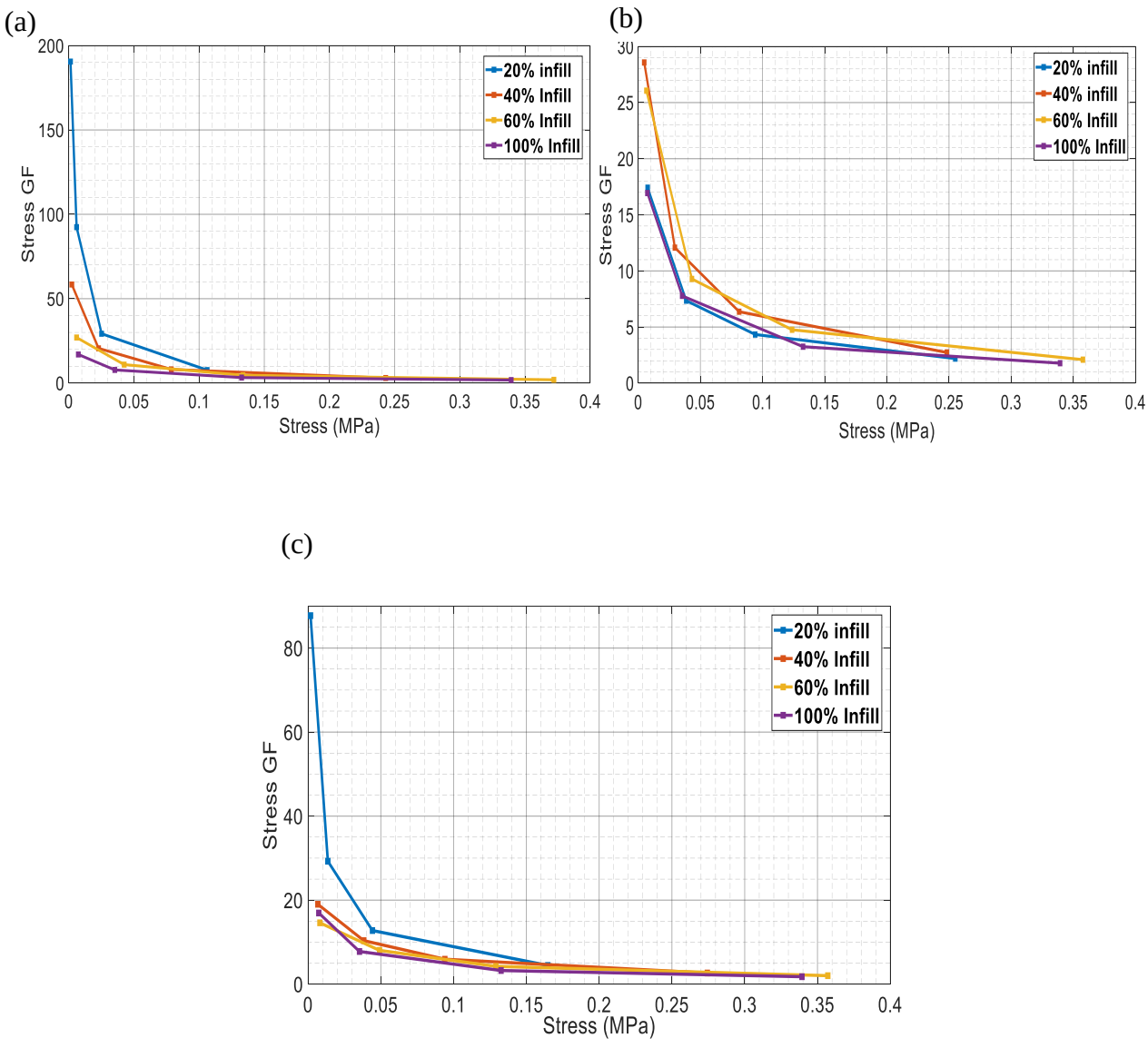

Figure 29: Stress gauge factors of (a) grid, (b) triangle and (c) honeycomb infill pattern sensors with 410 µm layer thickness

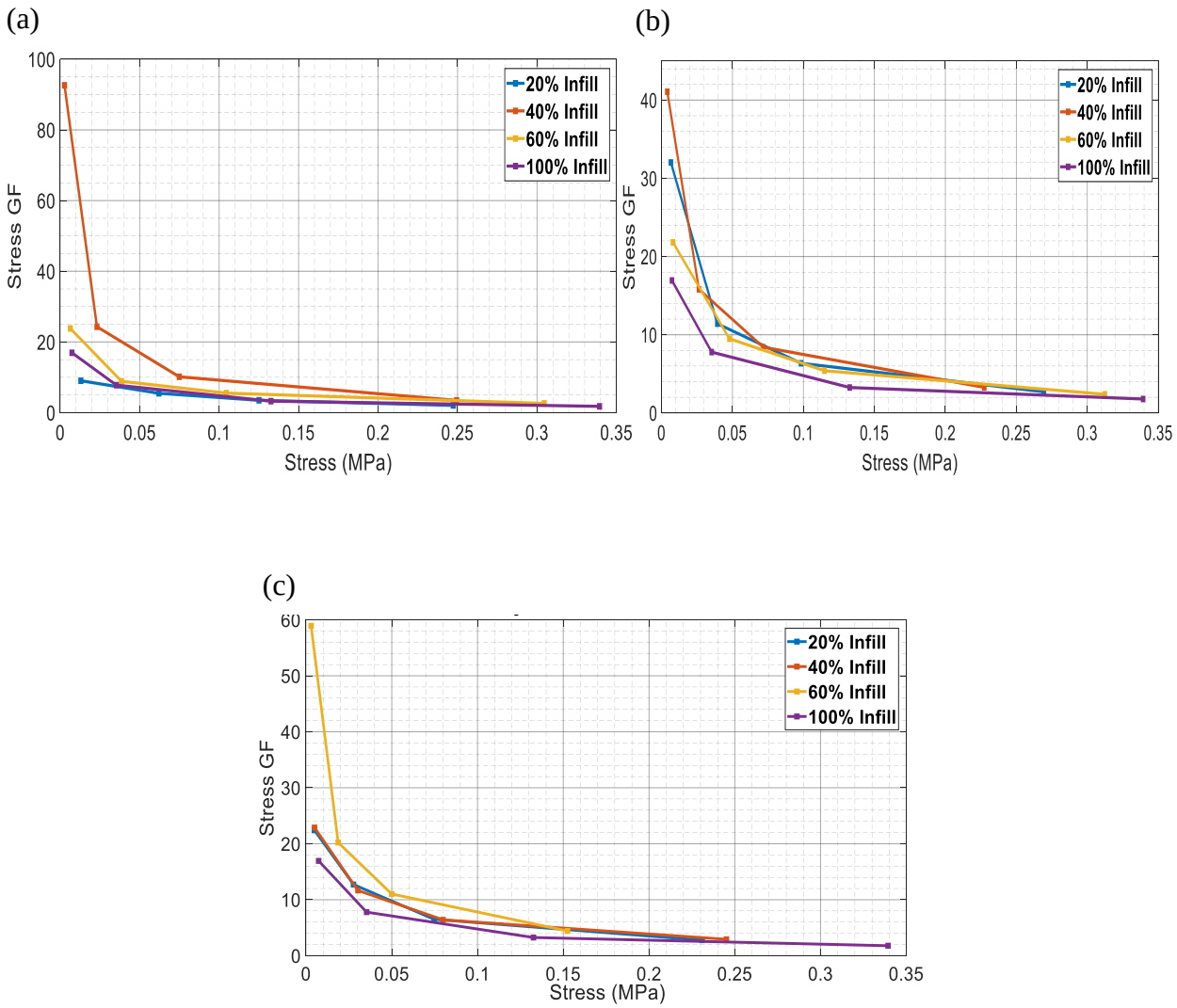

Figure 30: Stress gauge factors of (a) grid, (b) triangle and (c) honeycomb infill pattern sensors with 260 µm layer thickness

3.3 Hysteresis

A more quantitative method of characterizing the hysteresis effect within the porous 3D printed nanocomposite sensors is by observing their electrical and mechanical behavior upon cyclic loading and unloading. This allows for the observation of the lagging behind of these physical properties behind the mechanical load causing their change. This lagging behind behavior

is time dependent and is a property of viscoelastic materials such as elastomeric nanocomposites. Figure 31 displays this phenomenon. In the elastic region of a viscoelastic material, the strain recovers fully upon loading and unloading. However, the stress-strain curve does not follow the same path during the loading and unloading process, resulting in hysteresis. Hysteresis can be seen as the difference between the strain energy required to generate a given stress in a material and the elastic energy of the material at that particular stress. This hysteresis energy is dissipated as internal friction within the material during one cycle of loading and unloading. This energy is represented by the area between the diverged loading and unloading paths. This definition of hysteresis allows for the quantification of the hysteresis amount within the 3D printed porous sensors when their loading and unloading curves on the stress-strain graph are observed.

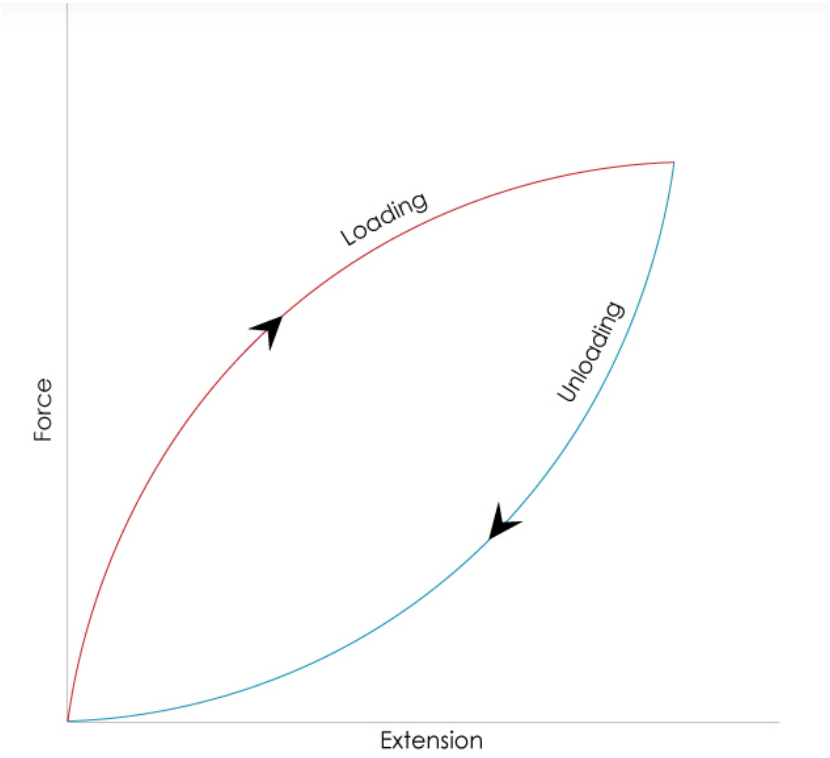

Figure 31: Effect of hysteresis in viscoelastic materials upon mechanical loading and unloading

Figures 32 and 33 show stress-strain curves of the 3D printed sensors with 410 and 260 µm layer thickness during one loading and unloading cycle at 20% strain. Looking at stress-strain curves of the 410 µm layer grid sensors shown in Figure 32(a), it is evident that the 100% infill sensor has the largest area between its loading and unloading curves. Therefore, the bulk material sensor has the highest amount of hysteresis of the sensors studied. The 20% infill sensor is shown to have the smallest area, with the area getting larger moving to the 40% and 60% infill sensors. The triangle and honeycomb pattern porous sensors also have areas between their loading and unloading curves that are significantly smaller than the bulk material sensor. The 260 µm layer sensors show similar behavior. Quantified hysteresis values of the sensors were determined using the areas between their loading and unloading curves, calculated using numerical integration, specifically the trapezoidal rule. Figure 34 shows the hysteresis energy values for the 410 and 260 µm layer compression sensors. From the bar graph, it is proven that the porous 3D printed sensors have significantly lower hysteresis values than the bulk material sensors. The behavior of the hysteresis values aligns very well with the hysteresis effect seen on the sensing functions shown in section 3.2.2. For example, the 410 µm layer grid sensors show a decrease in hysteresis with a decrease in the infill density, seen with the calculated hysteresis values of 0.0124 J/mm^3, 0.0058 J/mm^3, 0.0038 J/mm^3 and 0.0016 J/mm^3 for the 100%, 60%, 40% and 20% infill sensors respectively. These results are in line with the hysteresis behavior observed on the sensing functions of the grid infill pattern sensors. The bar graph also shows the observed behavior of the 260 µm layer 20% grid and 260 µm layer 60% honeycomb sensors having the highest hysteresis among the 3D printed porous samples. The hysteresis values seen on Figure 34 confirm the effect of hysteresis on the sensitivity of the sensors. The sensors with the lowest hysteresis such as the 410 µm layer 20% grid (0.0016 J/mm^3) and 260 µm layer 40% grid (0.0028 J/mm^3) sensors have

the highest gauge factors (26.1 and 25.1 respectively). Moreover, the bar graph allows for the recognition of patterns that were not seen on the piezoresistive sensing functions. For example, the amount of hysteresis within the 410 and 260 µm layer sensors is similar at corresponding infill pattern and densities for a majority of the porous 3D printed sensors.

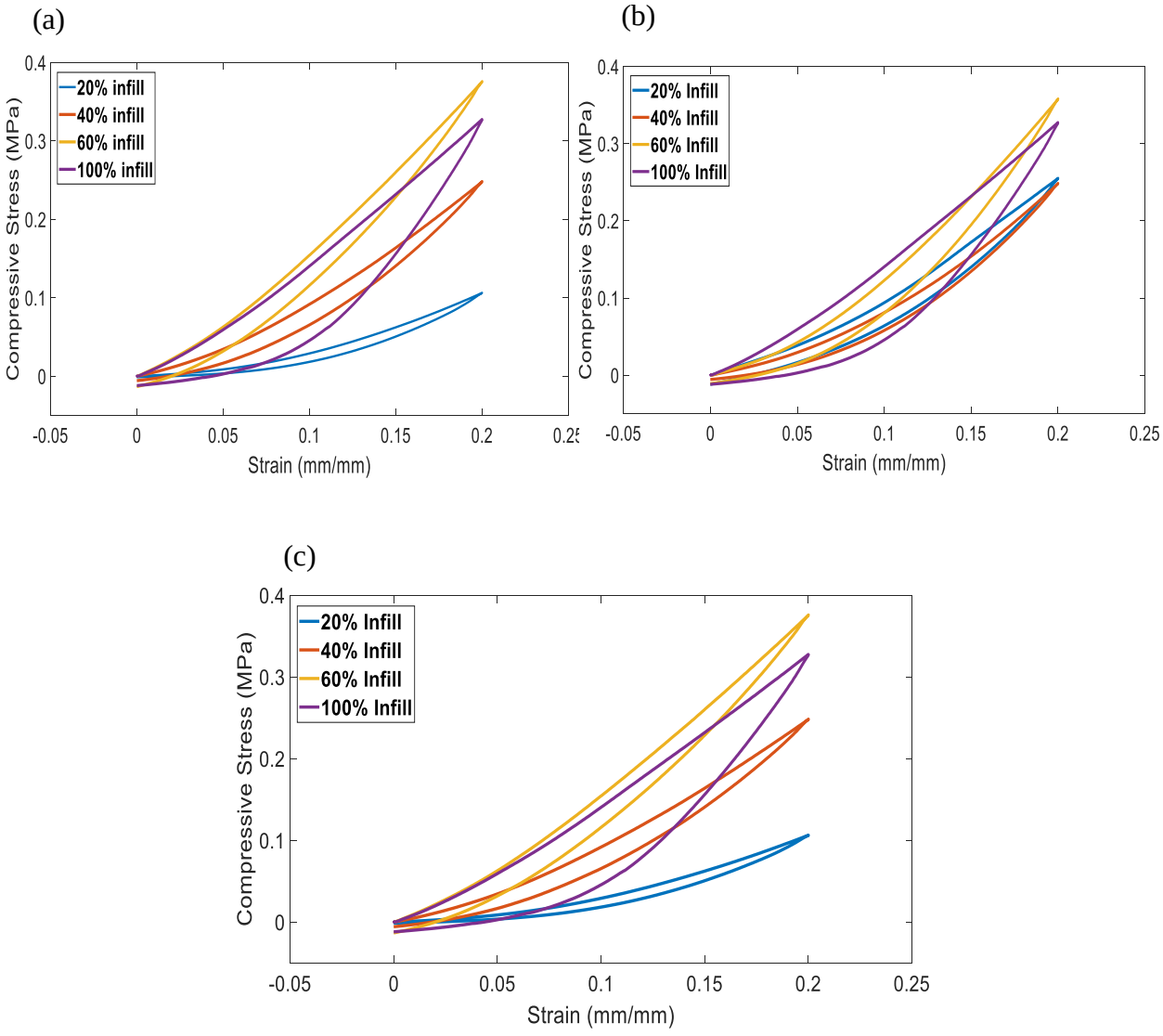

Figure 32: Mechanical hysteresis functions of (a) grid, (b) triangle and (c) honeycomb infill pattern sensors with 410 µm layer thickness

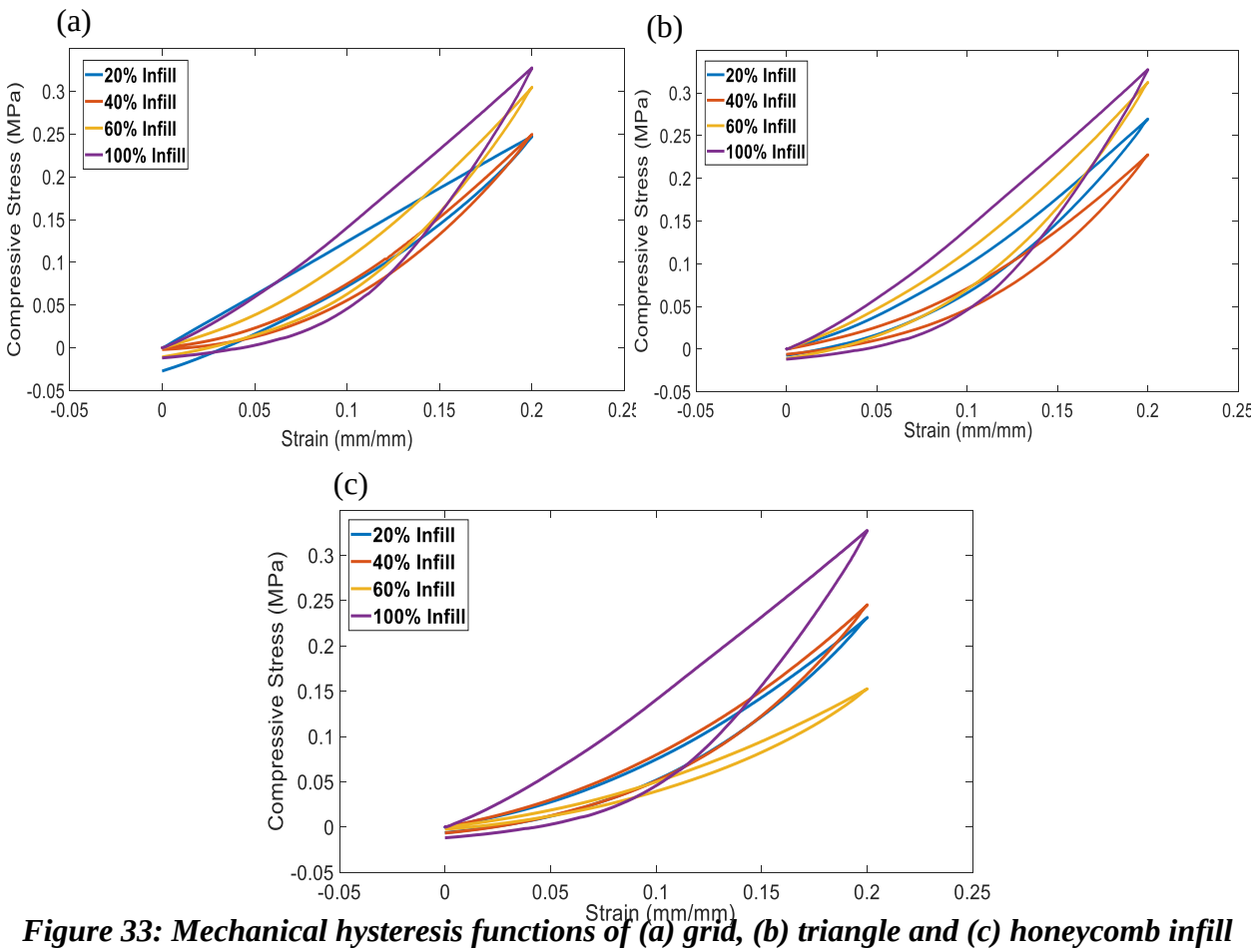

Figure 33: Mechanical hysteresis functions of (a) grid, (b) triangle and (c) honeycomb infill pattern sensors with 260 µm layer thickness

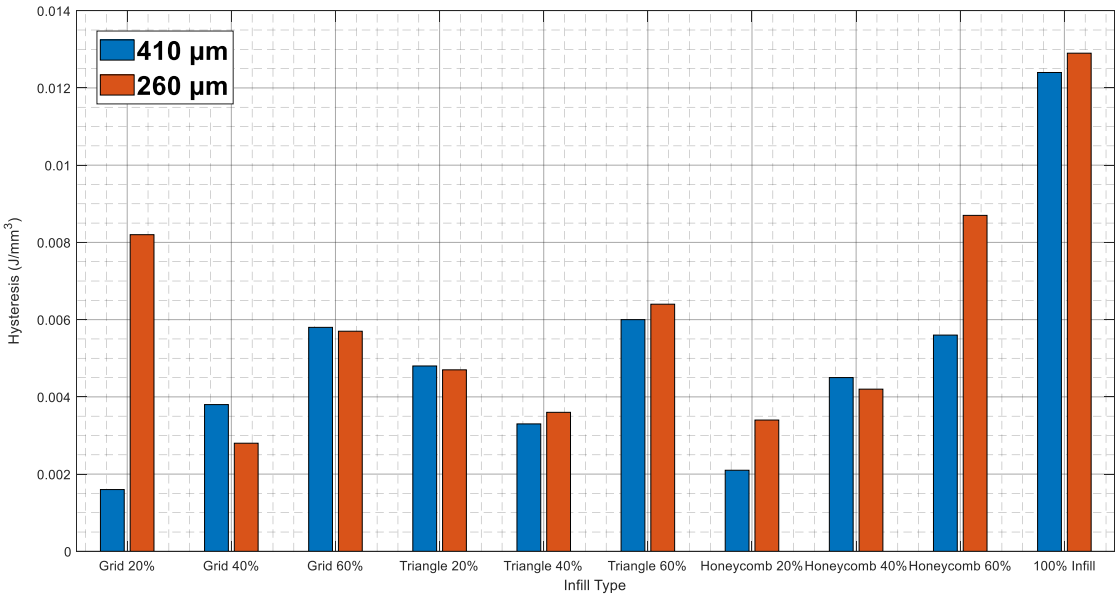

Figure 34: Effect of hysteresis represented as area between loading and unloading curves (energy dissipated)

While elastic hysteresis greatly correlates to the reduction of sensing capacity of flexible piezoresistive nanocomposite sensors, a more direct analysis can be made using the electrical hysteresis. The definition of electrical hysteresis is similar to that of elastic hysteresis in that it refers to the lagging behind behavior of the electrical response upon the loading and unloading of the mechanical load. The sensing function does not follow the same path during the loading and unloading of the mechanical load, resulting in electrical hysteresis. This form of hysteresis is responsible for the reduction in sensing capacity seen with sensors with high amounts of hysteresis. Figures 35 and 36 display the ΔR/R values of the 3D printed sensors with 410 and 260 µm layer thickness during one loading and unloading cycle at 20% strain. These curves show very similar behavior to the elastic hysteresis curves in Figures 32 and 33. The 100% infill sensor has the largest area enclosed by the ΔR/R curve upon the loading and unloading cycle, and consequently has the highest hysteresis amounts observed of the 410 µm layer sensors. The 410 µm layer 20% grid and 260 µm layer 40% grid sensors have some of the smallest areas on the electrical hysteresis curves, corresponding to the low hysteresis effect observed within the samples.

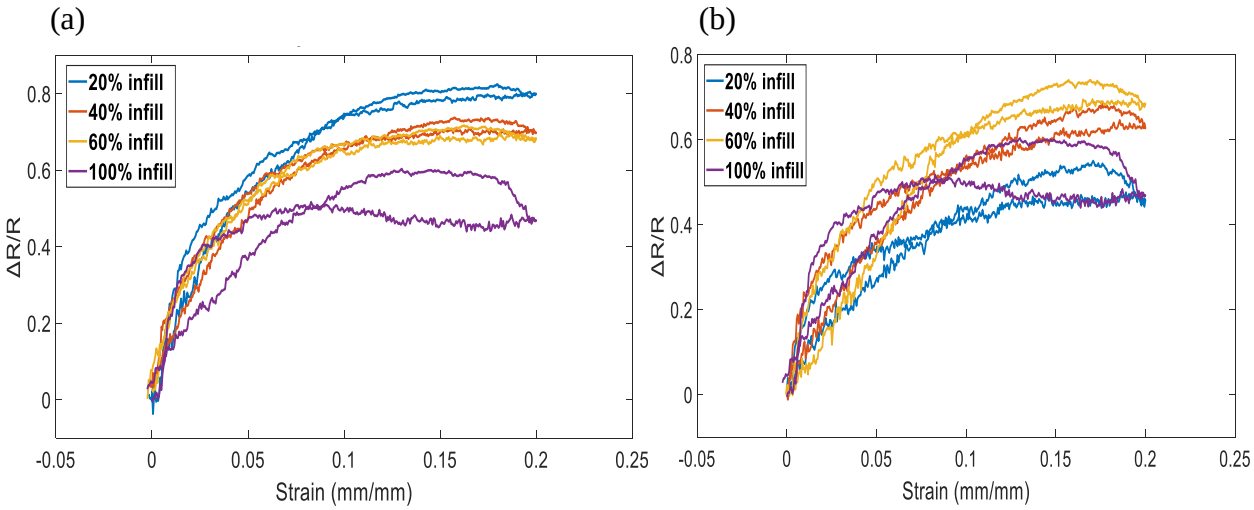

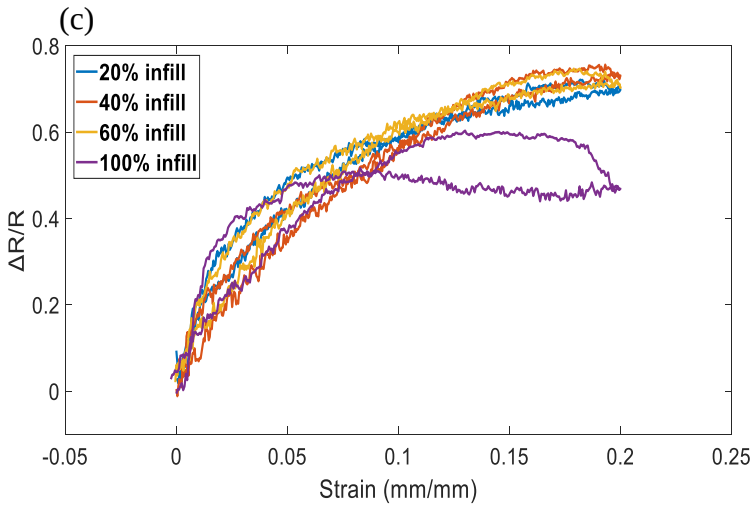

Figure 35: Electrical hysteresis functions of (a) grid, (b) triangle and (c) honeycomb infill pattern sensors with 410 µm layer thickness

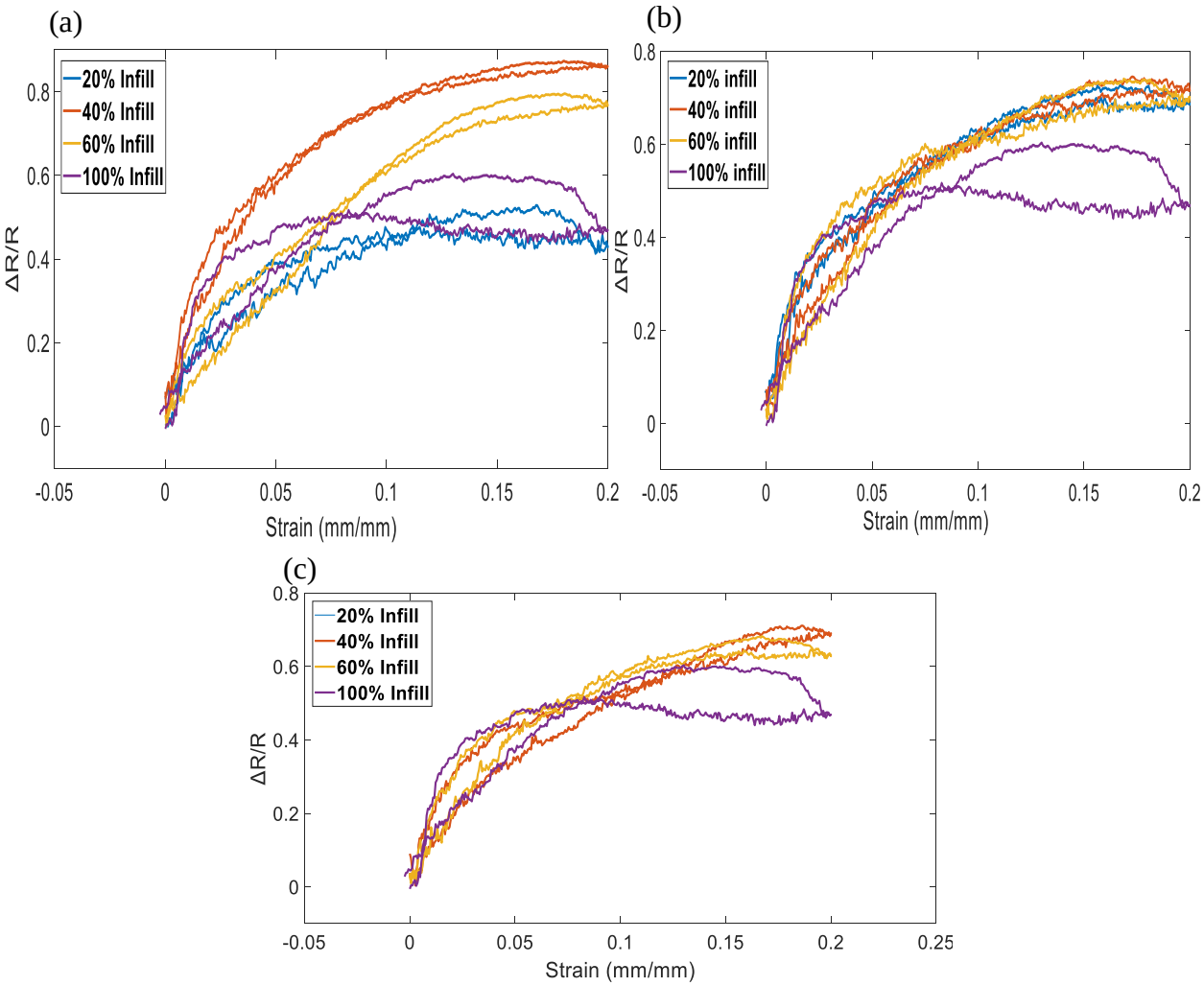

Figure 36: Electrical hysteresis functions of (a) grid, (b) triangle and (c) honeycomb infill pattern sensors with 260 µm layer thickness

3.4 Conclusion

This chapter focused on the characterization of the sensing response of 3D printed porous PDMS/CNT nanocomposite sensors. An investigation of the sensing response was done using cyclic compressive testing at strains of 1%, 5%, 10%, and 20% with a constant crosshead speed of 1 mm/min. The results showed repeatable cyclic response behavior, with all the resistance changes being identical in the loading and unloading for all observed cycles. The effect of hysteresis and its effect on the piezoresistive sensing response was thoroughly analyzed. The sensing functions of the porous sensors and the bulk sensors were scrutinized in order to observe signs of hysteresis. Common signs of the hysteresis include the presence of two troughs on each sensing function cycle whereby the $\Delta R/R$ nears a maximum value then suddenly increases into a mini peak, followed by a decrease to the resistance change value. Hysteresis is also characterized by the behavior of material relaxation whereby the entire sensing function drifts down as the number of cycles increases until the material has relaxed and warmed up. The bulk material sensor showed a high amount of hysteresis, displaying a prominent mini peak and material relaxation behavior. The 3D printed porous sensors all showed significantly reduced hysteresis at all observed strains. The low levels of hysteresis seen in these sensors was correlated to the significant increase of their piezoresistive sensitivity. The sensors' sensing capacity was quantified using the gauge factor, a measure of the relative resistance change of the sensors normalized by the applied strain. The 3D printed porous sensors were found to have significantly higher gauge factors than the bulk material sensors, with the 410 µm layer 20% grid and 260 µm layer 40% grid sensors having the highest maximum gauge factors (26.1 and 25.1 respectively) of all the sensors tested. The pressure sensitivity of the sensors was also characterized using the stress gauge factor, a measure of the sensing response normalized by the stress. The 410 µm layer 20% infill grid sample achieved the

highest pressure sensitivity, showing a good potential in tactile sensing applications. Lastly, the effect of hysteresis was quantified using stress-strain behavior on the loading and unloading cycles. The area between the loading and unloading curves was calculated to determine the numerical differences in the hysteresis amounts. The 3D printed porous sensors all achieved significantly lower hysteresis values compared to the bulk material sensors.

Chapter 4. Characterization of Material and Mechanical Properties

4.1 Introduction

This chapter focuses on the exploration of the mechanical behavior of the 3D printed porous CNT/PDMS nanocomposites. The samples' fracture strength was studied using compression and tensile column testing at a constant strain rate. The fracture stress and strain was determined for the porous compression sensors in order to determine their durability in comparison to the bulk material sensor. Porous tensile samples with a grid infill pattern were also tested for their mechanical strength in order to determine whether they would be viable as flexible strain sensors. Lastly, computer simulations were conducted using Finite Element Analysis software in order to predict the mechanical behavior of the material.

4.2 Fracture Mechanical Strength

4.2.1 Fracture Mechanical Testing of 3D printed Porous Sensors

The mechanical behavior of the 3D printed porous nanocomposite sensors was characterized by analyzing the stress and strain of the sensors until failure. Fracture compression tests were conducted using an Instron 5969 Column Universal Testing Machine with a 5 kN load cell. Two circular plates were used as part of the compression fixture, with the sensors placed between them. A ramped compression load was applied at a constant crosshead rate of 1 mm/min until the sensor being tested failed. The load applied as well as extension was recorded by the Instron software, and the variables were used to calculate the stress and strain by incorporating the measured dimensions of the sensors. The stress was calculated by factoring in the sensor's infill fraction in order to account for the porosity. Fracture tensile tests were conducted on 13 mm x 50 mm x 0.41 mm rectangular cuboids with a grid infill pattern to determine the strength of the infill

patterns in tension. The Instron column tester was fitted with screw side action tensile grips which clamped the sample 10 mm from its edge and provided 30 mm material testing length. Similar to the compression testing, the samples were loaded with a ramped tension at a crosshead rate of 1 mm/min until failure. Bulk material samples with a longitudinal and lateral rectilinear infill pattern were also tested in a similar manner in order to be used as a comparison with the porous tension samples.

4.2.2 Fracture Stress Results

The durability of the 3D printed porous nanocomposite structures can be characterized by looking at their fracture stress and strain information. Figures 37 and 38 show the stress-strain curves of 410 and 260 µm layer 3D printed porous compression sensors which were tested until failure. The stress-strain curves all show hyperelastic behavior in compression. The stress essentially increases at a rate that is higher than the rate of increase of the strain, resembling an exponential curve. The 40% and 60% infill sensors achieved the higher fracture stress and strains than the 100% infill sensors in all infill densities except one case whereby the 260 µm layer 40% infill triangle sample had a slightly lower fracture stress and strain values of 3.0 MPa and 0.492 mm/mm respectively compared to the 100% infill sensor which had the stress and strain values of 3.3 MPa and 0.504 mm/mm respectively. This behavior occurs even with the 40% and 60% infill samples having less material than the bulk material sensors. The high fracture stress and strain values are as a result of the porous sensors showing greater flexibility at higher strains, while bulk material sensors have slightly higher measure of brittleness. The pores endow the material with more space to spread within the sensor geometry during compression, meaning that there is a lesser buildup of stresses within the infill geometry that lead to early failure compared to the bulk material. Moreover, since the infill comprises of interconnected single line thick walls, a certain

amount of reversible “buckling” is likely to occur instead of only the Poisson effect. This makes the porous region more likely to fail at much higher strains compared to the bulk material which only displays the incompressible hyperelastic effect. The 60% infill sensors generally display much larger fracture stresses while failing at similar strains to the 40% infill sensors at almost all infill patterns. This is because the 60% infill sensors have the smallest pore sizes, and with compression at higher strains the material on an infill wall spreads until it bridges the pore gap and comes into contact with an adjacent infill wall which is also experiencing spreading. The stress increases drastically due to the adjacent material walls pushing against each other. This phenomenon is analyzed in greater detail in the Finite Element Analysis of the porous nanocomposite samples done in section 4.3. It can therefore be said that the 3D printed porous compression sensors are for the most part more durable than the bulk material sensors.

The 20% infill sensors showed mixed results, with three cases namely the 410 µm layer 20% infill grid, the 260 µm layer 20% infill grid and the 260 µm layer 20% infill triangle sensors showing significantly reduced fracture stress and strain values, and three other cases namely the 410 µm layer 20% infill triangle, 410 µm layer 20% infill honeycomb and the 260 µm layer 20% infill honeycomb sensors showing fracture mechanical values that are greater than those of the 100% infill sensors and are comparable to the 40% and 60% infill sensor values. These results suggest that, like with the electrical sensitivity and hysteresis results in chapter 3, there is a threshold at around 20% infill density whereby the sensor has very little supporting material and as a result fails after minimal deformation and at low stresses. This phenomenon is more prevalent with the 260 µm layer sensors which have a majority of the 20% infill samples that have low fracture mechanical properties. This is because the infill walls are much thinner compared to the 410 µm layer sensors, and as a result are more prone to crack development and damage when a

compressive load is applied. Figure 39(a) shows the failure stresses and strains of 3D printed porous tension samples. All the stress strain curves showed Neo-Hookean behavior whereby they resembled linear functions but showed a slight concave tilt at low strains. This concave tilt represented a form of plastic deformation which was not recoverable, making these samples not suitable for reliable strain sensing. The porous samples achieved fracture stresses and strains that were lower than those of the bulk material sample. The porous samples achieved similar fracture strain values of around 0.4 mm/mm with varying fracture stresses. The 20% infill sample achieved the lowest fracture stress of 0.072 MPa, followed by the 40% and 60% samples with values of 0.386 MPa and 0.512 MPa respectively, while the bulk sample showed fracture stress and strain values of 0.836 MPa and 0.478 mm/mm respectively. The low fracture mechanical values of the porous sensors can be explained by the fact that the tensile load is supported mainly by the longitudinal lines of the grid infill. These are thin lines that are more likely to fail compared to the bulk material sample which consists of longitudinal lines that are laminated in the lateral direction. As a result, the porous tension samples have limited application as strain sensors due to their low failure stress and strain. Highly flexible strain sensors which consist of 3D printed lines on a flexible elastomer substrate that have been fabricated and tested by various researchers achieve higher fracture strains and thus have a larger measurement range [60]. There was also no pattern of the sensing response observed when the infill pattern and density were varied on the tension samples. Figure 39(b) shows the fracture stress-strain curves of bulk material tension samples 3D printed with longitudinal and lateral rectilinear patterns. As expected, the longitudinal orientation achieved higher fracture stress and strain values than the lateral orientation. This is because, during tensile testing, the lateral sample has the tensile load carried by laminar bonds while the

longitudinal sample depends on the vertically oriented lines and the alignment of CNTs along each line which have been shown to reinforce material.

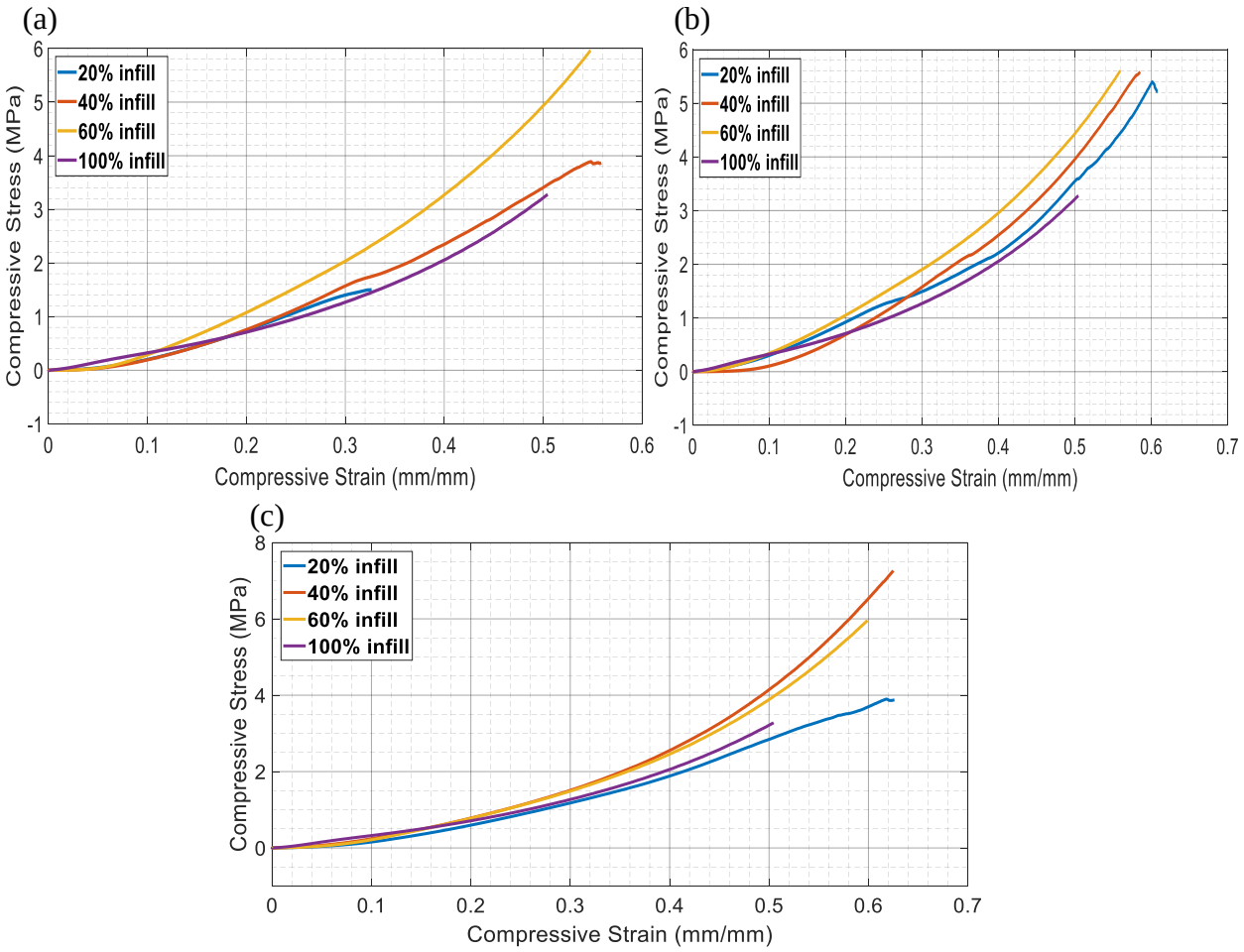

Figure 37: Fracture stress curves of (a) grid, (b) triangle and (c) honeycomb infill pattern sensors with 410 µm layer thickness

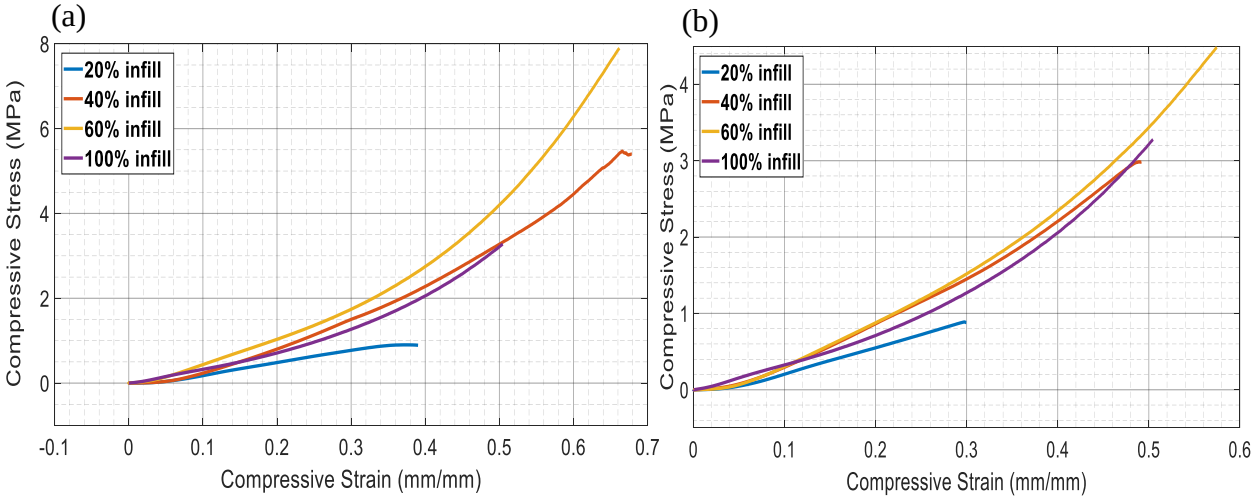

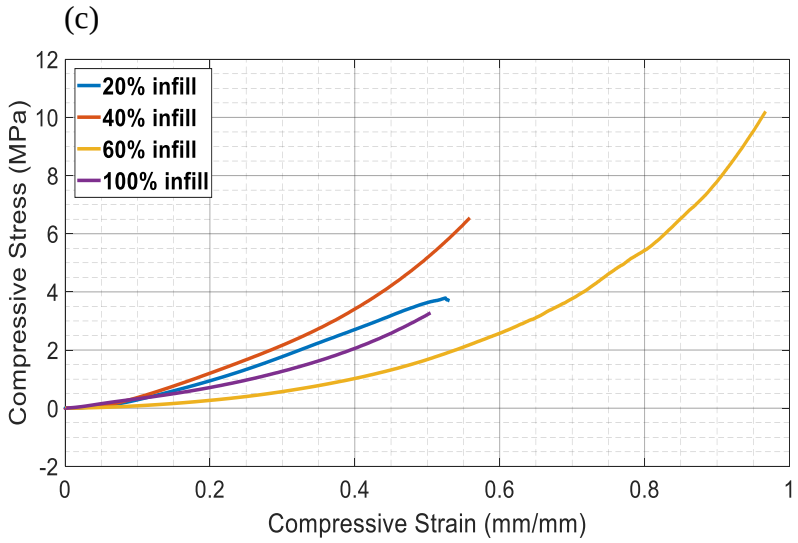

Figure 38: Fracture stress curves of (a) grid, (b) triangle and (c) honeycomb infill pattern sensors with 260 µm layer thickness

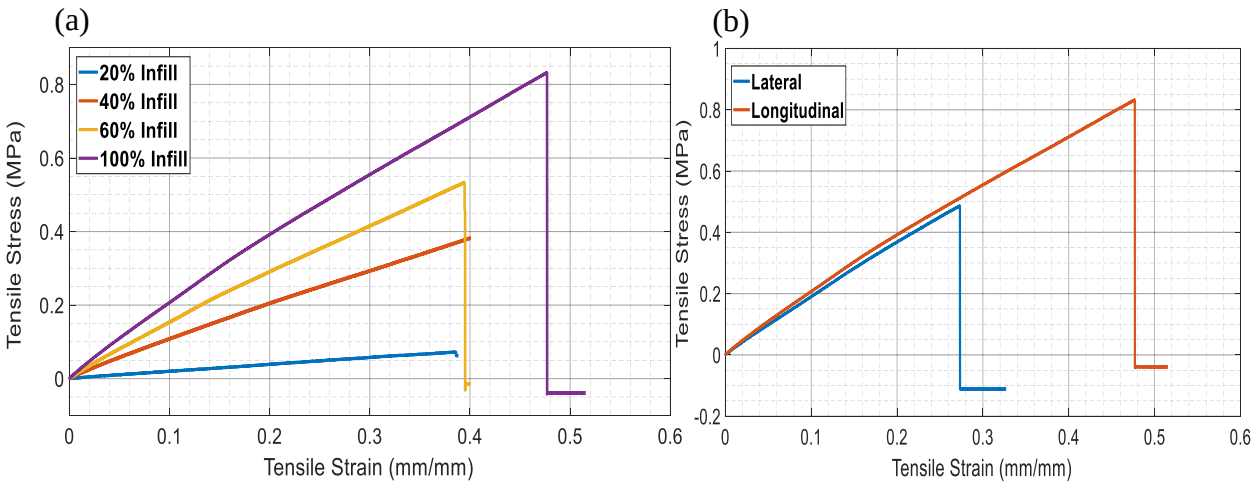

Figure 39: Fracture stress curves of (a) grid infill pattern and (b) longitudinal and lateral rectilinear infill tension samples with 410 µm layer thickness

4.3 Computer Simulation of the Mechanical Behavior

4.3.1 Material definition, boundary conditions and Finite Element Analysis

Computer simulation in the form of Finite Element Analysis (FEA) was used to investigate the mechanical behavior of the 3D printed porous CNT/PDMS nanocomposites. This simulation was performed as a static structural FEA using ANSYS Workbench R19. To begin the analysis, a

definition of the material properties was performed. The CNT/PDMS nanocomposite does not show linear mechanical behavior due to the hyperelastic properties of the polymer matrix, therefore hyperelastic material curve fitting was performed. Hyperelastic materials are defined as materials that experience large elastic strains and deformation with small volume change. These materials are usually rubbery, incompressible and display non-linear elastic behavior that is independent of the strain rate. Hyperelastic material curve fitting involves using stress-strain data obtained from experimentation. In this case, a cylinder was 3D printed using the CNT/PDMS nanocomposite ink formulation used throughout this study. The cylinder was loaded in compression using the Instron column tester until fracture, and the stress-strain results were entered into the ANSYS Workbench software. A material property curve was then fitted onto the experimental stress-strain curve. This material property curve was chosen from hyperelastic constitutive models that show material nonlinearity and large deformation. The hyperelastic constitutive model is chosen if it fits the shape of the experimental stress-strain curve the closest. Various hyperelastic models that show the behavior of commonly studied rubbery materials have been discovered and published in literature. For the compression study, the Mooney-Rivlin model which has a working strain range of 30% in compression and 200% in tension was used. This model is derived from the strain energy function, given as the equation

$$W = W(\bar{I}_1, \bar{I}_2, J) = W(\bar{I}_1, \bar{I}_2) + U(J) \tag{8}$$

whereby W is the strain energy, $\bar{I}_1$ and $\bar{I}_2$ are the invariants, U is the deformation energy and J is the Jacobian. The invariants are expressed as a functions of stretch rations seen one the following equations

$$I_1 = \lambda_1^2 + \lambda_2^2 + \lambda_3^2 \tag{9}$$

$$I_2 = \frac{1}{\lambda_1^2} + \frac{1}{\lambda_2^2} + \frac{1}{\lambda_3^2} \tag{10}$$

$$I_3 = \lambda_1^2 \lambda_2^2 \lambda_3^2 = J^2 \tag{11}$$

with λ_1, λ_2 and λ_3 representing the stretch ratios which are ratios of the initial and final lengths in the principal direction. The stretch ratio can be represented by

$$\lambda = 1 + \varepsilon \tag{12}$$

whereby ε is the applied engineering strain. The corresponding Second Piola Kirchoff stress is given as

$$\bar{S} = \frac{\partial W(\bar{I_1}, \bar{I_2})}{\partial E} \tag{13}$$

with E representing the elastic part of the Green strain tensor. There are four Mooney-Rivlin models, depending on the number of inflection points observed on the experimental stress-srain curve. The stress-strain curve of the cylindrical sample in compression has one-inflection point, therefore the Mooney-Rivlin model types that result in the closest fit are the 3-parameter and 5-parameter models. The Mooney-Rivlin 3-parameter model was chosen since it achieved the best curve fit. The strain energy function of this model as expressed as a function of the strain invariants can be written as

$$W_{(3)} = C_{10}(\bar{I_1} - 1) + C_{01}(\bar{I_2} - 1) + C_{11}(\bar{I_1} - 1)(\bar{I_2} - 1) + \frac{1}{d}(J - 1)^2 \tag{14}$$

whereby C_{01}, C_{10} and C_{11} are material constants that are determined when the curve is fit onto the experimental stress-strain curve. The corresponding Mooney-Rivlin 3-parameter uniaxial Second Piola Kirchoff stress is represented by the equation

$$\bar{S}_{3p} = 2C_{10}\left(\lambda - \frac{1}{\lambda}\right) + 2C_{01}\left(1 - \frac{1}{\lambda^3}\right) + 6C_{11}\left(\lambda^2 - \lambda - 1 + \frac{1}{\lambda^2} + \frac{1}{\lambda^3} - \frac{1}{\lambda^4}\right) \quad (15)$$

whereby $\bar{S}_{3p}$ is the Mooney-Rivlin 3-parameter uniaxial stress [61]. The hyperelastic curve fitting process is shown on Figure 40. The points on the stress-strain curve seen in the bottom right section of image represent experimental mechanical data. The curve running along the points is the hyperelastic material curve fit. In the bottom left section, the curve fit type selected is the Mooney-Rivlin 3 parameter model. The calculated values of the material constants C_{01}, C_{10} and C_{11}, as well as the incompressibility factor D_1 are also shown in the section. Once the material properties were well defined, the cylindrical geometry with a diameter and height of 10 mm was constrained as shown on Figure 41.

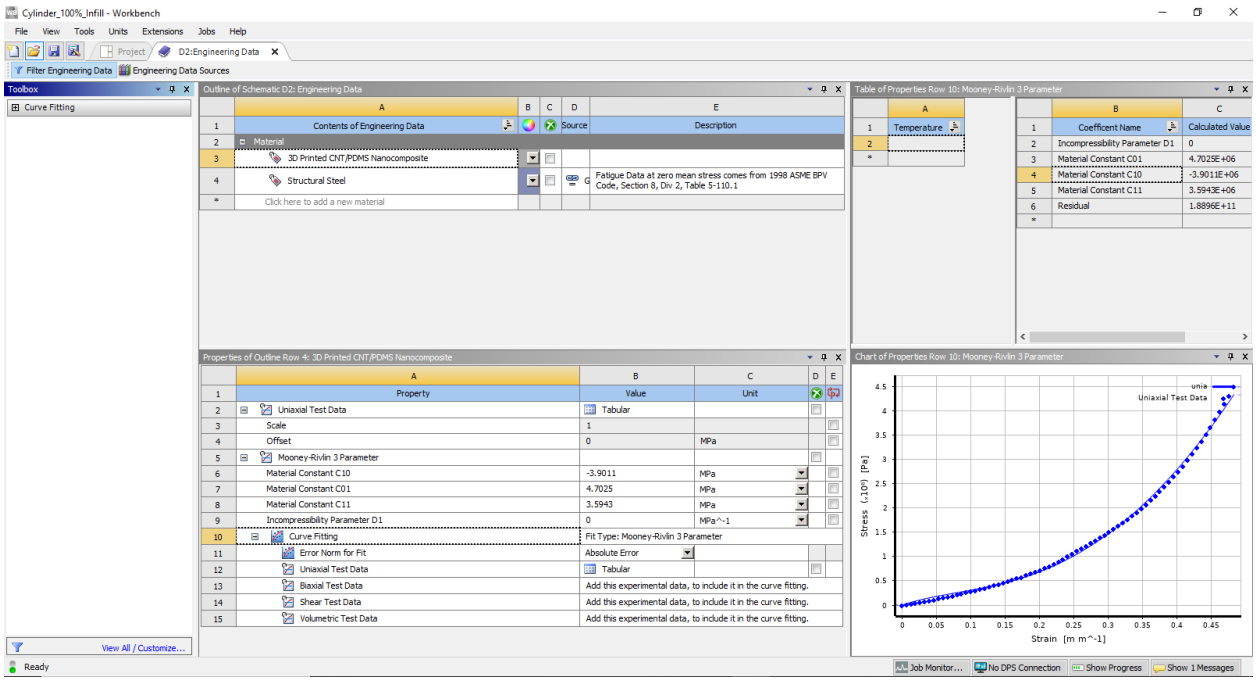

Figure 40: Mooney-Rivlin 3-Parameter hyperelastic material curve fitting using 3D printed PDMS/CNT nanocomposite cylindrical compression sensor stress-strain data

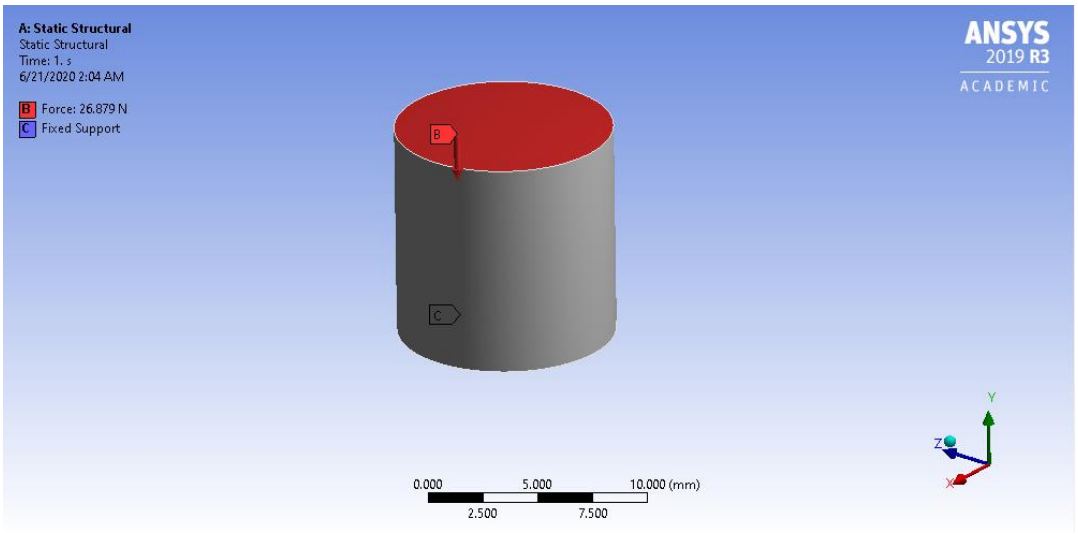

Figure 41: FEA constraints on cylindrical geometry

The 3D printed cylindrical CNT/PDMS nanocomposite sensor's stress-strain data was used to define the material properties of the 100% infill sensor as well as the 20%, 40% and 60% infill sensors with grid, triangle and honeycomb infill patterns. Only 410 µm layer sensors were used for this mechanical analysis. Using the material properties defined by the cylindrical test results, a verification test was performed to determine the accuracy of the hyperelastic material curve fit model. The cylinder, 100% infill sensor and the 3D printed porous sensors were simulated using the boundary and loading conditions used in their experimental fracture mechanical tests. Figure 42 shows the experimental data plotted against the simulation data for the cylinder, 100% infill cuboid sensor and the 20% infill grid sensor using the hyperelastic curve fitted material properties. All the geometries achieved accuracy with the experimental data, showing the validity of using the modeled material properties and the curve fit model. All other infill patterns and densities had stress-strain plots generated using FEA that achieved very good accuracy to the experimental data.

Similar analysis was performed for the tension samples. A Neo-Hookean hyperelastic curve fit model was used to define the material properties in tension due to the behavior of the 3D

printed CNT/PDMS nanocomposite material in tension. The model was derived from the strain energy equation highlighted by Equation 8, and it can be written in the form

$$\sigma_{11} = \frac{4C_1}{3J^{\frac{5}{3}}}\left(\lambda^2 - \frac{J}{\lambda}\right) + 2D_1(J-1) \tag{16}$$

$$\sigma_{22} = \sigma_{33} = \frac{2C_1}{3J^{\frac{5}{3}}}\left(\frac{J}{\lambda} - \lambda^2\right) + 2D_1(J-1) \tag{17}$$

whereby σ_{11}, σ_{22} and σ_{33} are the principal stresses, C_1 is a material constant and D_1 is the incompressibility parameter [62]. Figures 43 and 44 show the Neo-Hookean hyperelastic curve fit model as well as the boundary and loading conditions of a tension sample with a 13 mm x 30 mm x 0.41 mm testing volume. The material properties for the tension simulations were determined using the experimental stress-strain data obtained from the bulk material tension 3D printed sample with a longitudinal rectilinear pattern. This was due to the fact that the porous tension samples tested have a grid infill that is mainly supported by longitudinal lines in uniaxial tension. Figure 45 highlights the experimental data plotted against the simulation data for the 100% infill tension sample and the 20% infill grid sample using the hyperelastic curve fitted material properties. Like the compression sensors, the tension samples achieved an excellent fit, validating the use of the Neo-Hookean hyperelastic curve fitted material properties.

4.3.2 Simulation Results

Solid models of the porous geometries were created on Solidworks using the dimensions obtained from the sliced model gcode.

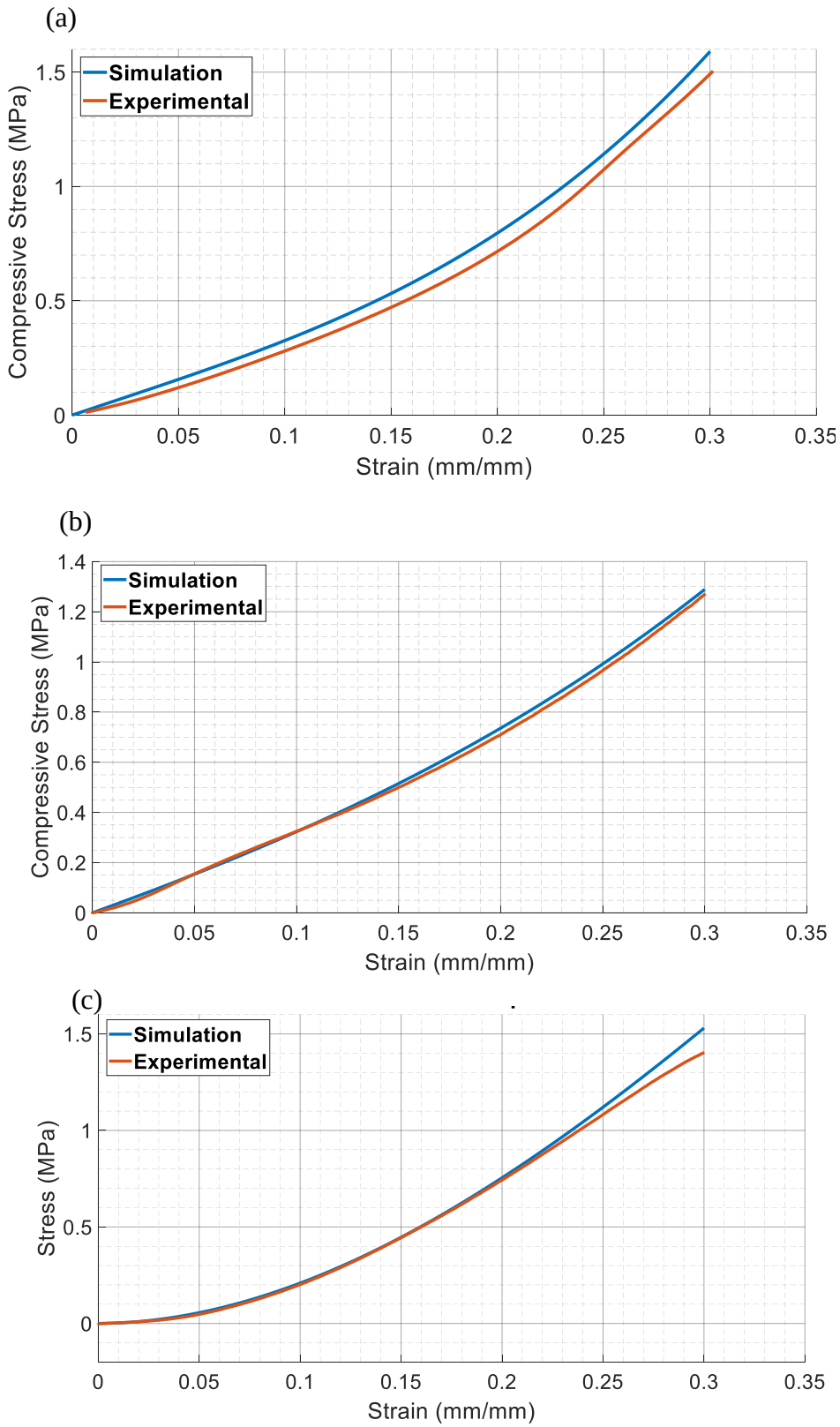

Figure 42: Experimental stress-strain data of (a) 100% infill cylidrical, (b) 100% infill square and (c) 20% infill grid compression sensors plotted against FEA results

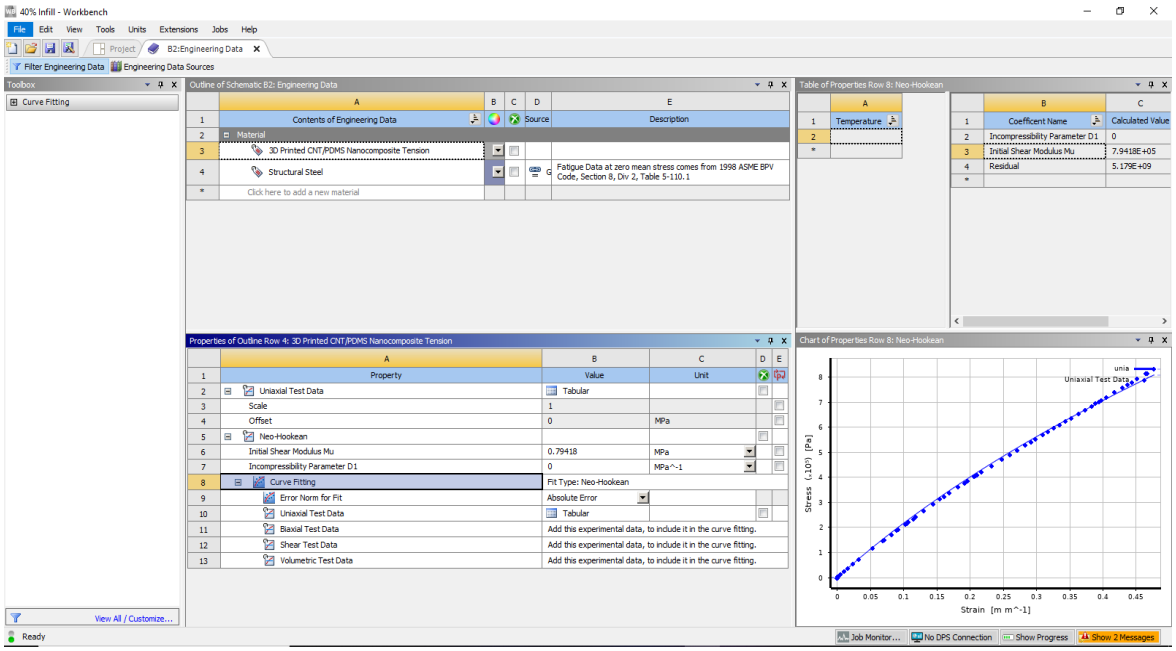

Figure 43: Neo-Hookean hyperelastic material curve fitting using 3D printed PDMS/CNT nanocomposite tension sample stress-strain data

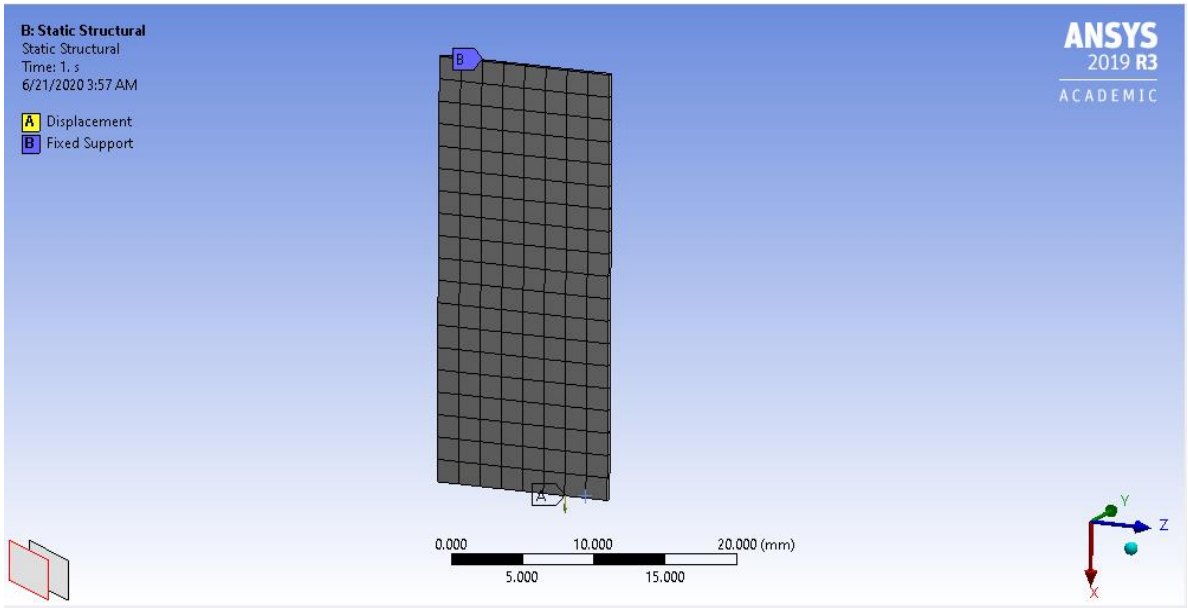

Figure 44: FEA boundary and loading conditions on rectangular geometry

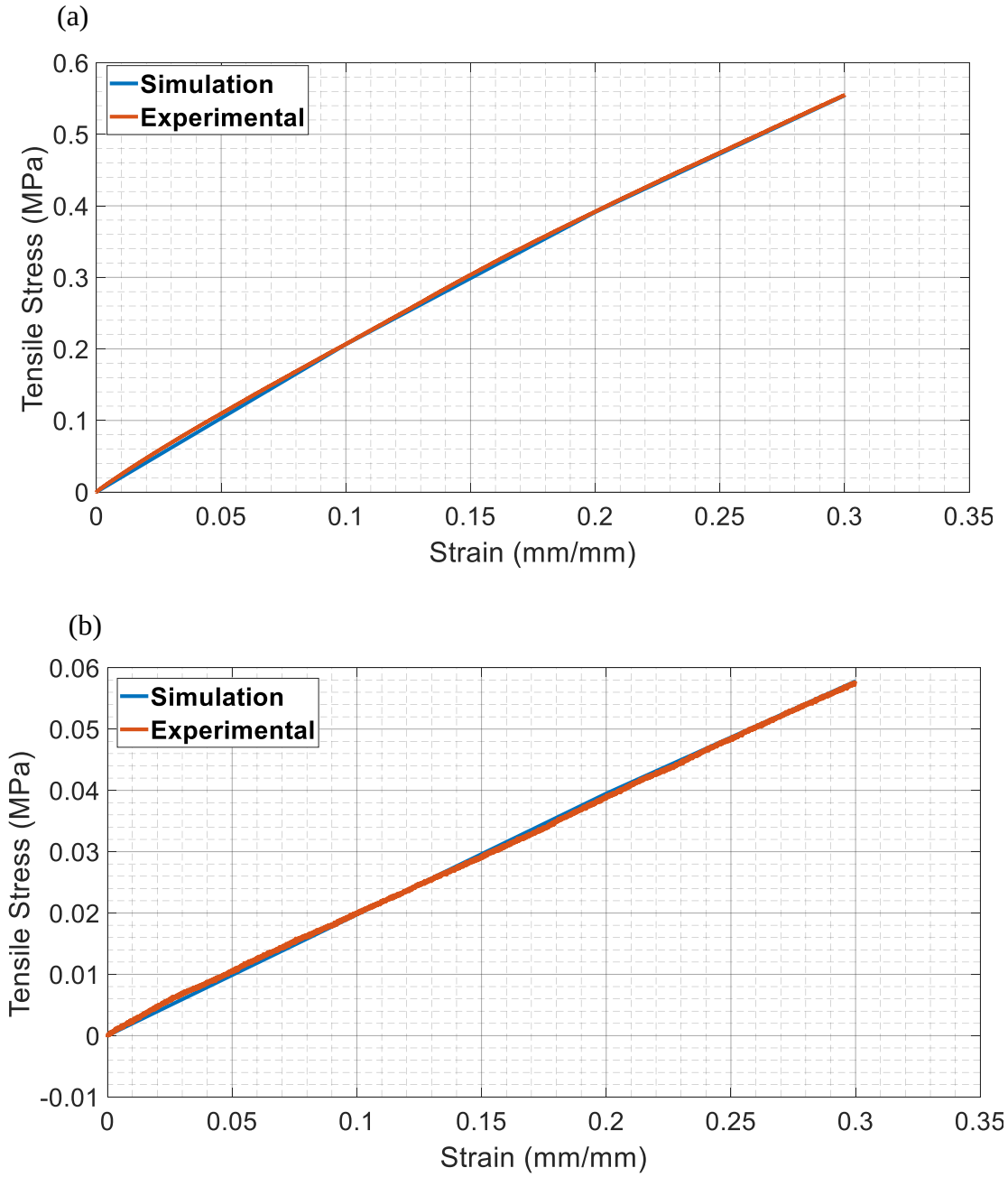

Figure 45: Experimental stress-strain data of (a) 100% infill and (b) 20% infill grid tension samples plotted against FEA results

410 µm layer 3D printed porous compression sensors were constrained with a fixed support at their base and loaded with a ramped displacement achieved in experimentation. Figure 46 shows their FEA results, specifically the Von Mises stress at 30% strain. These results allow for the analysis of the areas of high stress, as well as showcase how the sensors behaved in deformation.

The bulk material sensor is shown to have regions of high stress toward the edge of the sample. This is due to the geometry of the sensor, since objects with sharp corners has higher stress concentrations towards its edges. The 20% infill grid sensor shows stress and deformation behavior that is consistent to observations made in the fracture mechanical testing section. Due to the large pore size and the thin infill walls, a large portion of the stress is concentrated in the infill region, with the maximum stress occurring in this space. The infill is shown to be undergoing bending and buckling instead of material spreading and the Poisson effect. The sensor is therefore likely to fail in the infill region. These observations are consistent with the determinations made in section 4.2.2 which explained why the sensor failed at a low stress and strain relative to the other sensors. The 40% and 60% grid sensors, however, have high stresses along their respective edges. This is where the sensors have two lines as a perimeter, instituted in order to aid the completion of the 3D printing process. As the pore size decreases, the infill began to exhibit bulk material properties. The infill walls experienced the Poisson effect instead of buckling, with the spreading material occupying more of the pore space. The 60% infill sensors experience the most of this phenomenon, with the pores almost closing entirely. Material from adjacent lines comes into contact with each other and exerts a force, making the entire sensor less compliant and adding to the stress experienced. This is also consistent with the findings in section 4.2.2 since this effect results in much higher fracture stresses than the other sensors due to the contact between adjacent lines. A non-linear mesh adaptive region as well as contact regions had to be implemented in order to solve the 60% infill simulations. The 60% infill sensors essentially behave like bulk material sensors at high strains since the pores become fully enclosed, providing another explanation for the increased amounts of hysteresis at these strains. The 40% and 60% infill sensors are more likely to fail along the edges since the infill has room to spread laterally until the pores are completely enclosed, thereby

lessening the stress buildup within the center of the sensors. This behavior is also seen in the triangle and honeycomb infill patterns. Although they have pores as large as the 20% infill grid sensor, the 20% triangle and honeycomb sensors show more structurally stable infill regions. The sensors are reinforced by the large volumes of the joints where infill lines connect, preventing material buckling and bending. Figure 47 shows the images of fractured 20% infill sensors taken immediately after testing. As predicted, the 20% grid infill sensor fractured within the infill region, while the triangle and honeycomb sensors fractured at the edges. The 100% infill sensor fractured at the edges and the cracks traveled inwardly.

Tension samples were constrained with a fixed support at their base and loaded with a ramped tensile displacement. Figure 48 shows the FEA results of tension samples tested to 30% strain. The region of maximum strain was recorded close to the locations where the fixed support and the load condition was applied for all samples. This is consistent to the fracture locations found with experimentation, as highlighted in Figure 49, which were often found near the tensile grips. The 100% infill sample shows a concentration of stress in the center of the material. The porous samples have results that show that the longitudinal infill lines bear almost the tensile load, with maximum stresses occurring at the joints where longitudinal and lateral lines intersect. The 20% infill sample achieves the lowest failure stress and strain due to having less longitudinal infill lines that can support the load compared to the other samples. The increase in the number of vertical lines achieved by increasing the infill density results in higher failure stresses and strains, with the 100% infill sample achieving the highest failure mechanical values since it has the largest number of longitudinal lines. This is consistent with the failure mechanical analysis provided in section 4.2.2.

(a)

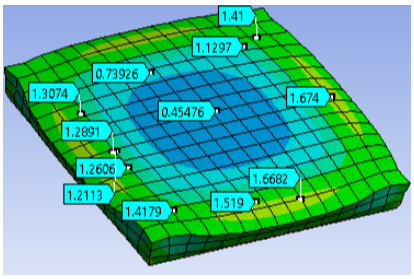

(b)

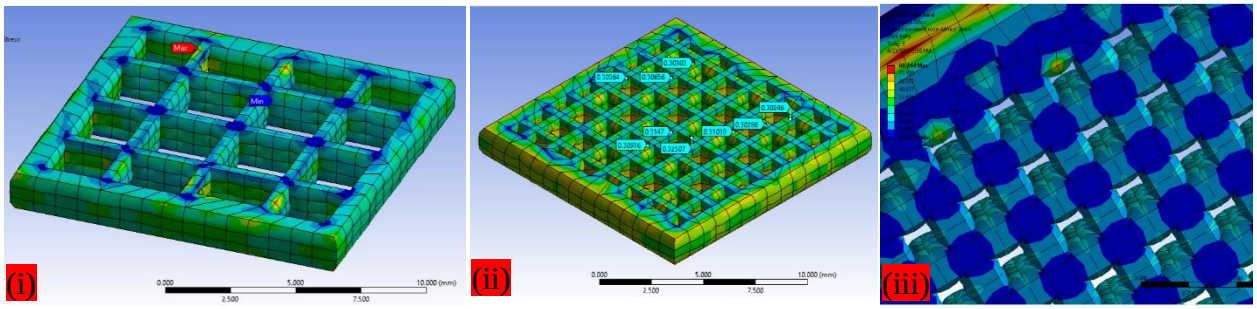

(c)

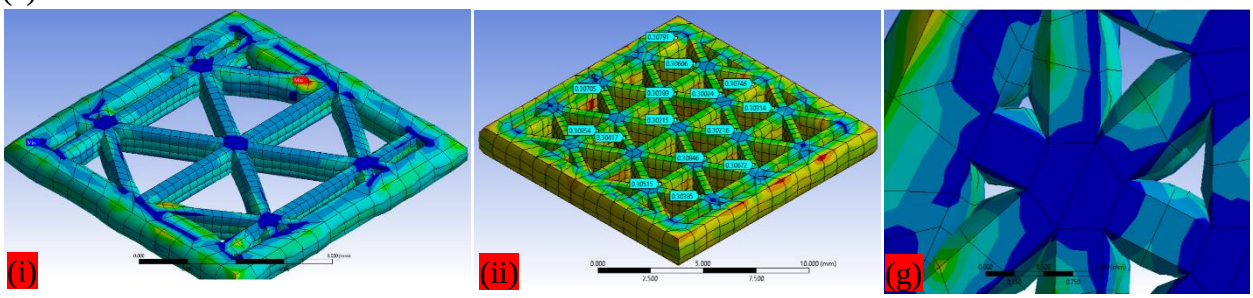

(d)

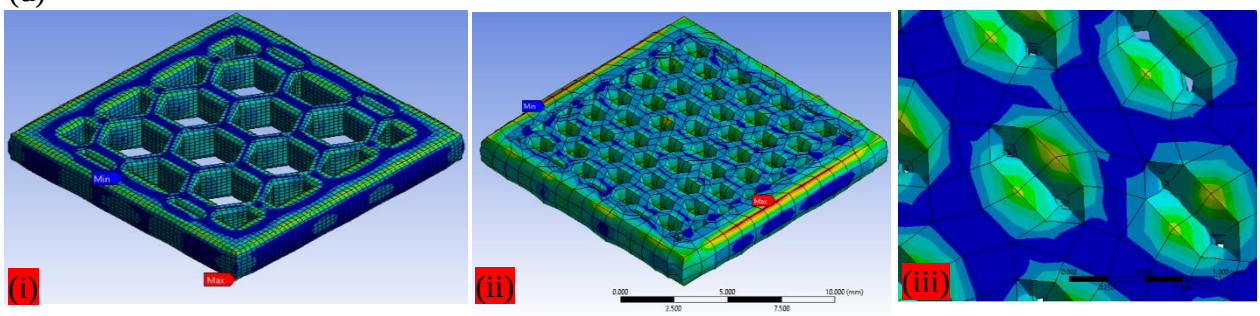

Figure 46: FEA compression simulation results (equivalent stress) for sensors with (a) 100% infill as well as (b) grid, (c) triangle and (d) honeycomb infill pattern at (i) 20%, (ii) 40% and (iii) 60% infill density with 410µm layer height and thickness at 30% strain

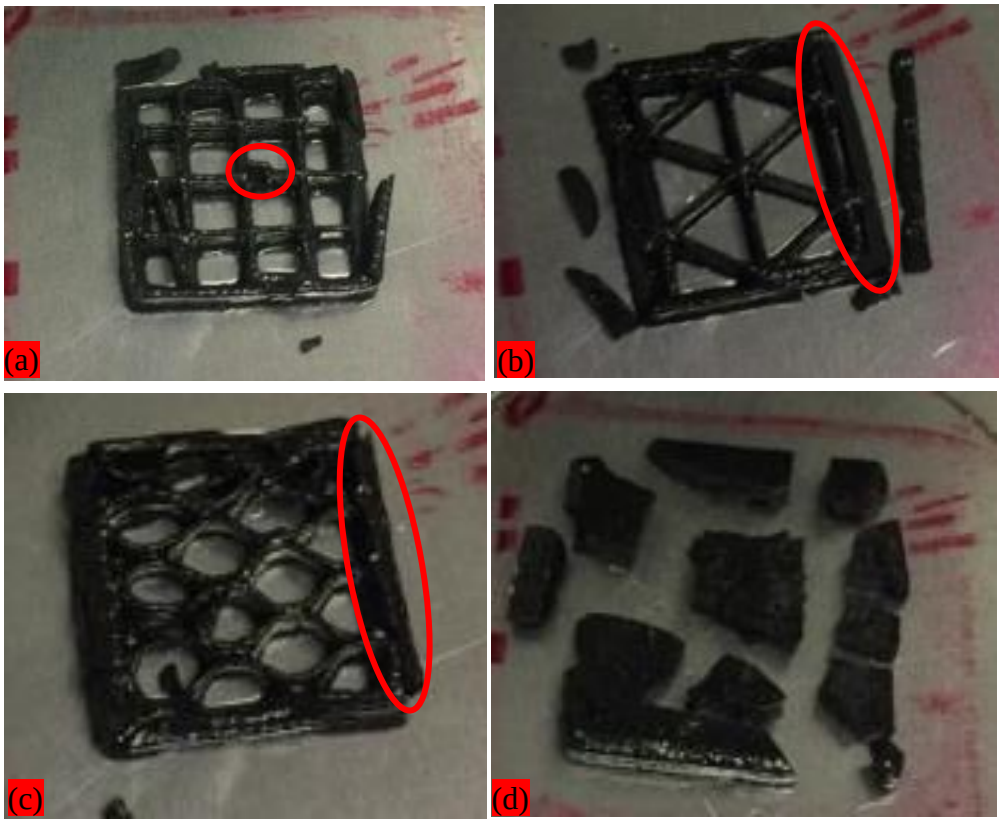

Figure 47: Fracture locations of 3D printed 20% infill (a) grid, (b) triangle and (c) honeycomb porous sensors along with the (d) 100% infill sensor

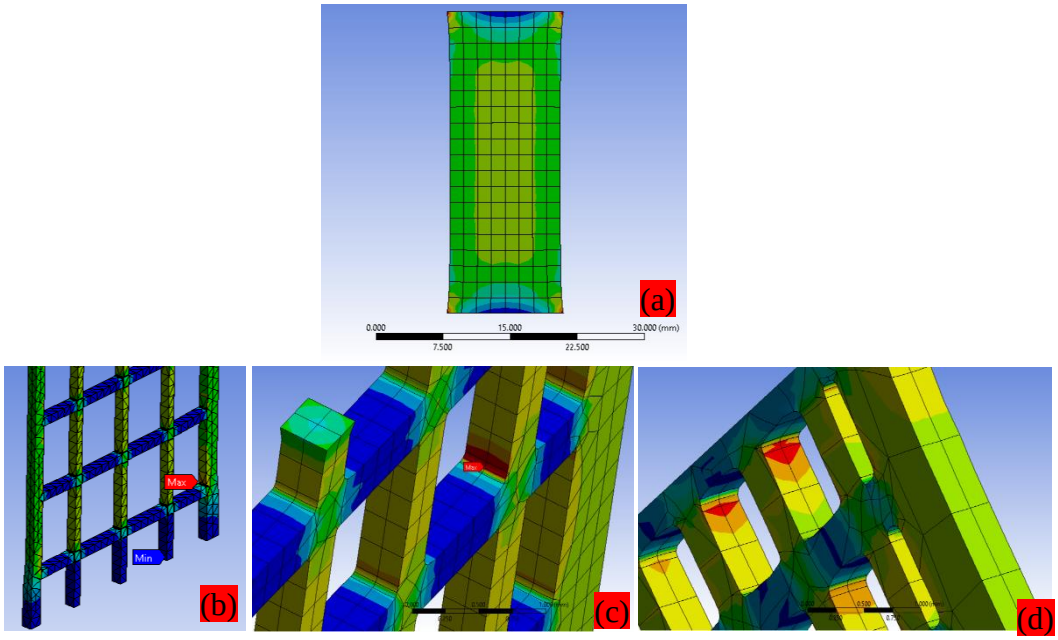

Figure 48: FEA tension simulation results (equivalent stress) of (a) a bulk material sample as well as (b) 20%, (c) 40% and (d) 60% infill grid samples at 30% strain

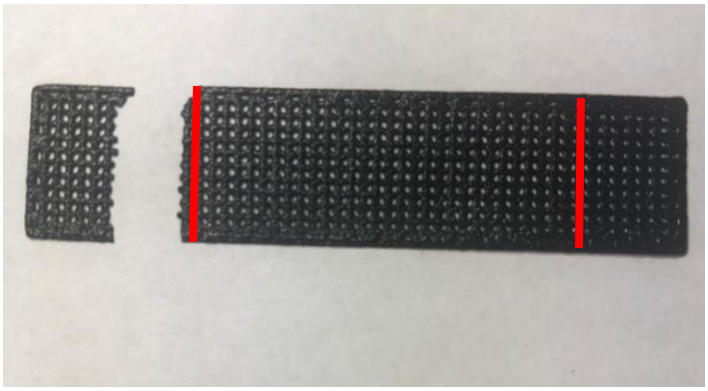

Figure 49: Fracture location of 3D printed tension sample with location of tensile grips (red)

4.4 Conclusion

This chapter focused on the characterization of the mechanical properties of the 3D printed porous PDMS/CNT nanocomposites. The samples were tested using ramped compression and tension load at a constant crosshead rate of 1 mm/min until the sensor being tested failed. The porous compression sensors achieved higher fracture stresses and strains at a majority of infill patterns and densities compared to the bulk material sensor, thus proving that they have higher durability than the commonly used bulk material sensor. Some porous sensors, namely the 410 µm layer 20% infill grid, the 260 µm layer 20% infill grid and the 260 µm layer 20% infill triangle sensors showed significantly reduced fracture stress and strain values as a result of minimal supporting material and thin infill walls. These resulted from the infill walls undergoing buckling and bending instead of the Poisson effect, and the infill failing as a consequence. In tension, the porous samples achieved fracture stresses and strains that were lower than those of the bulk material sample, making them unsuitable for use as highly stretchable strain sensors. Finally, the mechanical behavior of the 3D printed porous samples was investigated using FEA. Hyperelastic material curve fitting was utilized to define the material properties of the 3D printed CNT/PDMS nanocomposite material. The Mooney-Rivlin 3-parameter and the Neo-Hookean curve fitting models were used to define materials for the compression and tension tests respectively. The

simulated geometries produced results that fit excellently to the experimental data, thus showing the accuracy of the hyperelastic models. The behavior of the samples was observed, providing explanations of their fracture mechanical behavior.

Chapter 5. Conclusion and Future Work

This thesis performed an investigation on the use of 3D printing to fabricate controlled porous structures using a flexible CNT/PDMS nanocomposite with silica nanofiller. Four CNT/PDMS nanocomposite inks with 1.5 wt% CNT content were manufactured using a shear mixing and desiccation. A combination of two vinyl-terminated PDMS prepolymers with different viscosities were mixed with a dimethylsiloxane copolymer, with a platinum based catalyst used as a crosslinker. Thixotropic silica nanofiller was added to the nanocomposite ink in order to improve its rheological properties. While adding the CNTs was enough to achieve a yield point whereby the material holds shape and does not collapse upon extrusion, the yield point was relatively low and the material could not achieve the formation of complex infill patterns which usually require freestanding single line thick walls. CNT/PDMS formulations with 5 wt%, 10 wt%, 15 wt% and 20 wt% silica filler were tested using a TA Instruments Discovery HR2 rheometer in order to determine their rheological properties. The yield stress point increased with an increase in the silica filler weight percentage. While 5 wt% silica formulation showed significant spreading after printing, the other silica concentrations held very good shape upon extrusion. The 15 wt% silica formulation was chosen as the material of choice due to its geometric accuracy upon printing and its high yield point while maintaining high flexibility. 3D printing was performed using a Direct Ink Write method, with the extrusion system being driven by a pneumatic pump. 13 mm x 13 mm x 2.05 mm cuboid compression samples were 3D printed with grid, triangle and honeycomb infill patterns, with 20%, 40%, 60% and 100% infill densities, and with 410 and 260 µm layer heights and thicknesses. 13 mm x 50 mm x 0.41 mm tension samples with a porous grid structure were also 3D printed. The 3D printed samples achieved excellent geometric accuracy as a result of the good rheological properties of the nanocomposite ink. The multi-layer compression sensors

showed no collapse of one layer into another, and there were little to no voids observed within the samples. The morphology, microstructure and CNT distribution within the 3D printed porous samples was characterized using a Field Emission SEM. The CNTs and the silica fillers were well distributed within the polymer matrix, with few agglomerations formed. FE-SEM images at higher magnification (2500 X and 10 000 X) show the CNTs in contact with each other, forming conductive networks. There were also gaps observed between adjacent CNTs that could be reduced by the compression of the material, thus displaying the piezoresistive effect. The porosity of the 3D printed samples was characterized using a tabletop SEM. The pores showed good geometric accuracy to the sliced models with little dragging of existing lines occurring. The pore size and infill density were analyzed using the image processing software ImageJ. The analysis showed that each infill density as annotated by the slicing software differs from the gcode model produced and from the 3D printed product by about 20%. This discrepancy was as a result of the slicing software used. For simplicity and consistency, the 20%, 40% and 60% infill labels were used to identify the three different porosities. The porosity values determined from the experimental 3D printed samples and the slicing software models were very similar, further showing the good geometric accuracy achieved. The porosities at each infill density were similar at different infill patterns, for example the 20% infill grid sensor achieved similar porosities to the 20% infill triangle and honeycomb sensors. The line thicknesses of the lines surrounding a pore as well as the area of the joint where lines intersect within the infill were also characterized. The line thicknesses were consistent with the sliced models. For both the 410 and 260 μm layer thicknesses, the grid pattern showed the smallest joint area by a significant margin due to it consisting of two intersected lines at each joint while the triangle pattern had three intersected lines and the honeycomb pattern had

two lines that were connected in parallel. The grid infill tension samples showed similar porosity, line thickness and joint area to the compression grid infill sensors.

The characterization of the piezoresistive response of the 3D printed porous CNT/PDMS nanocomposite sensors was achieved using cyclic compression tests at 1%, 5%, 10% and 20% strain with a constant crosshead speed of 1 mm/min. The results of the test showed that the samples all showcased the piezoresistive effect whereby the resistance of the sensors decreased with an increase of the compressive load. The sensing functions of the bulk material sensor showed high incidence of hysteresis, with the graphs $\Delta R/R$ curves displaying two troughs on each sensing function cycle and a drift of the entire sensing function curve. The porous sensors all had sensing functions which showed decreased amounts of the hysteresis effect. The piezoresistive sensitivity of the sensors was characterized using the gauge factor. Results showed that in most cases the reduction of hysteresis led to an increase in the piezoresistive sensitivity, highlighted by the fact that the porous sensors which had the least hysteresis seen on their sensing functions achieved the highest gauge factors. The highest gauge factor achieved was 26.1 measured for the 410 μm layer 20% infill grid sensor. The pressure sensitivity of the porous sensors was determined using the stress gauge factor, and the values obtained were compared to the bulk material sensors. The porous sensors achieved higher pressure sensitivity than the bulk sensors due to their significantly reduced stiffnesses, the 410 μm layer 20% infill grid sensor achieving a particularly high pressure gauge factor of 190.5 MPa^{-1}. The amount of hysteresis within the sensors was quantified by using stress-strain behavior on the loading and unloading cycles during compression mechanical testing. The area between the loading and unloading curves was calculated to determine the numerical differences in the hysteresis amounts. The 3D printed porous sensors all achieved significantly lower hysteresis values compared to the bulk material sensors.

Finally, the mechanical properties of the 3D printed porous structures were characterized using fracture experimental testing at a constant crosshead speed of 1 mm/min, as well as using Finite Element Analysis. The results of the fracture mechanical tests reveal that the porous compression tests achieved higher fracture stresses and strains than the bulk sensors at a majority of infill patterns and densities. It could therefore be said that the porous sensors have increased durability compared to the bulk sensors. The 20% infill grid sensors with 410 and 260 μm layer thickness showed significantly reduced fracture stress and strain values due to reduced supporting material and thin infill walls. Computer simulations were performed in order to determine the structures' behavior when loaded in compression and in tension. The material properties were defined by performing hyperelastic material curve fitting using stress-strain data obtained from experimentation. The Mooney-Rivlin 3-parameter and the Neo-Hookean curve fitting models were used to define the material properties for the compression and tension samples respectively. The results of the Finite Element Analysis show that the stresses are concentrated along the edges of the compression samples at most infill patterns and densities, and that the porous internal structure added to the sensors' durability. The tension samples, however, were found to be weaker than the bulk sample because the tension load was mainly supported by the longitudinal infill lines and the bulk sample had the most lines supporting the load.

This study is beneficial since it explores the improvement of the sensing capacity of flexible CNT/PDMS nanocomposite sensors by introducing controlled porosity in the form of varying infill patterns and densities. The use of 3D printing to achieve porosity is greatly advantageous since it allows for the tunability of porosity and pore size. Since the study details the effect of infill pattern, infill density and the layer thickness on the piezoresistive sensing response, the sensitivity can therefore be tuned by varying these parameters. Although this study highlights

these benefits in detail, there is still more room for improvement and innovation. Firstly, parameters such as the infill pattern, density and layer thickness could be varied more than shown in this study. Secondly, since the slicing software used had an infill density annotation offset of about 20%, an iterative method could be used to locate the infill percentage annotated by the slicing software which results in the desired model and experimental value, with the approximate 20% difference being used as a starting point. Additionally, an investigation into the threshold value at high porosity beyond which the hysteresis increases sharply and piezoresistive sensitivity decreases significantly could help further understanding of the electrical properties of these sensors. This porosity threshold value affects the mechanical properties of the sensors as well since beyond it the fracture stress and strain decrease significantly within grid infill samples in particular, therefore such a study would greatly increase understanding of the electrical and mechanical properties of the controlled porous structure. Moreover, further Finite Element Analysis could be performed on the nanocomposite samples. A more thorough failure analysis using failure criterion of elastomeric nanocomposites could shed more light on the fracture mechanical behavior of the 3D printed porous samples. Optimizations of the pore shape and infill density using FEA tools could also be performed in order to determine which infill types achieves the highest pressure sensitivity without surpassing the threshold. Lastly, the controlled porous structure could be implemented in geometries that have been optimized in literature such as the truncated cone. Conductive nanofiller such as graphene could be used in order to realize the full potential of such porous structures.

References

[1] Termehyousefi, A. (2017). Development of haptic based piezoresistive artificial fingertip: Toward efficient tactile sensing systems for humanoids. *Materials Science & Engineering.*, 1098-1103.

[2] Laflamme, S., Saleem, H., Vasan, B., Geiger, R., Chen, D., Kessler, M. and Rajan, K., 2013. Soft Elastomeric Capacitor Network for Strain Sensing Over Large Surfaces. *IEEE/ASME Transactions on Mechatronics*, 18(6), pp.1647-1654.

[3] Amjadi, M., Pichitpajongkit, A., Lee, S., Ryu, S. and Park, I., 2014. Highly Stretchable and Sensitive Strain Sensor Based on Silver Nanowire–Elastomer Nanocomposite. *ACS Nano*, 8(5), pp.5154-5163.

[4] Niu, D., Jiang, W., Ye, G., Wang, K., Yin, L., Shi, Y., Chen, B., Luo, F. and Liu, H., 2018. Graphene-elastomer nanocomposites based flexible piezoresistive sensors for strain and pressure detection. *Materials Research Bulletin*, 102, pp.92-99.

[5] Murray, W. and Miller, W., 1992. The Bonded Electrical Resistance Strain Gage. *New York: Oxford University Press*.

[6] Chen, L., Chen, G. and Lu, L., 2007. Piezoresistive Behavior Study on Finger-Sensing Silicone Rubber/Graphite Nanosheet Nanocomposites. *Advanced Functional Materials*, 17(6), pp.898-904.

[7] Stassi, S., Cauda, V., Canavese, G. and Pirri, C., 2014. Flexible Tactile Sensing Based on Piezoresistive Composites: A Review. *Sensors*, 14(3), pp.5296-5332.

[8] Mostofizadeh, A., Li, Y., Song, B. and Huang, Y., 2011. Synthesis, Properties, and Applications of Low-Dimensional Carbon-Related Nanomaterials. *Journal of Nanomaterials*, 2011, pp.1-21.

[9] Mata, A., Fleischman, A. and Roy, S., 2005. Characterization of Polydimethylsiloxane (PDMS) Properties for Biomedical Micro/Nanosystems. *Biomedical Microdevices*, 7(4), pp.281-293.

[10] Prabowo, F., Wing-Keung, A. and Shen, H., 2015. Effect of Curing Temperature and Cross-Linker to Pre-Polymer Ratio on the Viscoelastic Properties of a PDMS Elastomer. *Advanced Materials Research*, 1112, pp.410-413.

[11] Fiorillo, A., Critello, C. and Pullano, S., 2018. Theory, technology and applications of piezoresistive sensors: A review. *Sensors and Actuators A: Physical*, 281, pp.156-175.

[12] Liu, Chang (2006). Piezoresistive Sensors. *Foundations of MEMS*. Upper Saddle River, NG: Prentice Hall. ISBN 0131472860.

[13] Hu, N., Karube, Y., Yan, C., Masuda, Z. and Fukunaga, H., 2008. Tunneling effect in a polymer/carbon nanotube nanocomposite strain sensor. *Acta Materialia*, 56(13), pp.2929-2936.

[14] Tallman, T., Gungor, S., Wang, K. and Bakis, C., 2015. Tactile imaging and distributed strain sensing in highly flexible carbon nanofiber/polyurethane nanocomposites. *Carbon*, 95, pp.485-493.

[15] Chowdhury, S., Saha, M., Patterson, S., Robison, T. and Liu, Y., 2018. Highly Conductive Polydimethylsiloxane/Carbon Nanofiber Composites for Flexible Sensor Applications. *Advanced Materials Technologies*, 4(1), p.1800398.

[16] Luo, W., Charara, M., Saha, M. and Liu, Y., 2019. Fabrication and characterization of porous CNF/PDMS nanocomposites for sensing applications. *Applied Nanoscience*, 9(6), pp.1309-1317.

[17] Zhang, F., Wu, S., Peng, S., Sha, Z. and Wang, C., 2019. Synergism of binary carbon nanofibres and graphene nanoplates in improving sensitivity and stability of stretchable strain sensors. *Composites Science and Technology*, 172, pp.7-16.

[18] Toprakci, H., Kalanadhabhatla, S., Spontak, R. and Ghosh, T., 2013. Polymer Nanocomposites Containing Carbon Nanofibers as Soft Printable Sensors Exhibiting Strain-Reversible Piezoresistivity. *Advanced Functional Materials*, 23(44), pp.5536-5542.

[19] Mapkar, J., Belashi, A., Berhan, L. and Coleman, M., 2013. Formation of high loading flexible carbon nanofiber network composites. *Composites Science and Technology*, 75, pp.1-6.

[20] Cai, J., Chawla, S. and Naraghi, M., 2014. Piezoresistive effect of individual electrospun carbon nanofibers for strain sensing. *Carbon*, 77, pp.738-746.

[21] Tamburrano, A., Sarasini, F., De Bellis, G., D'Aloia, A. and Sarto, M., 2013. The piezoresistive effect in graphene-based polymeric composites. *Nanotechnology*, 24(46), p.465702.

[22] Ke, K., Solouki Bonab, V., Yuan, D. and Manas-Zloczower, I., 2018. Piezoresistive thermoplastic polyurethane nanocomposites with carbon nanostructures. *Carbon*, 139, pp.52-58.

[23] Shang, S., Yue, Y. and Wang, X., 2016. Piezoresistive strain sensing of carbon black /silicone composites above percolation threshold. *Review of Scientific Instruments*, 87(12), p.123910.

[24] Lee, B. and Loh, K., 2015. A 2D percolation-based model for characterizing the piezoresistivity of carbon nanotube-based films. *Journal of Materials Science*, 50(7), pp.2973-2983.

[25] Al-solamy, F., Al-Ghamdi, A. and Mahmoud, W., 2011. Piezoresistive behavior of graphite nanoplatelets based rubber nanocomposites. *Polymers for Advanced Technologies*, 23(3), pp.478-482.

[26] Chen, L., Lu, L., Wu, D. and Chen, G., 2007. Silicone rubber/graphite nanosheet electrically conducting nanocomposite with a low percolation threshold. *Polymer Composites*, 28(4), pp.493-498.

[27] He, Q., Yuan, T., Zhang, X., Guo, S., Liu, J., Liu, J., Liu, X., Sun, L., Wei, S. and Guo, Z., 2014. Heavy duty piezoresistivity induced strain sensing natural rubber/carbon black nanocomposites reinforced with different carbon nanofillers. *Materials Research Express*, 1(3), p.035029.

[28] Li, L., Zhang, M. and Ruan, W., 2014. Studies on synergistic effect of CNT and CB nanoparticles on PVDF. *Polymer Composites*, 36(12), pp.2248-2254.

[29] Wang, L., Ding, T. and Wang, P., 2009. Thin Flexible Pressure Sensor Array Based on Carbon Black/Silicone Rubber Nanocomposite. *IEEE Sensors Journal*, 9(9), pp.1130-1135.

[30] M. Shimojo, A. Namiki, M. Ishikawa, R. Makino, and K. Mabuchi, “Atactile sensor sheet using pressure conductive rubber with electrical-wires stitched method,”IEEE Sensors J., vol. 4, no. 5, pp. 589–596

[31] Cao, M., Wang, X., Cao, W. and Yuan, J., 2015. Ultrathin graphene: electrical properties and highly efficient electromagnetic interference shielding. *Journal of Materials Chemistry C*, 3(26), pp.6589-6599.

[32] Lee, C., Wei, X., Kysar, J. and Hone, J., 2008. Measurement of the Elastic Properties and Intrinsic Strength of Monolayer Graphene. *Science*, 321(5887), pp.385-388.

[33] Hou, Y., Wang, D., Zhang, X., Zhao, H., Zha, J. and Dang, Z., 2013. Positive piezoresistive behavior of electrically conductive alkyl-functionalized graphene/polydimethylsilicone nanocomposites. *J. Mater. Chem. C*, 1(3), pp.515-521.

[34] Tung, T., Robert, C., Castro, M., Feller, J., Kim, T. and Suh, K., 2016. Enhancing the sensitivity of graphene/polyurethane nanocomposite flexible piezo-resistive pressure sensors with magnetite nano-spacers. *Carbon*, 108, pp.450-460.

[35] Mutlay, İ. and Tudoran, L., 2014. Percolation Behavior of Electrically Conductive Graphene Nanoplatelets/Polymer Nanocomposites: Theory and Experiment. *Fullerenes, Nanotubes and Carbon Nanostructures*, 22(5), pp.413-433.

[36] Gudarzi, M. and Sharif, F., 2012. Molecular level dispersion of graphene in polymer matrices using colloidal polymer and graphene. *Journal of Colloid and Interface Science*, 366(1), pp.44-50.

[37] Cai, D. and Song, M., 2010. Recent advance in functionalized graphene/polymer nanocomposites. *Journal of Materials Chemistry*, 20(37), p.7906.

[38] Donaldson, K., Aitken, R., Tran, L., Stone, V., Duffin, R., Forrest, G. and Alexander, A., 2006. Carbon Nanotubes: A Review of Their Properties in Relation to Pulmonary Toxicology and Workplace Safety. *Toxicological Sciences*, 92(1), pp.5-22.

[39] Jouni, M., Boiteux, G. and Massardier, V., 2013. New melt mixing polyethylene multiwalled carbon nanotube nanocomposites with very low electrical percolation threshold. *Polymers for Advanced Technologies*, 24(10), pp.909-915.

[40] Kang, J., Park, C., Scholl, J., Brazin, A., Holloway, N., High, J., Lowther, S. and Harrison, J., 2009. Piezoresistive characteristics of single wall carbon nanotube/polyimide nanocomposites. *Journal of Polymer Science Part B: Polymer Physics*, 47(16), pp.1635-1636.

[41] Cattin, C. and Hubert, P., 2014. Piezoresistance in Polymer Nanocomposites with High Aspect Ratio Particles. *ACS Applied Materials & Interfaces*, 6(3), pp.1804-1811.

[42] Wang, Q., Quek, S. and Varadan, V., 2007. Torsional buckling of carbon nanotubes. *Physics Letters A*, 367(1-2), pp.135-139.

[43] J. -. Wang, M. -. Lin, H. -. Liang, R. Chen and W. Fang, "Piezoresistive nanocomposite rubber elastomer for stretchable MEMS sensor," *2016 IEEE 29th International Conference on Micro Electro Mechanical Systems (MEMS)*, Shanghai, 2016, pp. 550-553

[44] Kim, K., Park, J., Suh, J., Kim, M., Jeong, Y. and Park, I., 2017. 3D printing of multiaxial force sensors using carbon nanotube (CNT)/thermoplastic polyurethane (TPU) filaments. *Sensors and Actuators A: Physical*, 263, pp.493-500.

[45] Ye, X., Liu, H., Ding, Y., Li, H. and Lu, B., 2009. Research on the cast molding process for high quality PDMS molds. *Microelectronic Engineering*, 86(3), pp.310-313.

[46] Wu, C., Lin, H., Hsu, J., Yip, M. and Fang, W., 2009. Static and dynamic mechanical properties of polydimethylsiloxane/carbon nanotube nanocomposites. *Thin Solid Films*, 517(17), pp.4895-4901.

[47] Ren, X., Chaurasia, A. and Seidel, G., 2016. Concurrent multiscale modeling of coupling between continuum damage and piezoresistivity in CNT-polymer nanocomposites. *International Journal of Solids and Structures*, 96, pp.340-354.

[48] Gibson, I., Rosen, D. and Stucker, B., 2015. *Additive Manufacturing Technologies: 3D Printing, Rapid Prototyping, And Direct Digital Manufacturing*. 2nd ed. New York: Springer.

[49] Charara, M., Abshirini, M., Saha, M., Altan, M. and Liu, Y., 2019. Highly sensitive compression sensors using three-dimensional printed polydimethylsiloxane/carbon nanotube nanocomposites. *Journal of Intelligent Material Systems and Structures*, 30(8), pp.1216-1224.

[50] Lu J, Lu M, Bermak A, et al. (2007) Study of piezoresistance effect of carbon nanotube-PDMS composite materials for nanosensors. In: 2007 7th IEEE Conference on Nanotechnology (IEEE NANO), Hong Kong, 2–5 August, pp.1240–1243. New York: IEEE.

[51] Jung, Y., Jung, K., Park, B., Choi, J., Kim, D., Park, J., Ko, J. and Cho, H., 2019. Wearable piezoresistive strain sensor based on graphene-coated three-dimensional micro-porous PDMS sponge. *Micro and Nano Systems Letters*, 7(1).

[52] Wu, S., Zhang, J., Ladani, R., Ravindran, A., Mouritz, A., Kinloch, A. and Wang, C., 2017. Novel Electrically Conductive Porous PDMS/Carbon Nanofiber Composites for Deformable Strain Sensors and Conductors. *ACS Applied Materials & Interfaces*, 9(16), pp.14207-14215.

[53] Mattmann, C., Clemens, F. and Tröster, G., 2008. Sensor for Measuring Strain in Textile. *Sensors*, 8(6), pp.3719-3732.

[54] Cai, L., Li, J., Luan, P., Dong, H., Zhao, D., Zhang, Q., Zhang, X., Tu, M., Zeng, Q., Zhou, W. and Xie, S., 2012. Highly Transparent and Conductive Stretchable Conductors Based on Hierarchical Reticulate Single-Walled Carbon Nanotube Architecture. *Advanced Functional Materials*, 22(24), pp.5238-5244.

[55] Huang, C., Bian, Z., Fang, C., Zhou, X. and Song, J., 2018. Experimental and Theoretical Study on Mechanical Properties of Porous PDMS. *Journal of Applied Mechanics*, 85(4).

[56] Yang, J., Zhang, Z., Men, X. and Xu, X., 2009. Fabrication of stable, transparent and superhydrophobic nanocomposite films with polystyrene functionalized carbon nanotubes. *Applied Surface Science*, 255(22), pp.9244-9247.

[57] Alison, L., Menasce, S., Bouville, F., Tervoort, E., Mattich, I., Ofner, A. and Studart, A., 2019. 3D printing of sacrificial templates into hierarchical porous materials. *Scientific Reports*, 9(1).

[58] Mu, X., Bertron, T., Dunn, C., Qiao, H., Wu, J., Zhao, Z., Saldana, C. and Qi, H., 2017. Porous polymeric materials by 3D printing of photocurable resin. *Materials Horizons*, 4(3), pp.442-449.

[59] Zhao, T., Li, T., Chen, L., Yuan, L., Li, X. and Zhang, J., 2019. Highly Sensitive Flexible Piezoresistive Pressure Sensor Developed Using Biomimetically Textured Porous Materials. *ACS Applied Materials & Interfaces*, 11(32), pp.29466-29473.

[60] Abshirini, M., Charara, M., Marashizadeh, P., Saha, M., Altan, M. and Liu, Y., 2019. Functional nanocomposites for 3D printing of stretchable and wearable sensors. *Applied Nanoscience*, 9(8), pp.2071-2083.

[61] Kumar, N. and Rao, V., 2016. Hyperelastic Mooney-Rivlin Model: Determination and Physical Interpretation of Material Constants. *MIT International Journal of Mechanical Engineering*, Vol. 6(No. 1), pp.pp. 43-46.

[62] Gent, A., 2012. *Engineering With Rubber*. Cincinnati: Hanser Publications, pp.303-304.

[63] Alamusi, Hu, N., Fukunaga, H., Atobe, S., Liu, Y. and Li, J., 2011. Piezoresistive Strain Sensors Made from Carbon Nanotubes Based Polymer Nanocomposites. *Sensors*, 11(11), pp.10691-10723.

[64] Mondal, A., Sukati, M., Charara, M., Saha, M., Liu, Y., Patterson, S. and Robison, T., 2019. "Investigation of Rheology and 3D Printability of PDMS Nanocomposites Ink". *American Society for Composites 2019, 34th Technical Conference.*